

FABRICATION OF MONODOMAIN POROUS ALUMINA  
USING NANOIMPRINT LITHOGRAPHY  
AND ITS APPLICATIONS

**Dissertation**

zur Erlangung des akademischen Grades

Doktoringenieur (Dr.-Ing.)

genehmigt durch die

Mathematisch-Naturwissenschaftlich-Technischen Fakultät  
(Ingenieurwissenschaftlicher Bereich)  
der Martin-Luther-Universität Halle-Wittenberg

von Herrn Dipl.-Ing. Jinsub Choi  
geb.: 30.06.1974 in Seoul, Korea

Gutachter:

1. Prof. Dr. Ulrich Gösele
2. Prof. Dr. Helmut Föll
3. Prof. Dr. Patrik Schmuki

Halle (Saale), Sep. 2003

verteidigt am 05.02.2004

# Contents

<b>1</b>	<b>Aluminum anodization</b>	<b>1</b>
1.1	History . . . . .	1
1.2	Electrochemistry of anodic alumina . . . . .	2
1.2.1	Thermodynamics . . . . .	2
1.2.2	Kinetics . . . . .	3
1.3	Composition of the oxide . . . . .	3
1.4	Barrier-type and porous-type alumina . . . . .	4
1.4.1	Inner and outer oxide layer . . . . .	4
1.4.2	Oxide thickness as a function of applied potential . . . . .	5
1.4.3	Pore formation mechanisms . . . . .	6
1.5	Self-ordered porous alumina - current state-of-the-art . . . . .	7
1.5.1	Experimental set-up . . . . .	7
1.5.2	Self-ordered alumina by 2-step anodization . . . . .	9
1.5.3	The mechanical stress model . . . . .	10
1.5.4	Anodization parameters influencing self-ordering . . . . .	11
<b>2</b>	<b>Self-ordered porous alumina - new insight in growth</b>	<b>13</b>
2.1	The 10% porosity rule . . . . .	13
2.2	Relationship between the mechanical stress model and the 10% porosity rule . . . . .	14
2.3	Deviations from the 10 % porosity rule . . . . .	15
2.4	Summary . . . . .	16
<b>3</b>	<b>Monodomain porous alumina obtained by nanoimprint lithography</b>	<b>17</b>
3.1	Nanoimprint lithography (NIL) . . . . .	17
3.2	Previous methods for pre-patterning Al substrates . . . . .	17
3.2.1	Dot-like master stamp . . . . .	17
3.2.2	Direct writing on Al by lithography . . . . .	19
3.2.3	2-step indentation using optical gratings with periodic lines . . . . .	19
3.2.4	Thin Al films on prestructured Si . . . . .	19
3.3	A novel imprint method . . . . .	19
3.3.1	Fabrication process of imprint stamp . . . . .	19
3.3.2	Nanoindentation . . . . .	22
3.3.3	Anodization of imprinted aluminum . . . . .	23
3.3.4	Monodispersity of pore size . . . . .	23
3.3.5	Influence of impurities . . . . .	24
3.4	Summary . . . . .	27
<b>4</b>	<b>Porous alumina structures obtained by advanced nanoimprint lithography</b>	<b>28</b>
4.1	Smart nanoimprint lithography . . . . .	28
4.1.1	Experimental . . . . .	28
4.1.2	Results and discussion . . . . .	29
4.2	Monodomain porous alumina with branched structures . . . . .	34

4.2.1	Experimental . . . . .	35
4.2.2	Results and discussion . . . . .	36
4.3	Monodomain porous alumina on Si . . . . .	40
4.3.1	Experimental . . . . .	41
4.3.2	Results and discussion . . . . .	42
4.4	Superposition of successive nanoimprint patterns . . . . .	43
4.4.1	Experimental . . . . .	43
4.4.2	Theoretical description . . . . .	43
4.4.3	Results and discussion . . . . .	45
4.5	Monodomain porous alumina with modulated pore diameter . . . . .	48
4.5.1	Experimental . . . . .	48
4.5.2	Results and discussion . . . . .	49
4.6	Summary . . . . .	51
<b>5</b>	<b>Ti anodization: A comparison with aluminum anodization</b>	<b>52</b>
5.1	Titanium metal among valve metals . . . . .	52
5.2	Experimental . . . . .	53
5.2.1	Preparation of polished substrates . . . . .	53
5.2.2	Nanoimprint . . . . .	53
5.2.3	Anodization and analysis . . . . .	53
5.3	Results and Discussion . . . . .	54
5.3.1	Pore formation above the breakdown potential of the anodic oxide . . .	54
5.3.2	Pore formation below the breakdown potential of the anodic oxide . . .	63
5.4	Summary . . . . .	64
<b>6</b>	<b>Application I - Templates for silver nanowire growth</b>	<b>65</b>
6.1	Electrochemical silver deposition into monodomain porous alumina . . . . .	65
6.2	Silver deposition into templates with branches . . . . .	68
6.3	Silver deposition into porous Al films on Si . . . . .	68
6.4	Summary . . . . .	70
<b>7</b>	<b>Application II - Porous alumina photonic crystals</b>	<b>71</b>
7.1	Definition of photonic bandgaps . . . . .	71
7.2	Porous alumina photonic crystals . . . . .	71
7.2.1	Optical characterization of porous alumina . . . . .	72
7.2.2	Optical setup . . . . .	72
7.2.3	Calculations of reflectivity and bandstructure . . . . .	73
7.2.4	Duplex structure of porous alumina: inner and outer oxide . . . . .	73
7.2.5	Optical characterization . . . . .	75
7.2.6	Discussion . . . . .	80
7.3	Summary . . . . .	81
<b>8</b>	<b>Conclusions</b>	<b>83</b>
<b>9</b>	<b>Outlook</b>	<b>86</b>

## Notation

$\Delta G^o$  = Gibbs' free energy

$a$  = Lattice constants of the first nanoimprinted pattern, lattice constant of photonic crystal

$Al_{aq^{3+}}$  = Total amount of  $Al^{3+}$  anions in the electrolyte after anodization

$Al_{tot}$  = Total amount of oxidized Al atoms

$b$  = Lattice constant of the second nanoimprinted pattern

$D_B$  (nm) = Thickness of the barrier-layer

$D_{cell}$  (nm) = Cell size of hexagonally close-packed porous alumina array

$D_{E-field}$  (nm) = Circular electric field on the alumina oxide caused by the applied potential

$D_{inner}$  (nm) = Inner wall thickness

$D_{int}$  (nm) = Interpore distance (= pore spacing)

$D_m$  (nm) = Diameter of the center of polymer replica hillocks

$D_{moi}$  (nm) = Periodicity of Moiré pattern

$D_{outer}$  (nm) = Outer wall thickness

$D_p$  (nm) = Pore diameter

$E$  (V/m) = Electric field strength

$E_0$  (V) = Electrode potential

$E_{BO}$  (V) = Breakdown potential of the oxide film

$F$  (C/mol) = Faraday constant (= 96500 C/mol)

$F_w$  = Weight fraction of aluminum ions in alumina (= 0.53)

$j_0$  (A/cm<sup>2</sup>) = Temperature and metal dependent constant in Guntherschultze-Betz equation

$j_a$  (A/cm<sup>2</sup>) = Current density contribution by anions

$j_b$  (A/cm<sup>2</sup>) = Current density for the formation of the barrier layer

$j_c$  (A/cm<sup>2</sup>) = Current density contribution by cations

$j_e$  (A/cm<sup>2</sup>) = Current density contribution by electrons

$j_{hp}$  (A/cm<sup>2</sup>) = Hypothetic current density for the formation of the porous layer (the difference between  $j_p$  and  $j_b$ )

$j_i$  (A/cm<sup>2</sup>) = Ionic current density ( $j_i = j_a + j_c$ )

$j_p$  (A/cm<sup>2</sup>) = Current density for the formation of the porous alumina

$k$  (nm/V) = Proportionality constant in the relationship between  $D_{int}$  and  $U$

$M$  = Center of the nanoindented pits

$M_1$  = Center of the  $P_1$  pits

$M_2$  = Center of the  $P_2$  pits

$n$  = Number of metal atoms in a molecular formula (example:  $n = 2$  for  $Al_2O_3$ ), refractive index of the dielectric material

$P$  (%) = Porosity

$P_1$  = Pores formed by anodization of nanoimprinted Al (at 195 V)

$P_2$  = Pores formed by smart nanoimprint (at 120 V)  
 $P_3$  = Pores formed by 2-step smart nanoimprint (at 72 V)  
 $R$  ( $\text{J mol}^{-1} \text{K}^{-1}$ ) = Universal gas constant ( $8.3144 \text{ mol}^{-1} \text{K}^{-1}$ )  
 $r$  (nm) = Pore radius  
 $\beta$  = Temperature and metal dependent constant in Guntherschultze-Betz equation  
 $T$  (K) = Absolute temperature  
 $t_{\text{Al}^{3+}}$  = Transport number of  $\text{Al}^{3+}$  anions  
 $T_m$  ( $^{\circ}\text{C}$ ) = Melting temperature  
 $t_{\text{O}^{2-}}$  = Transport number of  $\text{O}^{2-}$  cations  
 $U$  (V) = Applied potential  
 $V_{\text{Al}}$  = Volume of Al before anodization  
 $V_{\text{AlOx}}$  = Volume of alumina after anodization  
 $W_{\text{Al}}$  = Weight of aluminum  
 $W_{\text{AlOx}}$  = Weight of alumina  
 $x$  = Moving mirror displacement  
 $z$  = Charge number of the electrode  
 $\delta$  = Angle of the inclination of the beam relative to the optical axis  
 $\epsilon$  = Dielectric constant ( $= n^2$ )  
 $\epsilon_{\text{eff,outer}}$  = Effective dielectric constant of the outer oxide layer  
 $\epsilon_{\text{inner}}$  = Dielectric constant of the inner oxide layer  
 $\epsilon_{\text{outer}}$  = Dielectric constant of the outer oxide layer  
 $\theta$  = Rotation angle between the two nanoindentation steps  
 $\lambda$  (nm) = Wavelength  
 $\lambda_{\text{gap}}$  (nm) = Wavelength of light in photonic band gaps  
 $\xi$  = Volume expansion coefficient  
 $\rho_{\text{TiO}_2}$  ( $\text{g/cm}^3$ ) = Density of  $\text{TiO}_2$  ( $= 2.7 \text{ g/cm}^3$ )  
 $\rho_{\text{Al}}$  ( $\text{g/cm}^3$ ) = Density of aluminum ( $= 2.7 \text{ g/cm}^3$ )  
 $\rho_{\text{AlOx}}$  ( $\text{g/cm}^3$ ) = Density of porous alumina ( $= 3.2 \text{ g/cm}^3$ )  
 $\omega_0$  (Hz) = Midgap frequency  
 $\omega_c$  (Hz) = Upper band edge frequencies of the gap  
 $\omega_v$  (Hz) = Lower band edge frequencies of the gap

## Abstract

The self-ordering regimes associated with specific anodization conditions obeying the 10 % porosity rule are described which allow to obtain self-ordered porous alumina structures by electrochemical anodization. Monodomain porous alumina templates with very high aspect ratios are synthesized by nanoimprint lithography using a novel master stamp with periodic pyramids of 500 nm lattice constant, which have been fabricated on a 4 *in.* wafer by silicon processing technology. The combination of self-assembly and nanoimprint lithography allows the preparation of porous alumina templates with various configurations of pore arrangement that are not accessible by other state-of-the-art methods. Smart nanoimprint lithography, nanobranches, Moiré patterns, porous films on a Si substrate and porous alumina channels with a modulated diameter are discussed in detail. The same concepts are applied to prepare nanostructured porous oxides on another valve metals. Anodic oxides grown on a Ti substrate above and below the breakdown potential, respectively, are discussed in detail and compared with the mechanisms governing the formation of porous alumina. Two promising applications of porous alumina are investigated: First, it is successfully used as template for the synthesis of silver nanowires by electrochemical deposition. Secondly, optical properties of the porous alumina structures are measured. These show in principle the feasibility of their application as photonic crystals.

## Kurzfassung

Poröses Aluminiumoxid, eines der meist genutzten anorganischen Templatmaterialien, weist unter bestimmten Herstellungsbedingung selbstgeordnete Poren-Domänen auf. Im Rahmen meiner Doktorarbeit habe ich mich mit dem Phänomen der Selbstordnung von Porenstrukturen und dessen geeigneter Kombination mit lithographischen Methoden beschäftigt. Ich konnte zeigen, dass das selbstgeordnete Porenwachstum nur unter spezifischen Reaktionsbedingungen abläuft, welche durch die 10 %-Porositäts-Regel beschrieben und vorhergesagt werden können. Darauf aufbauend wurde ein Nanoprägestempel mit einem Abstand der pyramidalen Prägespitzen, der gerade einem der selbstgeordneten Regime entspricht, entwickelt. Durch die Kombination von Selbstordnung und Nanopräge-Lithographie konnten so großflächige monodomänige Porenstrukturen mit Porentiefen von mehr als 100  $\mu\text{m}$  erzeugt werden. Diese Kombination ermöglichte aber noch viele weitere Entwicklungen: Smarte Nanopräge-Lithographie, Nanoverzweigungen, Moiré-Strukturen, Integration von porösem Aluminiumoxid mit Siliziumtechnologien und Tiefenmodulation des Porendurchmessers. Basierend auf dem sehr guten Verständnis der Elektrochemie von Aluminium wurden dann versucht dieses Konzept auch auf andere Ventilmetalle auszudehnen, hier Titan. Dabei konnte allerdings gezeigt werden, dass es ein analoges Porenwachstum wie beim Aluminium aufgrund der halbleitenden Eigenschaften von Titan nicht gibt. Zum Schluss wurden zwei Anwendungsbeispiele von monodomänigem porösem Aluminiumoxid vorgestellt: die Synthese von geordneten Silber-Nanostabensembles und die Nutzung von porösem Aluminiumoxid als photonischer Kristall im sichtbaren Spektralbereich.

# 1. Aluminum anodization

## 1.1 History

The history of electrochemical oxidation of aluminum dates back to the beginning of the last century. Anodic treatment of aluminum were intensively investigated to obtain protective and decorative films on its surface [1]. More recently, applications of porous alumina with a huge surface area and a relatively narrow pore size distribution have been exploited [2]. For example, several attempts to fabricate inorganic membranes have been reported [3, 4, 5]. Nowadays, porous alumina is one of the most prominent template materials for synthesis of nanowires or nanotubes with monodisperse controllable diameter and high aspect ratios [6, 7, 8, 9, 10, 11, 12, 13, 14]. Moreover, it can be employed as a 2-D photonic crystal.

Numerous patents had been published before the 1950's, concerning the anodization of aluminum for coloring [15]. Since the early years, anodic processes at DC or AC current based on either chromic, sulfuric or oxalic acid as electrolytes have been paid attention to [15]. Consequently, it was observed that additives such as metal salts like copper, nickel, silver, arsenic, antimony, bismuth, tellurium, selenium or tin lead to a change of the physical and mechanical properties as well as of the colors of the oxide. Bengough's and Stuart's patent in 1923 is recognized as the first patent for protecting Al and its alloys from corrosion by means of an anodic treatment [16]. In 1936, Caboni invented the famous coloring method consisting of two sequential processes: anodization in sulfuric acid, followed by the application of an alternating current in a metal salt solution [17].

The development of electron microscopy led to a deeper understanding of the porous alumina structures. In 1953, Keller and his coworkers described a porous alumina model as a hexagonally close-packed duplex structure consisting of porous and barrier layers [18]. Also, they demonstrated the relationship of an applied potential and the geometric features of the hexagonal porous structures such as the interpore distance. This model was the basis for initial studies that aimed at better a understanding of the physical and chemical properties of porous alumina.

A review paper dealing with anodic oxide films on aluminum was already published in 1968 [19]. Structural features concerning anion incorporation and water content in the oxide and theoretical models of formation mechanisms of both the barrier-type oxide and the porous-type oxide were described in detail in this paper.

Between 1970 and 1990, studies by the Manchester group (led by Thompson and Wood) resulted in a deep insight in the growth mechanisms of alumina oxide films. This was possible by the uses of new techniques such as Transmission Electron Microscopy (TEM), marker methods and microtome sectioning. [20, 21, 22, 23]. A corresponding publication by O'Sullivan and Wood is one of the most cited articles on anodization of aluminum to obtain porous alumina structures [24].

Efforts on theoretical modelling of porous oxide growth were carried out by several groups [25, 26, 27, 28, 29, 30, 31, 32, 33]. Fundamentally, an instability mechanism in terms of a field

focusing phenomenon was attributed to create pores in the barrier oxide. In these papers, it is claimed that the theoretic modelling of the pore formation mechanism in alumina is analogous to that for other porous materials which can be obtained via an anodic treatment, for example, microporous silicon.

Based on a two-step replicating process, a self-ordered porous alumina membrane with 100 nm interpore distance was synthesized by Masuda and Fukuda in 1995 [34]. This discovery was a breakthrough in the preparation of 2D-polydomain porous alumina structures with a very narrow size distribution and extremely high aspect ratios. Two years later, they combined the aluminum anodization method with nanoimprint technologies, which allowed for the first time the preparation of a monodomain porous alumina structure [35].

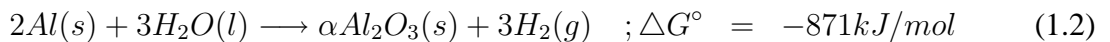
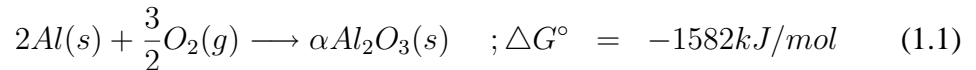
Numerous other groups, not mentioned here specifically, have also contributed to an improvement of porous alumina structures.

The purpose of this dissertation is to understand self-assembly of porous alumina under specific conditions (Chapter 1 and Chapter 2). In addition, nanoimprint methods are developed to obtain monodomain porous alumina structures (Chapter 3). These nanoimprint methods are further advanced to fabricate porous alumina arrays with various configurations (Chapter 4). Furthermore, the combination of nanoimprint and anodization will be applied to obtain porous oxides grown on titanium, which is also a valve metal<sup>1</sup> (Chapter 5). Finally, in the last two chapters, applications of the alumina templates will be discussed, for example, templates for monodisperse silver nanowires (Chapter 6) and 2D-photonic crystals (Chapter 7).

## 1.2 Electrochemistry of anodic alumina

### 1.2.1 Thermodynamics

The spontaneous reaction leading to the formation of aluminum oxide in air can be ascribed to the large negative Gibb's free energy changes [36].



If aluminum is electrochemically anodized, an oxide grows at the anode electrode [37],



and hydrogen evolves at the cathode



Assuming there are no complex anions, the Nernst equation reads

$$E = E_0 - \left(\frac{RT}{zF}\right) \ln\left(\frac{[red]}{[ox]}\right) \quad (1.5)$$

where  $R$  is the universal gas constant,  $T$  is the absolute temperature in Kelvin,  $z$  is the charge number of the electrode reaction, and  $F$  is the Faraday constant ( $96,500 \text{ C mol}^{-1}$ ). The electrode potential  $E$  at the anode can be written as

$$E = -1.550 - 0.0591pH \quad (1.6)$$

---

<sup>1</sup>The definition of valve metal will be discussed in the Chapter 4.

Name	Crystalline form	Density (g/cm <sup>3</sup> ) / Crystal system	Remark
Corundum	$\alpha$ -Al <sub>2</sub> O <sub>3</sub>	3.97 / hexagonal	found in nature
Boehmite	$\alpha$ -Al <sub>2</sub> O <sub>3</sub> ·H <sub>2</sub> O	3.44 / ortho-rhombic	
Gibbsite	$\alpha$ -Al <sub>2</sub> O <sub>3</sub> ·(H <sub>2</sub> O) <sub>3</sub>	2.42 / monoclinic	
Diaspore	$\beta$ -Al <sub>2</sub> O <sub>3</sub> ·(H <sub>2</sub> O)	3.4 / ortho-rhombic	no occurrence in nature
Bayerite	$\beta$ -Al <sub>2</sub> O <sub>3</sub> ·(H <sub>2</sub> O) <sub>3</sub>	2.53 / monoclinic	
Gamma alumina	$\gamma$ -Al <sub>2</sub> O <sub>3</sub>	/	anhydrous alumina with ill-defined structure

**Table 1.1:** Alumina oxide forms [39]

This explains that the reaction at the anode electrode (Al) thermodynamically depends on the pH value, which is determined by electrolyte and temperature.

## 1.2.2 Kinetics

The current density passing across the oxide film can be written as [19, 37]

$$j = j_a + j_c + j_e \quad (1.7)$$

where  $j_a$ ,  $j_c$  and  $j_e$  are the anion-contributing, cation-contributing and electron-contributing current density, respectively. Since the electronic conductivity in the aluminum oxide is very low, the ionic current density ( $j_i = j_a + j_c$ ) is the predominant mode to transport the charges. The relationship between the ionic current,  $j_i$ , and the electric field,  $E$ , can be expressed in terms of the Guntherschultze-Betz equation

$$j_i = j_0 \exp(\beta E) \quad (1.8)$$

where both  $j_0$  and  $\beta$  are temperature- and metal-dependent parameters. For the aluminum oxide, the electric field  $E$ ,  $j_0$  and  $\beta$  are in the range of  $10^6$  to  $10^7$  V/cm,  $1 \times 10^{-16}$  to  $3 \times 10^{-2}$  mA/cm<sup>2</sup> and  $1 \times 10^{-7}$  to  $5.1 \times 10^{-6}$  cm/V, respectively [38]. Based on the Guntherschultze-Betz equation, the rate-limiting steps of the film formation are determined by the ionic transport either at the metal/oxide interface, within the bulk oxide or at the oxide/electrolyte interface [19]. Nowadays, it is generally accepted that the oxides simultaneously grow at both interfaces, e.g., at the metal/oxide interface by Al<sup>3+</sup> transport and at the oxide/electrolyte interface by oxygen ion transport [21, 24]. For example, the transport number<sup>2</sup> of Al<sup>3+</sup> anions,  $t_{Al^{3+}}$ , and the cation transport number,  $t_{O^{2-}}$ , were reported as 0.45 and 0.55, respectively, for 5mA/cm<sup>2</sup> [22].

## 1.3 Composition of the oxide

Due to a number of polymorphs, hydrates, and incorporated ions, anodic Al<sub>2</sub>O<sub>3</sub> can exist in various forms, e.g., Al<sub>2</sub>O<sub>3</sub>·(H<sub>2</sub>O)<sub>n</sub> where n = 0 to 3 [37, 40]. Six forms are mostly discussed (see Table 1.1). Gibbsite and Boehmite are converted to several transition alumina minerals such as  $\gamma$  series (e.g.,  $\gamma$ ,  $\rho$ ,  $\xi$ ) and  $\delta$  series, (e.g.,  $\delta$ ,  $\kappa$ ,  $\theta$ ) by heating. Corundum, which thermodynamically

<sup>2</sup>The fraction of the total current carried in a solution by a given ion. Ions may carry drastically different portions of the total current if their mobilities are different. The transport numbers of the anion and the cation adds up to unity.

is the most stable form among alumina oxides, is generated above 1100°C, regardless of the transition course. Boehmite heated at between 400 ~ 500 °C yields  $\gamma$ -Al<sub>2</sub>O<sub>3</sub> consisting of irregular structures [40].

Generally speaking, anodic Al<sub>2</sub>O<sub>3</sub> was mostly reported as a form of X-ray amorphous solid [19, 24, 37]. For the barrier layer, the presence of nanocrystallites of  $\gamma'$ -Al<sub>2</sub>O<sub>3</sub> with sizes of 2-10 nm was demonstrated by several authors.  $\gamma'$ -Al<sub>2</sub>O<sub>3</sub> is considered as an intermediate form between amorphous and  $\gamma$ -crystalline Al<sub>2</sub>O<sub>3</sub>. Thompson and Wood suggested that aluminum oxides may consist of nanocrystallites, hydrated alumina, anions, and water molecules [20, 24].

## 1.4 Barrier-type and porous-type alumina

Depending on several factors, in particular the electrolyte, two types of anodic films can be produced. Barrier type films can be formed in completely insoluble electrolytes ( 5 < pH < 7 ), e.g., neutral boric acid, ammonium borate, tartrate, and ammonium tetraborate in ethylene glycol. Porous type films can be created in slightly soluble electrolytes such as sulfuric, phosphoric, chromic and oxalic acid [19, 37].

### 1.4.1 Inner and outer oxide layer

As shown in Fig. 1.1, both the barrier-type and the porous-type alumina films consist of an inner oxide of high purity alumina and an outer oxide layer comprised of alumina which has incorporated anions [18, 20, 24, 41]. In fact, the nomenclature of the inner and the outer oxide are determined in terms of the interfaces. The inner oxide is adjacent to the oxide/metal interface, while the outer oxide is adjacent to the electrolyte/oxide interface.

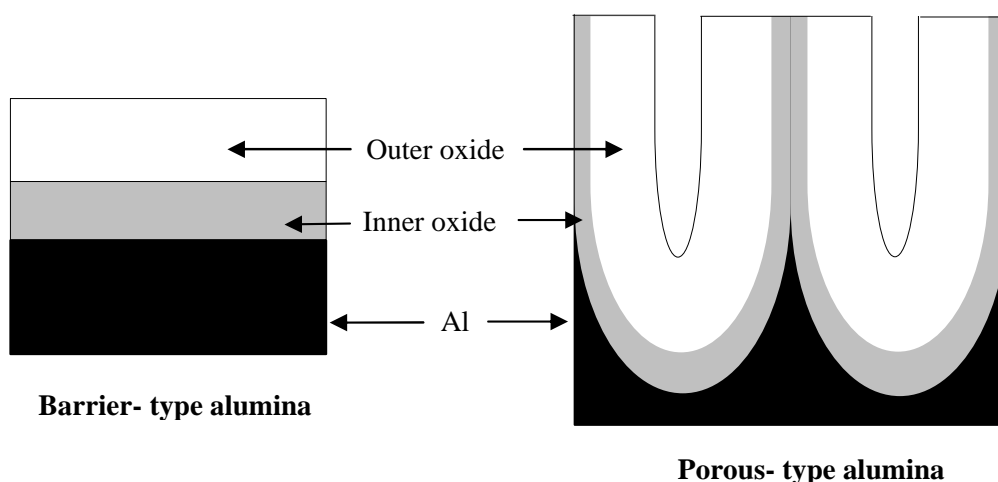


**Figure 1.1:** Schematic diagram for barrier type alumina and porous type alumina. The aluminum metal, an inner oxide consisting of pure alumina and an outer oxide consisting of an anion-contaminated alumina are indicated.

According to the Manchester group [20, 21, 22, 23, 24], the degree of incorporation of electrolyte species in the outer oxide layer of barrier-type alumina strongly depends on the type of electrolyte, the concentration of adsorbed anions, and the faradaic efficiency of film growth. This group found that the electrolytes can be classified into three categories in terms of ionic

Immobile species	Outwardly mobile species	Inwardly mobile species
Silicate, Arsenate	Antimonate, Chromate, Borate, Molybdate	Phosphate, Sulfate, Selenate

**Table 1.2:** Mobility of species in the outer oxide of barrier-type alumina. [23]

mobility in the oxide; immobile, outwardly mobile, and inwardly mobile ions. Table 1.2 shows the direction of the mobility of electrolyte species, which is determined by the type of the charge of electrolyte species in the film. For example, if the incorporated species are cations, they would move outwardly during the anodic reaction in Al. Immobility of electrolyte species can be attributed to effectively no charge in the film (compensated or low mobility). Therefore, the thickness of the outer oxide film is strongly influenced by the directionality of the electrolyte species.

### 1.4.2 Oxide thickness as a function of applied potential

Metal	Anodizing ratio ( $\text{\AA V}^{-1}$ )
Tantalum	16.0
Niobium	22.0
Zirconium	20 ~ 27
Tungsten	18
Silicon	4 - 8
Aluminum	10.0 in 15 % sulfuric acid 11.8 in 2 % oxalic acid 11.9 in 4 % phosphoric acid 12.5 in 3 % chromic acid 13 ~ 13.7 in barrier-type electrolytes

**Table 1.3:** Anodizing ratios for barrier film formation on valve metals. Note that in the case of aluminum anodized in sulfuric, oxalic, phosphoric, and chromic acid, anodizing ratios of the barrier layer formed beneath the porous alumina are indicated [19].

It is generally accepted that the thickness of barrier-type alumina is mainly determined by the applied voltage, even though there is a small deviation depending on the electrolytes and temperature [19, 24, 42, 43]. The anodizing ratio, which is defined as oxide thickness formed per volt, demonstrates that the barrier type films are also strongly influenced by the type of metal which is anodized as shown in table 1.3.

The maximum attainable thickness in the barrier-type alumina film was reported to be less than 1  $\mu\text{m}$ , corresponding to breakdown voltages in the range of 500 ~ 700 V. Above the limited voltage (or actually the breakdown electric fields,  $E_{B0}$ ), dielectric breakdown of the films occurs [19].

On the other hand, since the thickness in the porous alumina film is time-dependent, much thicker films than those in barrier-type films can be obtained [19]. Anodizing time, current density and electrolytes are important parameters in determining the film thickness of porous alumina. For instance, thick, compact, and hard porous films are formed at low temperatures ( $0^\circ < T < 5^\circ$ , so-called hard anodizing conditions), whereas thin, soft, and non-protective films are produced at high temperature ( $60^\circ < T < 75^\circ$ , so-called soft anodizing conditions). As the temperature increases, the corresponding current density also increases. This does not mean that a higher current density increases the film thickness since the rate of complex dissolution at the electrolyte/oxide interface increases, too. If the temperature is too high so that

the rate of dissolution is faster than that of oxide formation, the film even vanishes, resulting in electropolishing of aluminum [19, 37].

The thickness of the thin barrier layer at the bottom of the porous structure is only dependent on the anodizing voltage, regardless of anodizing time. However, electrolyte effects on the anodizing ratio in the barrier films have to be considered. For example,  $14\text{\AA}/\text{V}$ ,  $8\text{\AA}/\text{V}$ , and only  $1\text{\AA}/\text{V}$  were reported in a dilute, 40, and 90 % (w/w)<sup>3</sup> sulfuric acid, respectively [19, 42]. Comparing the anodizing ratio of the barrier-type oxide formed in non-dissolving electrolytes, the electrolyte effect can be ascribed to the dissolution of the formed oxide in acidic electrolytes.

### 1.4.3 Pore formation mechanisms

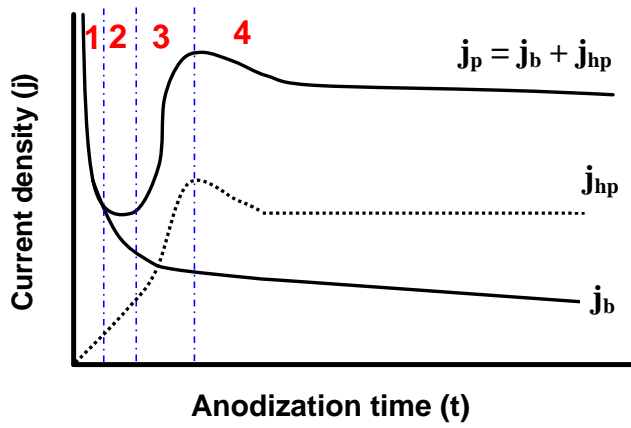


**Figure 1.2:** Schematic diagram of current density curve during the initial growth ( $< 1\text{h}$ ) at constant voltage.  $j_b$  and  $j_p$  indicate the current density for the barrier film and the porous film formation, respectively.  $j_{hp}$  represents a hypothetical current density, which is the difference between  $j_p$  and  $j_b$ .

The transient of the potentiostatic current density reflects the formation of barrier-type or porous-type porous alumina (see Fig. 1.2) [19, 36, 44, 45, 46]. At the beginning of the oxide formation, both transients have an identical behavior. However, for the barrier film formation, the current density  $j_b$  decays exponentially. Eventually, the barrier film current is dominated by an ionic current  $j_i$ .

In the case of the formation of porous films, the following current density profiles are typically observed [19, 36, 44, 45, 46]. First, the current density  $j_p$  decreases rapidly (regime 1 in Fig. 1.2). Then, it passes through minimum value (regime 2 in Fig. 1.2). It increases to arrive at a maximum value (regime 3 in Fig. 1.2). Subsequently, it slightly decreases again. Finally, a steady current density remains (regime 4 in Fig. 1.2). One can consider the current density  $j_p$  as the sum of  $j_b$  and hypothetical current density  $j_{hp}$ , which means the pure current density for creating pores.  $j_b$  is determined by the applied potential in terms of the anodizing ratio, while  $j_{hp}$  depends on the electrolyte and the temperature as well as on the applied potential.

The pore formation mechanism is displayed schematically in Fig. 1.3, corresponding to the four regimes of Fig. 1.2 [26]. At the beginning of the anodization, the barrier film, which consists of non-conductive oxide ( $= 10^{10} \sim 10^{12} \Omega \text{ cm}$  [47]), covers the entire surface of the aluminum (regime 1 in Fig. 1.2 and Fig. 1.3). The electric field is focused locally on fluctuations of the surface (regime 2 in Fig. 1.2 and Fig. 1.3). This leads to field-enhanced or/and temperature-enhanced dissolution in the formed oxide and thus to the growth of pores (regime 3 in Fig. 1.2 and Fig. 1.3). Since some pores begin to stop growing due to competition among the pores, the current decreases again as shown in regime 4 in Fig. 1.2. Finally,  $j_p$  maintains an equilibrated

<sup>3</sup>weight/weight percent = grams of solute /grams of solution  $\times 100$

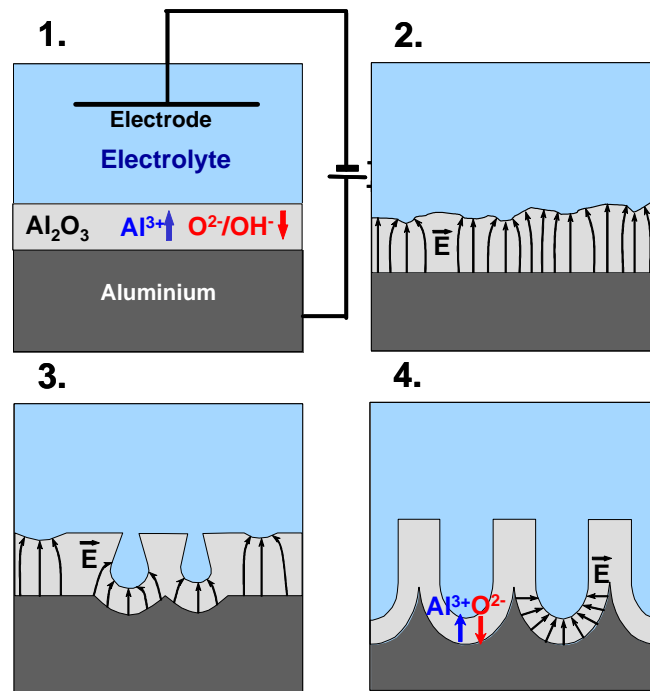


**Figure 1.3:** Schematic diagram of the pore formation at the beginning of the anodization. Regime 1: formation of barrier oxide on the entire area; regime 2: local field distributions caused by surface fluctuations; regime 3: creation of pores by field-enhanced or/and temperature-enhanced dissolution; regime 4: stable pore growth.

state. In this stage, pores grow in a stable manner. However, it is very often observed that during the stable pore growth, the current density continues to decrease slightly. This is due to diffusion limits in the long pore channels [45, 46].

## 1.5 Self-ordered porous alumina - current state-of-the-art

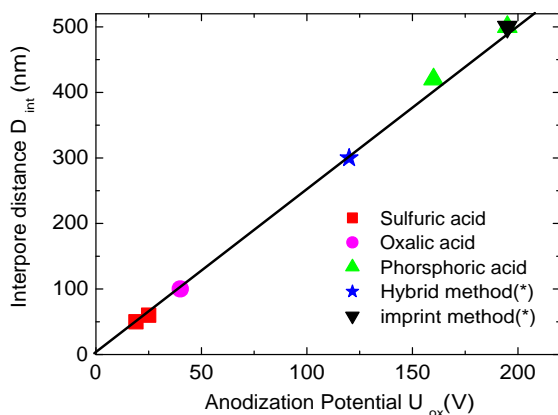
The method discovered by Masuda *et al.* relies on self-ordering of pores at the bottom of porous alumina channels after a long first-anodization step [34]. The driving force for self-assembly has been attributed to mechanical stress caused by the repulsive forces between neighboring pores during anodization [48, 49].<sup>4</sup>

Several previous studies revealed that self-ordered porous alumina structures can only be obtained under specific conditions. For example, structures with pore spacing of 50, 65, 100, 420 and 500 nm are fabricated at 19 V and 25 V in sulfuric acid, at 40 V in oxalic acid, and at 160 V and 195 V in phosphoric acid, respectively [46, 50, 51, 52], as seen in Fig. 1.4.

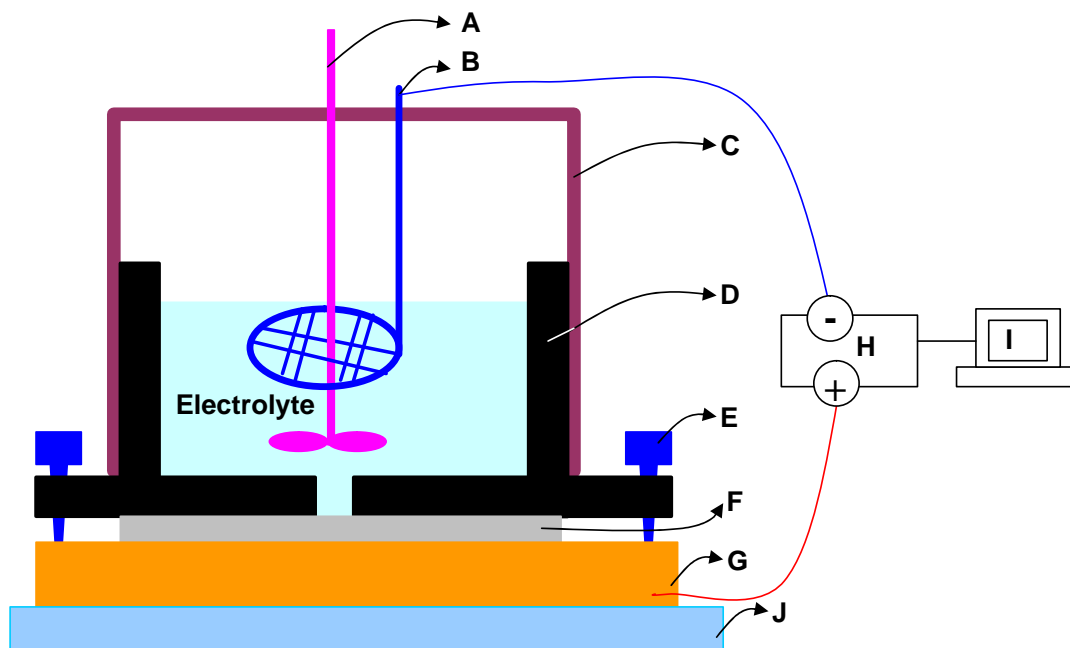
### 1.5.1 Experimental set-up

Fig. 1.5 shows an apparatus of our electrochemical experiments (anodization and electrochemical deposition) [44, 45]. The electrochemical cell consists of a two-electrode system, e.g., the Platinum (Pt) mesh acting as the counter electrode (**B** in Fig. 1.5) and Al sheet acting as the working electrode (**F** in Fig. 1.5). The Al sheet is inserted between the electrolyte container

<sup>4</sup>It will be discussed in detail in the Section 1.5.3.



**Figure 1.4:** Interpore distance as a function of the applied potential. The known self-ordering regimes are shown as symbols. The line is a fit to the data with a proportional constant  $k = 2.5 \text{ nm/V}$ . (\*) Imprint and hybrid method will be discussed in the Chapter 3 and 4, respectively.



**Figure 1.5:** Schematic diagram of the apparatus used for the anodization. A: Motor-controlled rotator for agitating the electrolyte, B: Pt mesh working as counter electrode, C: isolator consisting of an outer styrofoam layer and inner brass layer, D: electrolyte container made of teflon, E: screw for fixing the electrolyte container to the brass plate, F: aluminum sheet, G: brass plate working as electric conductor connected with a positive electric source, H : potentiostat/galvanostat (Keithley), and I: computer to operate the potentiostat/galvanostat and the cooling, J: Peltier cooling element.

(**D** in Fig. 1.5) and brass plate (**G** in Fig. 1.5) and fixed by screws (**E** in Fig. 1.5). To stir the electrolytes vigorously, a motor-controlled agitator is used (**A** in Fig. 1.5). The apparatus is operated by a computer (**I** in Fig. 1.5), using home-made software. The cell was clad with styrofoam acting as the thermal insulator (**C** in Fig. 1.5). For cooling the apparatus, a combination of water-cooling and a Peltier element is employed (**J** in Fig. 1.5). The potentiostat/galvanostat (Keithley 2400) has a working range of either 0 ~ 210 V (potentiostatic mode) or 0 ~ 100 mA (galvanostatic mode) as shown in **H** of Fig. 1.5.

## 1.5.2 Self-ordered alumina by 2-step anodization

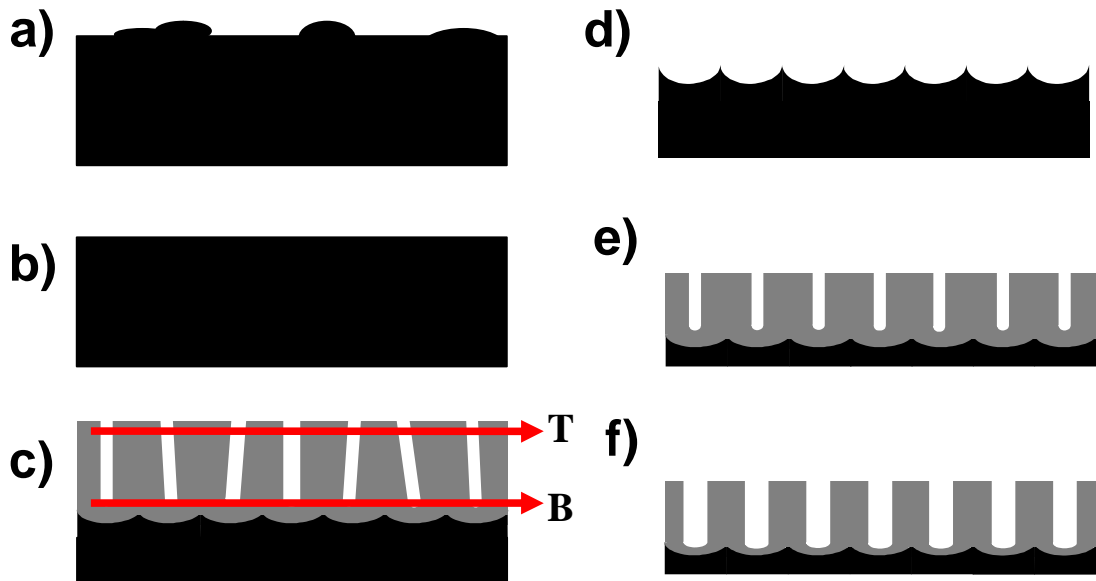


**Figure 1.6:** Stages of the formation of self-ordered alumina: a) Annealing at 500°C for 3h; b) electropolishing in a solution of 1/4 HClO<sub>4</sub> + 3/4 C<sub>2</sub>H<sub>5</sub>OH for 4 min at 8 V with agitation; c) first anodization (typically 1 ~ 2 days); d) selective dissolution of the formed oxide layer; e) second anodization under the same conditions as the first anodization; and f) isotropic etching in 1 M phosphoric acid at 30°C to widen the pores.

Experimental procedures are described in detail in Fig. 1.6 [44, 45]. Firstly, aluminum with a high purity (99.99 %) is cleaned with acetone in an ultrasonic bath. Then, it is immersed in 100 ml of a mixture containing HF/HNO<sub>3</sub>/HCl/H<sub>2</sub>O at a ratio of 1:10:20:69 in order to remove impurities on the surface. After cleaning with deionized (DI) water ( $\Omega\text{m}^2 > 10^6$ ), Al is annealed for 3 h at 500 °C in N<sub>2</sub> to obtain large single crystalline grains. As a matter of fact, the larger the grains are, the larger are the domains of self-ordered porous alumina (see Fig. 1.6 (a)). To reduce surface roughness, electropolishing is carried out in a mixture consisting of 1/4 HClO<sub>4</sub> + 3/4 C<sub>2</sub>H<sub>5</sub>OH (Fig. 1.6 (b)). Electropolishing is a prerequisite for the formation of self-ordered porous alumina with large domain size. Note that caution is needed when perchloric acid/ethanol is used due to its explosiveness at moderate temperatures.

After the pretreatment, anodization is performed either at 19 V in 2 M H<sub>2</sub>SO<sub>4</sub>, at 25 V in 0.3 M H<sub>2</sub>SO<sub>4</sub>, at 40 V in 0.3 M (COOH)<sub>2</sub>, at 160 V in 1 M H<sub>3</sub>PO<sub>4</sub>, or at 195 V in 0.1 M H<sub>3</sub>PO<sub>4</sub> for more than 1 day (Fig. 1.6 (c)). Since pores are randomly created on the surface, the initial pore arrangement is very irregular (Fig. 1.7 (a)). However, due to the repulsive forces between neighboring pores during the long-anodization, self-organization occurs. As a result, hexagonally close-packed arrays are obtained at the interface between the porous alumina layer and the

aluminum substrate ((Fig. 1.7 (b))). Then, the porous alumina film is selectively dissolved in a solution containing chromic acid (Fig. 1.6 (d)) [53]. Patterns that are replicas of the hexagonal pore array are preserved on the fresh aluminium surface. This allows the preparation of pores with a high regularity by a subsequent second anodization under the same conditions as the first anodization (Fig. 1.6 (e)). If needed, the resulting pores can be isotropically widened by chemical etching with 0.5 ~ 1 M phosphoric acid (Fig. 1.6 (f)).

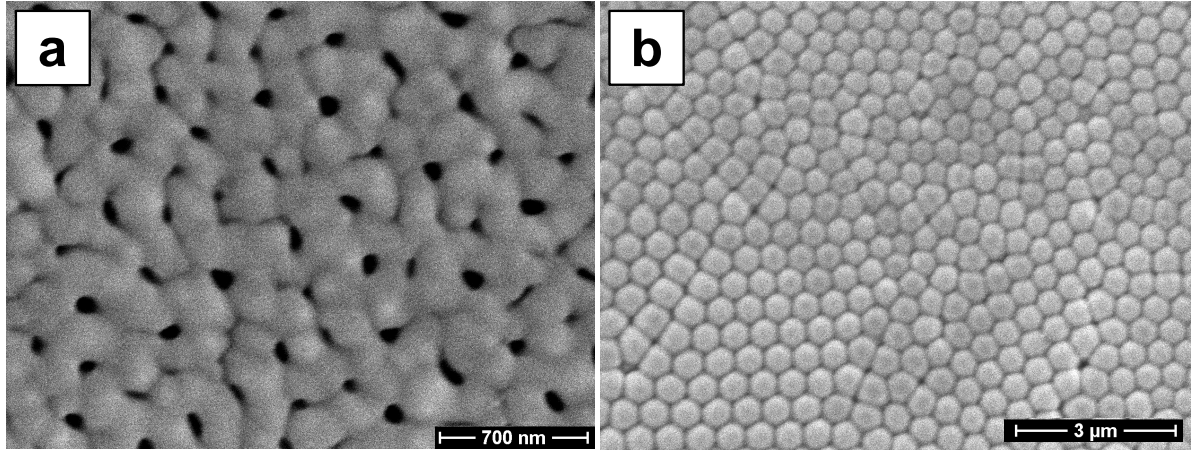


**Figure 1.7:** Scanning Electron Microscopy (SEM) images of a porous alumina sample produced by a first anodization (in 0.1 M phosphoric acid at 195 V). (a) the surface, and (b) the bottom of the membrane after selective removal of Al, which correspond to **T** and **B** in Fig. 1.6 (c), respectively

### 1.5.3 The mechanical stress model

Jessensky *et al.* and Li *et al.* proposed a mechanical stress model to explain the formation of hexagonally-ordered pore arrays [48, 52]. They considered the following factors;

1. The oxidation takes place at the entire metal/oxide interface mainly by the migration of oxygen containing ions ( $O^{2-}$  or  $OH^-$ ) from the electrolyte.
2. The dissolution and thinning of the oxide layer is mainly due to the hydration reaction of the formed oxide layer.
3. In the case of barrier oxide growth without pore formation, all  $Al^{3+}$  ions reaching the electrolyte/oxide interface contribute to oxide formation. On the other hand, porous alumina is formed when  $Al^{3+}$  ions drift through the oxide layer. Some of them are ejected into the electrolyte without contributing to the oxide formation.
4. Pores grow perpendicular to the surface when the field-enhanced dissolution at the electrolyte/oxide interface is equilibrated with oxide growth at the oxide/metal interface.
5. The formed alumina is assumed to be  $Al_2O_3$ . Therefore, the atomic density of aluminium in alumina is by a factor of 2 lower than in metallic aluminium. This means that the volume of the anodized alumina expands to about twice the original volume.
6. This volume expansion leads to compressive stress during the oxide formation in the oxide/metal interface. The expansion in the vertical direction pushes the pore walls upwards.

According to their studies, the degree of the volume expansion of aluminum, the volume expansion coefficient  $\xi$  (see Eq. 2.5), varies with the applied potential and determines either the

formation of self-ordered pores or the formation of disordered pores. If the stress is maximal ( $\xi_{max} \sim 2$ ), no pores are generated. If the stress is too small ( $\xi < 1.2$ ), the force promoting ordering is too small and a disordered porous alumina array is formed. In the case of moderate promoting forces ( $\xi \simeq 1.2$ ), ordered pore growth occurs. If  $1.3 < \xi < \xi_{max}$ , the size of domains of self-ordered porous alumina will decrease and finally disappear due to the strong repulsive interactions. They concluded that self-ordered porous alumina is best formed when the volume expansion coefficient  $\xi \approx 1.2$ .

## 1.5.4 Anodization parameters influencing self-ordering

### Potential

The applied potential,  $U$ , is one of the most important factors to adjust self-assembly of porous alumina. As seen in Fig. 1.4, the interpore distance,  $D_{int}$ , is linearly proportional to the applied potential with a proportionality constant  $k$  of approximately  $2.5 \leq k(nm/V) \leq 2.8$  [18, 24].

$$D_{int} = kU \quad (1.9)$$

In addition, the thickness of the barrier layer can be approximately estimated as half of the interpore distance ( $D_{int} = 2D_B$ , where  $D_B$  is the barrier-layer thickness).

### Type and concentration of the electrolyte

The type and the concentration of the electrolyte for a given potential has to be selected properly to obtain self-ordered pore growth. In other words, the choice of the type of electrolyte is restricted. Usually, the anodization of aluminium is carried out in sulfuric acid in low potential ranges (ca. 5 ~ 40 V), oxalic acid is used for medium potential ranges (ca. 30 ~ 120 V) and phosphoric acid for high potential ranges (ca. 80 ~ 200 V). This restriction is due to the conductivity and pH value of the electrolyte. For example, if aluminum is anodized in sulfuric acid at a high potential (note that sulfuric acid has a very high conductivity), breakdown of the oxide layer takes place very often. In addition, the pH-value of the electrolyte determines the size of the pores. The lower the pH value, the lower the potential threshold for field-enhanced dissolution at the pore tip. This leads to a smaller size of the pores. Therefore, large pore diameters are formed by using the phosphoric acid, and small pore diameter are obtained by using sulfuric acid [24, 41].

### Temperature dependence

During the anodization, temperature should be kept lower than room temperature to prevent the formed oxide structure from being dissolved in acidic electrolytes. For instance, anodization at 40 V in oxalic acid is performed at 5 ~ 18°C and at 0 ~ 2°C in the case of anodization at 195 V in phosphoric acid. A second reason to keep the temperature as low as possible is to avoid a local heating at the bottom of the pores during the course of anodization (specially, in the case of anodization at a high potential). The local heat causes an inhomogeneous electric field distribution at the bottom, leading to local electrical breakdown of the oxide (see Fig. 1.8). In fact, cracks and bursts of the oxide film are generated if porous alumina is formed without temperature controlling. If the temperature is too low (just below zero degree) and diluted electrolytes are used, the electrolyte may freeze. In addition, the speed of the growth of porous alumina is affected by the temperature. The lower the temperature, the lower is the growth rate.

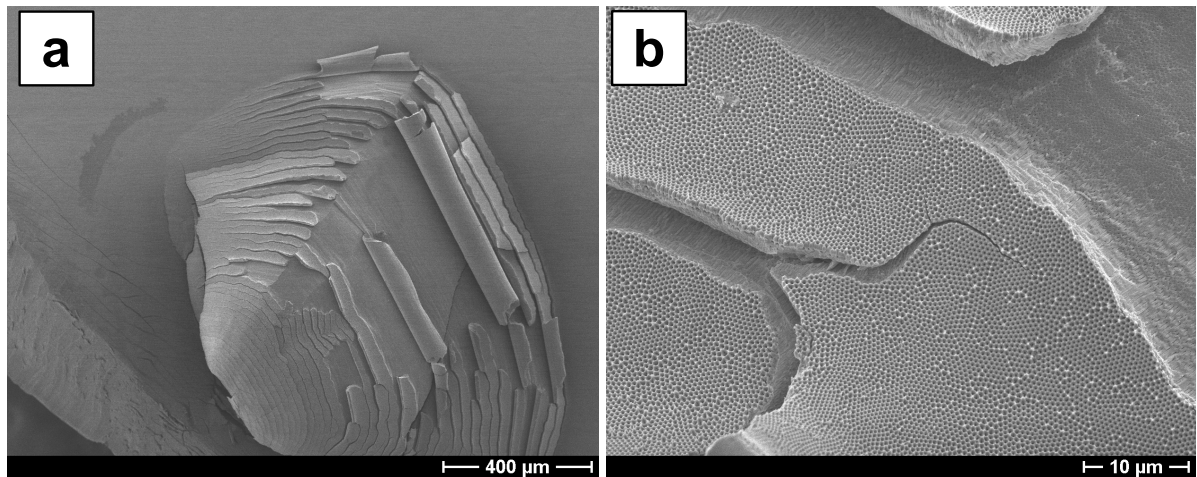


**Figure 1.8:** (a) SEM image of porous oxide after electrical breakdown caused by local heating. Enlarged the image is shown in Fig. 1.8 (b).

### **Influence of impurity**

Aluminum with a high purity ( $\geq 99.99\%$ ) is usually recommended to obtain self-ordered porous alumina. It is reasonable to expect that anodization of aluminum having impurities leads to defects since impurities have a different volume expansion coefficient than aluminum. To my knowledge there are no investigations about the effect of impurities on the self-ordering. In the next chapter (see chapter 3), we will discuss these effects.

### **Other important parameters**

Additionally, annealing, electro-polishing, agitating, and the first anodizing time are important parameters to be considered to fabricate self-ordered porous alumina structures with large domain sizes.

- The aluminum substrate is annealed below the melting point to obtain a large grain size (see Fig.1.6 (a)). Usually, an annealing process is performed at 500 °C for 3h (note that the melting point of Al is 680 °C).
- The surface roughness is smoothed by electropolishing (see Fig.1.6 (b)) [49]. Usually, the electropolishing is performed for 1 ~ 4 min.
- During the anodization, the electrolyte should be vigorously stirred to effectively remove hydrogen bubbles and local heat on the surface, and to allow a homogenous diffusion of anions into pore channels [49].
- The first anodizing time affects the size of domains of self-ordered porous alumina. It turned out that the domain size increases with the first anodizing time [54]. However, it was also found that the average of domain sizes decreased again if Al is anodized over a critical time (see next chapter).

## 2. Self-ordered porous alumina - new insight in growth

As already discussed in the previous chapter, self-ordering phenomena in porous alumina are only observed under specific anodization conditions (see Fig. 1.4). Here, new insight in the self-ordered pore growth associated with specific anodization conditions will be presented [41].

### 2.1 The 10% porosity rule

Cell structures of self-ordered porous alumina have been analyzed in detail by transmission electron microscopy (TEM). Figure 2.1 shows TEM images of porous alumina with well-arranged arrays anodized in  $H_2SO_4$ ,  $(COOH)_2$ , and  $H_3PO_4$ , respectively. It is obvious from the three pictures that walls between pores consist of a dark inner layer, far from the pore, and a relatively bright outer layer. This contrast can be explained by the fact that the outer layer is anion-contaminated, whereas the inner layer consists of dense pure alumina [20]. Numerical analysis of the pictures reveals that the ratio of the radius of the pores  $r$  to the interpore spacing  $D_{int}$  is constant. Furthermore, the ratios of  $D_{inner}/D_{outer}$  are constant and about  $0.2 \pm 0.02$  for all self-ordering regimes (see Table 2.1). Interestingly, Thompson *et al.* found that the thickness ratio of the inner to the outer layer strongly depends on the acid. For example,  $D_{inner}/D_{outer} = 0.05$  for  $H_2SO_4$ , 0.1 for  $(COOH)_2$ , and 0.5 for  $H_3PO_4$  [20]. However, they had concentrated their work on disordered pore regimes. In the case of well-defined self-ordered porous alumina, the same  $r/D_{int}$  as well as the same  $D_{inner}/D_{outer}$  are always observed. It could be deduced that the optimum porosity for the self-ordering is around 10 %, since  $r/D_{inner}$  is constant (see Table 2.1) and the definition of the porosity in a hexagonal structure is given by

$$P = \frac{2\pi}{\sqrt{3}} \left( \frac{r}{D_{int}} \right)^2 \quad (2.1)$$

electrolyte	interpore distance $D_{int}$	inner wall thickness $D_{inner}$	pore diameter $D_p (= 2r)$	porosity $P$	$pK_s$
$H_2SO_4$	66.3 nm	7.2 nm	24 nm	12 %	0.1
$(COOH)_2$	105 nm	9.1 nm	31 nm	8 %	1.125
$H_3PO_4$	501 nm	54 nm	158.4 nm	9 %	2.1

**Table 2.1:** Results of structural properties of self-ordered porous alumina obtained from the TEM images in Figure 2.1

Note that the slightly larger pore diameter of the  $H_2SO_4$  sample is due to chemical attack of the pore walls. For comparison, the porosity in the disordered growth regime is significantly larger or even smaller than 10 %. For example, using 160 V instead of 195 V in 0.1 M  $H_3PO_4$ , the porosity is about 40 %.

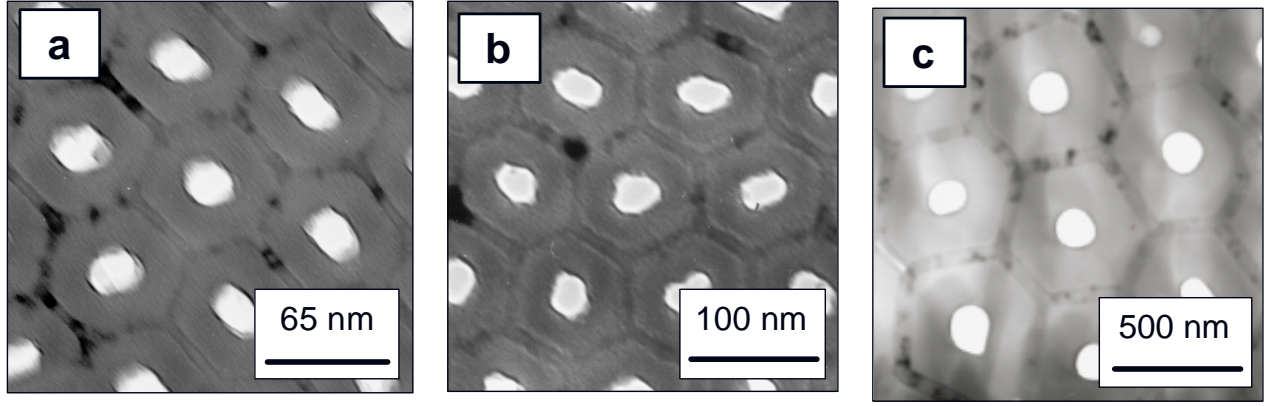


**Figure 2.1:** Transmission electron micrographs of self-ordered porous alumina fabricated at (a) 25 V in 0.3 M  $\text{H}_2\text{SO}_4$ , (b) 40 V in 0.3 M  $(\text{COOH})_2$ , and (c) 195 V in 0.1 M  $\text{H}_3\text{PO}_4$ .

As already discussed in the section 1.5.4,  $D_{int}$  is linearly proportional to the applied cell potential  $U$  with a proportionality constant  $k$  ( $2.5 \text{ nm/V} \leq k \leq 2.8 \text{ nm/V}$ )

$$D_{int} = kU. \quad (2.2)$$

From experimental observations of the 10% porosity rule, Eq. 2.2 can be written for self-ordered pore growth as

$$U = \sqrt{\frac{2\pi}{\sqrt{3}P}} \frac{r}{k} \quad (2.3)$$

where, under optimum self-ordering conditions,  $P = 10\%$ . Eq. 2.3 shows the required potential  $U$  to obtain self-ordered growth for a given pore radius determined by the pH-value. As a matter of fact,  $\text{H}_2\text{SO}_4$ ,  $(\text{COOH})_2$ , and  $\text{H}_3\text{PO}_4$  have different pH values. Therefore, different self-ordering regimes for different potentials are obtained (Eq. 2.3). Moreover, changing the concentration would also lead to a change of the pH value. Indeed, increasing the concentration by a factor of 10, leads to a 20% decrease in the optimum interpore distance. For example, increasing from 0.3 to 2 M  $\text{H}_2\text{SO}_4$  leads to a reduction of the lattice constant from 65 to 50 nm. A similar relationship is also observed for  $\text{H}_3\text{PO}_4$ .

## 2.2 Relationship between the mechanical stress model and the 10% porosity rule

The observation of the 10% porosity rule strongly supports the mechanical stress model proposed by Jessensky *et al.* [44, 48, 52].

The total amount of Al ions in the electrolyte,  $\text{Al}_{aq}^{3+}$ , after anodization can be measured by atomic absorption spectroscopy. In addition, the total amount of oxidized aluminum atoms,  $\text{Al}_{tot}$ , is calculated from the charge flow during the anodization ( $\text{Al}_{tot} = \frac{1}{3} \int I dt$ ). According to the relationship between  $\text{Al}_{tot}$  and  $\text{Al}_{aq}^{3+}$ , the ratio of the weight of alumina to that of aluminum is determined by,

$$\frac{W_{Al_{ox}}}{W_{Al}} = 1 - \frac{\text{Al}_{aq}^{3+}}{\text{Al}_{tot}} \quad (2.4)$$

where  $W_{Al}$  and  $W_{AlOx}$  are the weight of aluminum and alumina, respectively.

The volume expansion  $\xi$  can be expressed by

$$\xi = \frac{V_{AlOx}}{V_{Al}} = \frac{W_{AlOx}}{W_{Al}} \times \frac{F_w \times \rho_{Al}}{\rho_{AlOx}} \quad (2.5)$$

where  $\rho_{Al}$ ,  $\rho_{AlOx}$ ,  $F_w$  are the density of aluminum (2.7 g/cm<sup>3</sup>), the density of porous alumina (3.2 g/cm<sup>3</sup>, measured value), and the weight fraction of aluminum ions in alumina (= 0.53), respectively.

In the case of self-ordered alumina, 23% Al<sup>3+</sup> ions are detected in the solution by atom absorption spectroscopy, taking into account that each aluminum atom needs three charges to dissolve. Thus, the self-ordered alumina maintains 77% of Al<sup>3+</sup> ions, which corresponds to a volume expansion by a factor of 1.23 (eq. 2.5). This is in a good agreement with the values of Jessenky *et al.* obtained from gravimetric measurements [48]. Also, it is in line with results obtained by Li *et al.* who performed measurements of thickness difference between non-anodized and anodized aluminum with a profiler assuming 10% porosity of porous alumina [52].

### 2.3 Deviations from the 10 % porosity rule

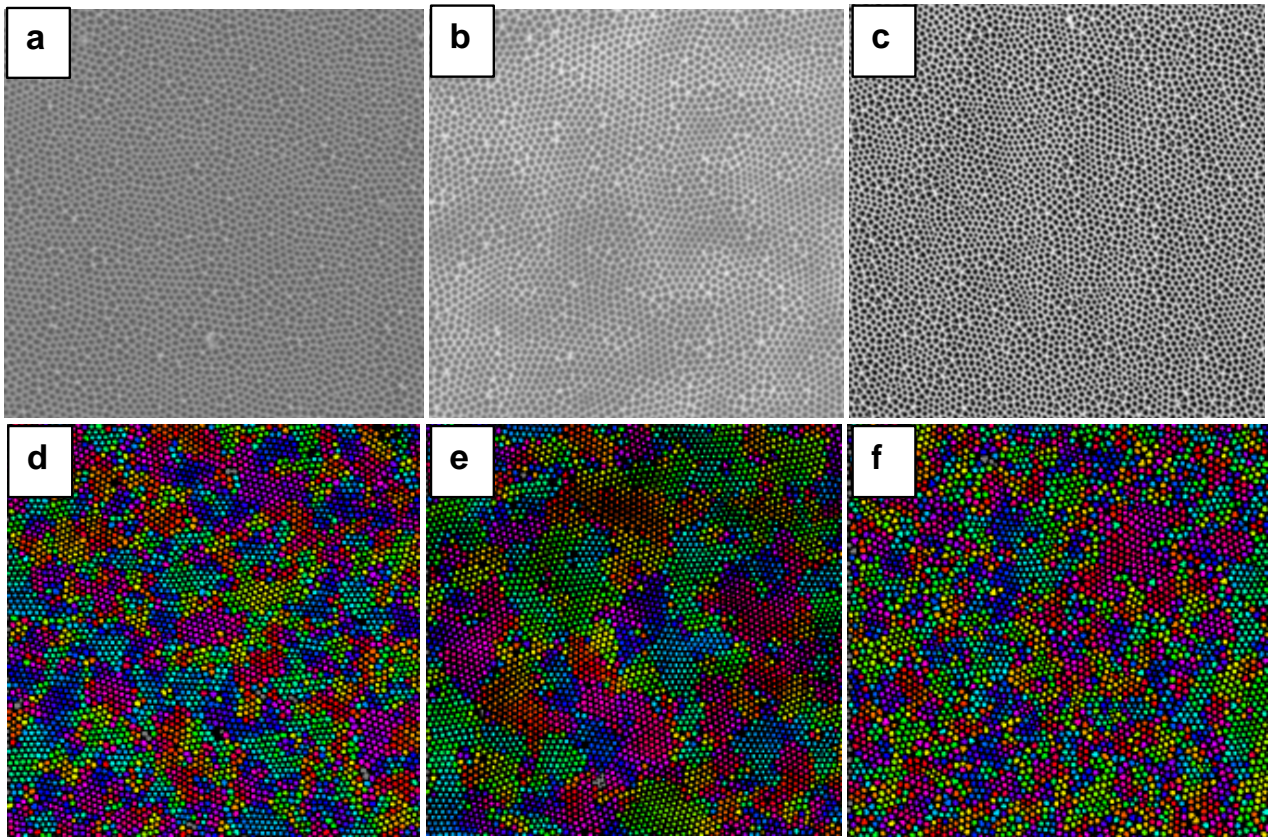


**Figure 2.2:** SEM images of polydomain porous alumina arrays formed at 195 V in 0.1 M phosphoric acid for (a) 6 h, (b) 24 h and (c) 36 h, resulting in 500 nm interpore distance. (d), (e) and (f): Numerical image treatment of (a), (b) and (c), respectively, showing the domain size in false colors.

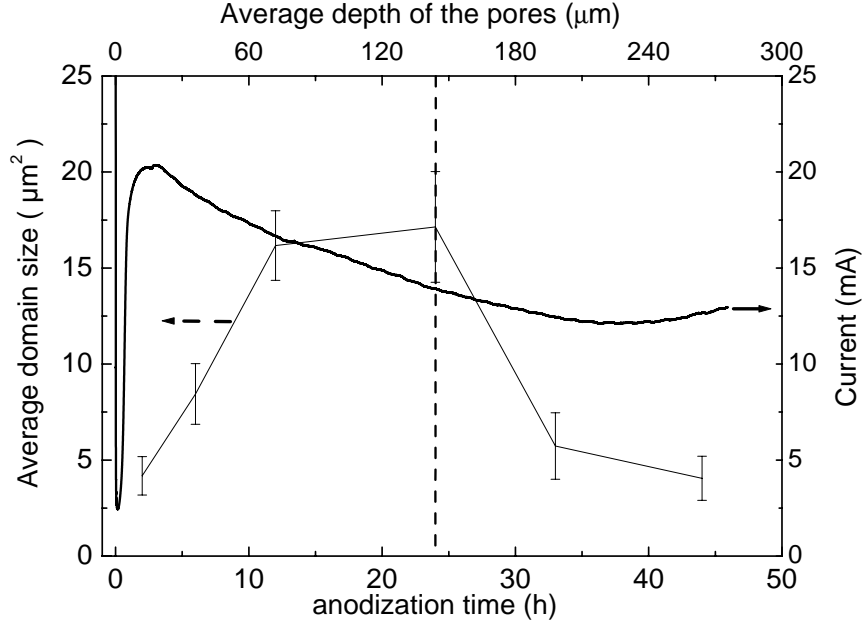


**Figure 2.3:** (left axis) Average domain size as a function of the anodization time during anodization in 0.1 M  $\text{H}_3\text{PO}_4$  at 195 V. The domain size is obtained by numerical picture treatment. First the domain size increases due to self-ordering, but after a critical time shown by the dashed line the domain size decreases again. (right axis) Current transient during anodization of the same sample, showing first a current decrease typical for self-ordering, and then, after a critical time, a current increase.

According to these findings, it can be expected that after long anodization times in the self-ordering regimes the 10% porosity rule cannot be maintained, since the conditions at the pore bottom will change due to diffusion limitations. Fig. 2.2 shows three SEM images of porous alumina obtained by anodization in  $\text{H}_3\text{PO}_4$  after 6 h (a), 24 h (b) and 36 h (c). Numerical image treatment (Fig. 2.2 (d), (e) and (f)) of these pictures shows that the size of the ordered domains (false colors) decreases with anodization time. Analysis of a series of porous alumina structures shows that the domain size does not linearly increase with time but has a maximum (Fig. 2.3). The reason that the domain size decreased after a critical time can be explained as deviation from the 10% porosity rule due to a change of the pH value at the pore tip. In addition, the shape of pores after long anodization is not any more circular as it is observed in the ordering regimes but rather triangular or polygonal. The current transient increases again after a critical time, implying the change of conditions at the tip (Fig. 2.3). These results suggest that there is an optimum anodization time to obtain the largest domain size. This goes beyond the results of Li *et al.* who reported that the average domain area is a linear function of anodization time [54].

## 2.4 Summary

The 10 % porosity rule in terms of anodization conditions was suggested to explain the self-ordering regimes. The experimental findings were in good agreement with the mechanical stress model [48]. In addition, an attainable maximum thickness for self-ordered porous alumina was explained by diffusion limitations in long channels associated with deviation from the 10 % porosity rule.

# 3. Monodomain porous alumina obtained by nanoimprint lithography

## 3.1 Nanoimprint lithography (NIL)

In the previous chapter, the preparation of polydomain porous alumina by self-ordering was discussed. In this chapter, the fabrication of monodomain porous alumina by means of nanoimprint lithography will be introduced.

Lithography using nanoindentation has emerged as a possibility to overcome the low throughput and the high equipment cost of conventional lithography technologies [55, 56]. 50 nm-resolution x-ray lithography and sub-25 nm resolution electron beam lithography are established, but the costs are still considerable. The principle of the nanoimprint lithography was suggested by Stephen Chou *et al.* in 1995. A master mold is fabricated by conventional lithography with high resolution, low throughput, and high cost. Afterward, the mold containing regular nanostructures is pressed into a thin resist film. Since the nanoimprint process enables to reproducibly transfer patterns of the master stamp onto the desired substrates, mass production with low cost and high resolution is possible. In addition, the master stamp is very durable if the stamping pressure is optimized. It was reported that the proper choice of resist (which should have characteristics of small pressure shrinkage, small thermal expansion, and a weak adhesion to the mold), mold release agents, and the optimum pressure to fully transfer patterns are vital factors [57].

## 3.2 Previous methods for pre-patterning Al substrates

### 3.2.1 Dot-like master stamp

The idea for the fabrication of a monodomain porous alumina structure with an extremely high aspect ratio was proposed initially by Masuda *et al.* in 1997 [35]. They prepared a master stamp consisting of hexagonal dot arrays with 150 nm lattice constant based on a SiC single-crystal wafer by e-beam lithography. The detailed procedure of the preparation of the master stamp is depicted in Fig. 3.1 [58]. The master stamp was placed on a polished Al sheet. Subsequently, the patterns were replicated on its surface by pressing the stamp on the substrate using an oil press under  $5 \text{ ton/cm}^2$ . The depth of the indented concave patterns was estimated to be 20 nm. According to the relationship between the interpore distance and applied potential, anodization was carried out at 60 V in 0.3 M oxalic acid. This generated porous alumina templates with defect-free long-range-ordered channels and an aspect ratio of 150 [35]. Later, Masuda's group showed that not only hexagonal but also square and honeycomb configurations can be fabricated in anodic alumina by using a master stamp having appropriate configurations before anodization [59]. In these cases, due to the abberation of the 10% porosity rule, the formed porous alumina

templates had very low aspect ratios. For example, the depth of the holes in the case of the porous alumina with the square configuration was less than  $1 \mu\text{m}$ . Recently, Masuda *et al.* have demonstrated the self-healing property of anodic porous alumina. Aluminum prepatterned by a master stamp decorated with a hexagonal array with periodic defects was anodized at an appropriate voltage [60]. During the anodization, pores were automatically created in the defect sites on the surface of aluminum. Finally, on the back side, there were no obvious differences between pores grown from defects and prepatterned sites.

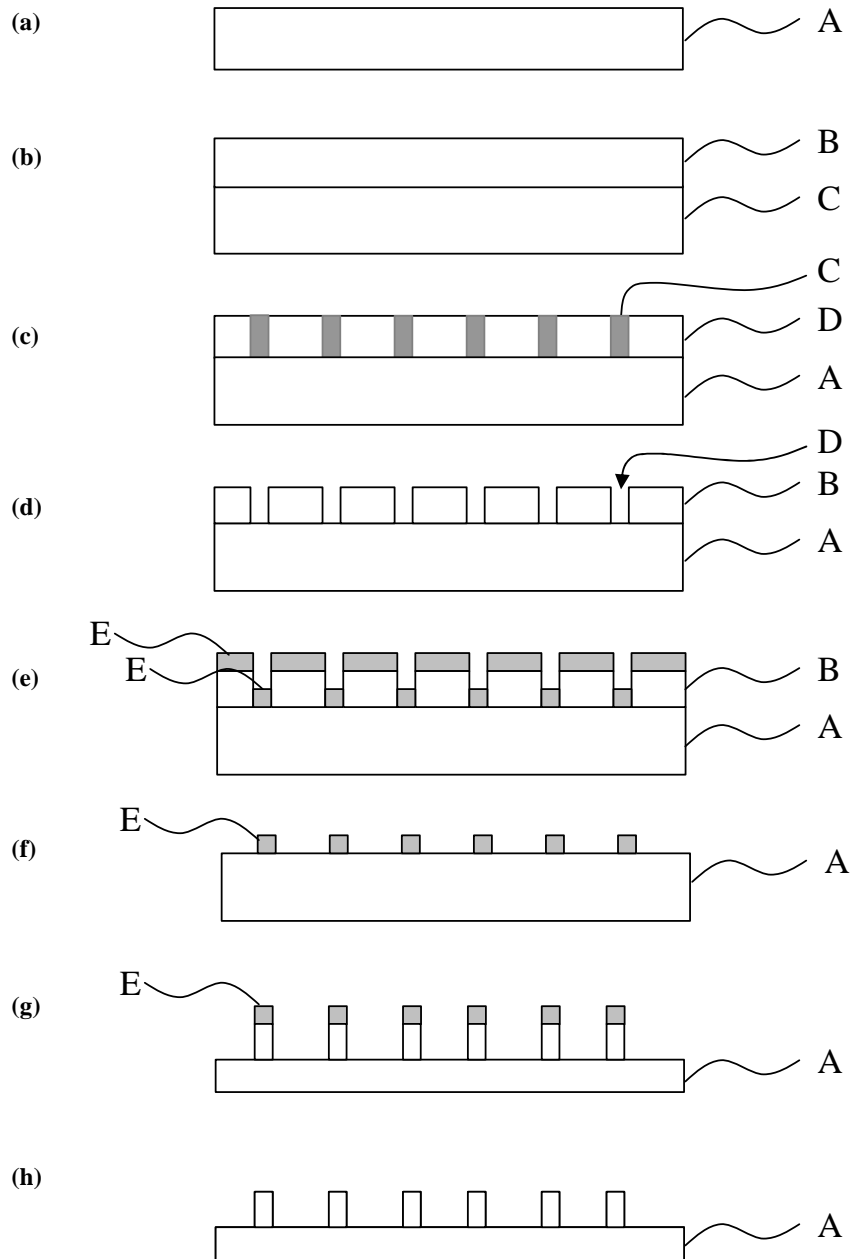


**Figure 3.1:** Fabrication procedures for the master stamp proposed by Masuda *et al.*; a) a SiC single-crystal wafer with a diameter of 2.5 cm acting as starting material, b) spinning of resist on the wafer, c) exposure to Gaussian beam (accelerating voltage of 25 kV), d) development of the exposed resist, e) lift-off process for Cr mask, f) removal of the resist, g) dry etching of SiC (parallel-plate RIE system), h) removal of Cr layer in cerium nitrate solution (A: a SiC single-crystal wafer, B: a positive electron beam resist, C: exposed sites by e-beam lithography, D: inverse etch pits, E: Cr mask) [58].

### 3.2.2 Direct writing on Al by lithography

Li *et al.* prepared monodomain porous alumina with 200 nm interpore distance and 50  $\mu\text{m}$  length via anodization of aluminum which had directly been patterned by conventional e-beam lithography [61]. They showed that the anodization conditions such as applied potential and electrolytes should match the pitch of prepatterns.

Liu *et al.* adopted the focus-ion-beam (FIB) technique to create prepatterns with depths of 4 nm [62]. They claimed that concaves as shallow as few nanometer would be sufficient to guide the growth of the pores by the subsequent anodization.

In both cases (e-beam and FIB lithographies), the polishing process to reduce the surface roughness was a vital step to correctly write the patterns on the surface.

### 3.2.3 2-step indentation using optical gratings with periodic lines

Mikulskas *et al.* reported that a regular groove mesh on the surface of Al can be formed by two successive indentations using commercially available optical diffraction grating [63]. For example, two consecutive indentation steps with a rotation by  $60^\circ$  in between allowed the formation of a profile of close-packed arrays. The used master stamp had line spacing of 833 nm (1:1200 lines per mm), which creates rhomb-shaped ridges with a period of 962 nm (determined as  $833 \text{ nm} / (\sin 60^\circ)$ ) in the profile (see Fig. 3.2 (a) and (b)). The subsequent anodization was carried out under the self-ordering condition in phosphoric acid corresponding to a period of the half of the distance between two intersections (i.e., 481 nm). The control of the angle and the identical pressure were required.

### 3.2.4 Thin Al films on prestructured Si

Sun *et al.* investigated the anodization of a thin film of Al on a silicon substrate which had been prestructured by a holographic lithography process [64]. Since the Al film was formed on a silica substrate having the corrugation profile, the pores can be only initiated in the valleys. They claimed that a contrast in thickness of about 100 nm is enough to guide pore growth during the subsequent anodization (see Fig. 3.3).

## 3.3 A novel imprint method

For mass production in the future, imprint methods are considered to be more suitable than the direct writing lithographies such as e-beam and FIB. However, up to now, the stamps which have been developed for imprinting allow only small imprint areas. Here, a novel 4'' imprint stamp consisting of regular arrays of  $\text{Si}_3\text{N}_4$  pyramids obtained by standard silicon processing techniques will be introduced.

### 3.3.1 Fabrication process of imprint stamp

In the following, the fabrication process of the imprint stamp is described. A master mold for stamping is fabricated from a 4'' silicon wafer (100) (Fig. 3.4 (a)). First of all,  $\text{SiO}_2$  is grown on the Si substrate by annealing (Fig. 3.4 (b)). Subsequently, a poly-methyl-methacrylate (PMMA)

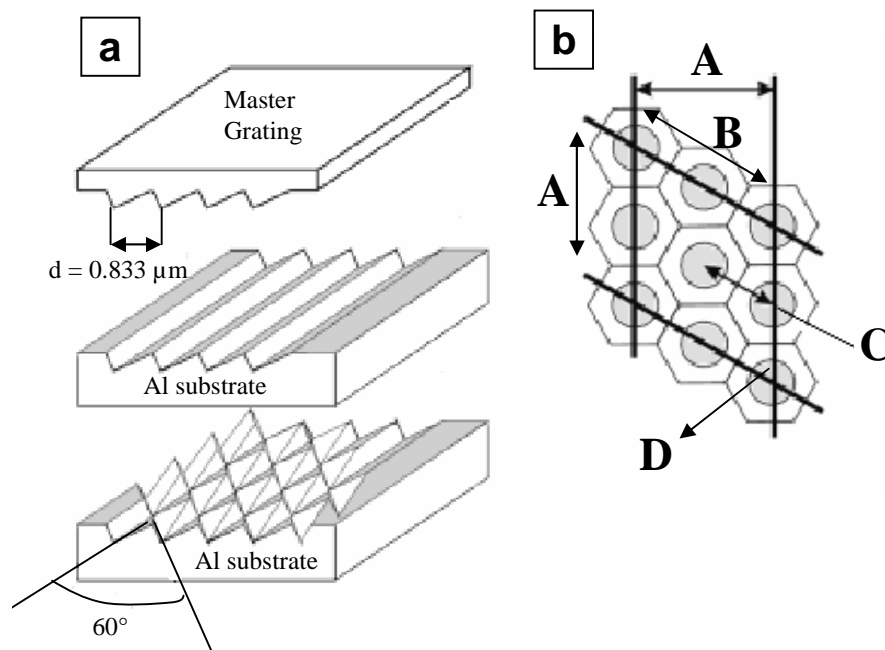


**Figure 3.2:** Schematic diagram of the cell configuration obtained by 2-step indentation by a rotation of  $60^\circ$ . (a) Depiction of experimental procedure. (b) The formation of a profile of close-packed arrays of rhomb-shaped ridges with a period of 962 nm. Bold lines show the dimensions of the pattern generated by stamping. A: line spacing ( $= 833 \text{ nm}$ ), B: distance between two intersections formed by 2-step indentation ( $= 962 \text{ nm}$ ), C: interpore distance ( $=$  the half of the distance between two intersections), D: angle of 2-step indentation ( $= 60^\circ$ ) [63].

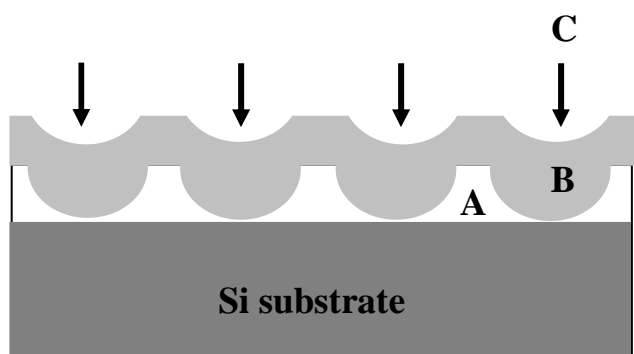


**Figure 3.3:** Schematic diagram of the corrugation profiles of the evaporated Al. Pores are created in the indents when Al is anodized (see C in the picture). A: photoresist, B: evaporated Al [64].

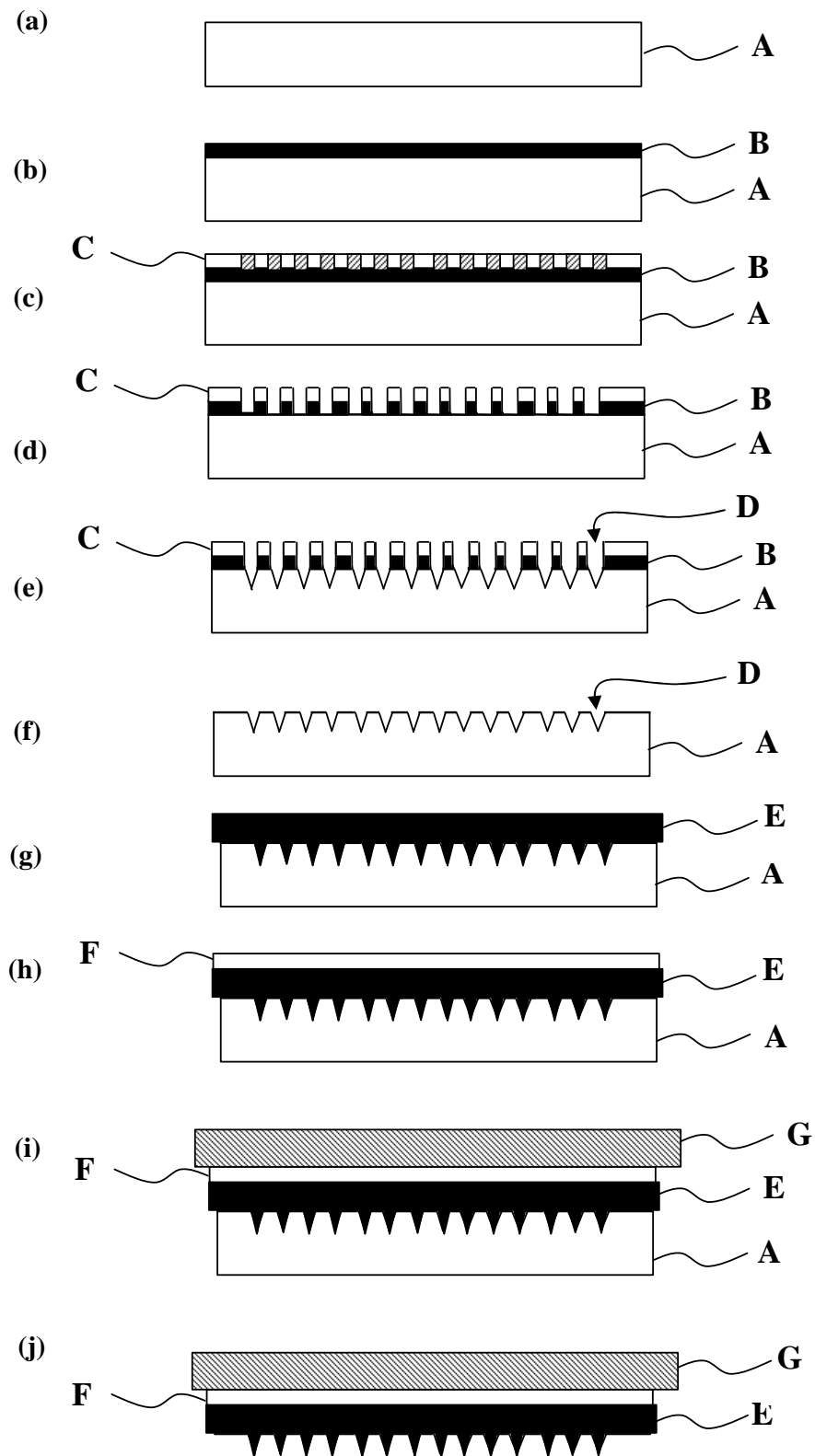


**Figure 3.4:** Fabrication procedures for master stamp with pyramids having 500 nm lattice constant; (a) a 4'' Si wafer, (b) SiO<sub>2</sub> grown on Si by annealing ( $T = 1000\text{ }^{\circ}\text{C}$ ), (c) deep-UV lithography ( $\lambda_{ex} = 248\text{ nm}$ ), (d) dissolution of the activated resist in developer, (e) anisotropic etching of Si in KOH, generating inverse pyramid pits, (f) removal of the remaining resist and SiO<sub>2</sub> in acetone and HF, respectively, (g) Si<sub>3</sub>N<sub>4</sub> CVD, (h) spin-on-glass (SOG), (i) bonding between Si wafer and SOG to obtain a stable stamp, (j) removal of the first Si wafer by mechanical polishing and wet etching. A: first Si wafer as starting material, B: SiO<sub>2</sub>, C: PMMA resist, D: inverse etch pits, E: Si<sub>3</sub>N<sub>4</sub>, F: spin-on-glass, G: second Si wafer for a easy handling.

resist is spun on the  $\text{SiO}_2$  grown on the Si. By using deep- $UV$  lithography ( $\lambda_{ex} = 248 \text{ nm}$ ), a 2D hexagonal array with a lattice constant of 500 nm and a pore diameter of 300 nm is patterned on the PMMA resist (Fig. 3.4 (c)). The activated pattern on the resist is developed in the developer (Fig. 3.4 (d)). Then, inverted pyramids are formed by anisotropic etching the pattern in KOH (Fig. 3.4 (e)). The remaining non-activated resist layer is removed in acetone. Subsequently,  $\text{SiO}_2$  is removed in HF (Fig. 3.4 (f)). A  $\text{Si}_3\text{N}_4$  layer is replicated on top of the patterned silicon by chemical vapor deposition (CVD) (Fig. 3.4 (g)). The thickness of the  $\text{Si}_3\text{N}_4$  layer is in the range of 300 to 500 nm.

For more stable bonding, spin-on-glass is added as adhesion promoter (Fig. 3.4 (h)). To obtain a stable stamp, another silicon substrate is waferbonded on top of the  $\text{Si}_3\text{N}_4$  layer so that the  $\text{Si}_3\text{N}_4$  was sandwiched between two silicon substrates (Fig. 3.4 (i)). Finally, the initially patterned silicon substrate is removed by grinding and selective spin-etching (Fig. 3.4 (j)).

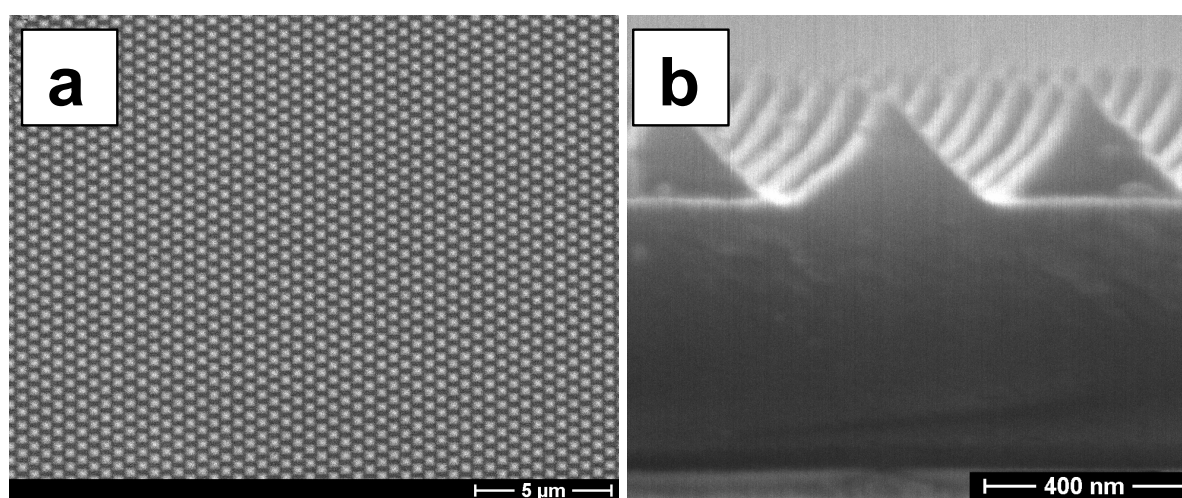


**Figure 3.5:** SEM image of the imprint master consisting of  $\text{Si}_3\text{N}_4$  pyramids with a 500 nm lattice constant and a 260 nm height: (a) Top view and (b) cross-section of the imprint master.

The master stamp consisting of a hexagonal lattice of pyramids with a height of about 260 nm and a lattice constant of 500 nm is shown in Fig. 3.5.

### 3.3.2 Nanoindentation

For the preparation of monodomain porous alumina, patterns on master stamps are transferred onto mechanically polished aluminum substrates (roughness,  $R_g < 100 \text{ nm}$ ) by a simple oil press (PW, Paul-Otto Weber GmbH). Fig. 3.6 (a) shows that the pattern of the master stamp is well transferred. The average depth of the prepatterns on the Al surface as a function of applied pressure is investigated by atomic force microscopy (Fig. 3.6 (b)). If the applied pressure is too high (here,  $> 10 \text{ kN/cm}^2$ ), the master stamp is very easy to be broken, while the patterns are only formed locally (non-patterned areas are found) if the pressure is too low. Even though homogenous pattern in depth and size are hard to achieve over large areas in the surface of a hard metal, subsequent anodization can compensate deviation of size and defects.

In fact, a pre-patterned hole with the depth of 20 nm is sufficient to guide the position of a pore formed by subsequent anodization. Therefore,  $5 \text{ kN/cm}^2$  allowing to form prepatterns with a depth of 50 nm is sufficient. Since a convex pyramid stamp is used, the stamping pressure

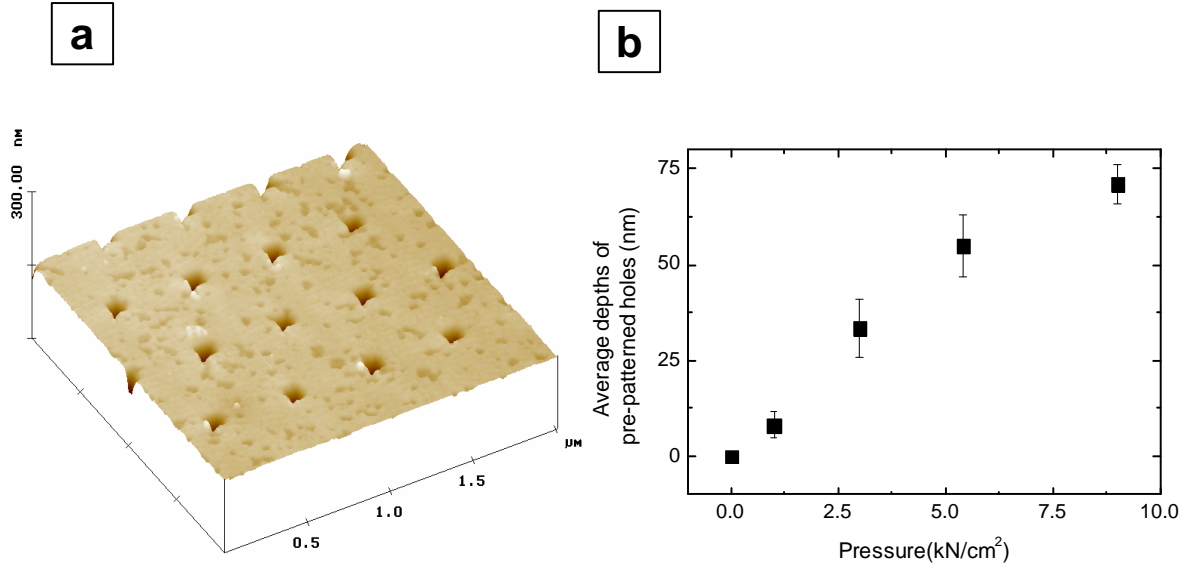


**Figure 3.6:** Pattern transference from the master stamp. a) AFM topography image of Al substrate after stamping, and b) average depths of prepatterns as a function of the applied pressure.

required for stable guiding points is about 50 times lower than that of the dot-like master mold fabricated by Masuda *et al.* [35, 58, 65].

From the AFM analysis, it can be observed that the surface roughness of the pre-patterned area is much lower than that of a just electropolished area. It could effectively lead to a perfect arrangement of pores at the beginning of pore formation [66].

### 3.3.3 Anodization of imprinted aluminum

Keeping in mind that the interpore distance,  $D_{int}$ , of two adjacent pores is determined mainly by the applied potential ( $D_{int} = 2.5 \sim 2.8 \text{ nm/V} \times U$ ), anodization should be carried out around 195 V to obtain a 500 nm interpore distance. The anodization is performed at 195 V since the breakdown potential of alumina was reported at around 200 V when Al is anodized in a weak phosphoric acid [67].

When self-ordering conditions and pre-patterned lattice constant match, very deep pore channels with more than 100  $\mu\text{m}$  can be obtained as shown in Fig. 3.7, which are similar to those obtained by Masuda *et al.* [65].

### 3.3.4 Monodispersity of pore size

The monodispersity of the pore diameter distribution in porous alumina obtained by anodization of the nanoimprinted aluminum is analyzed with an image processing program (NIH image 1.62) and compared with the self-ordered porous alumina structures. The concept of a coefficient of variation of diameter distribution is adopted to assess the monodispersity, which is widely used to evaluate a monodispersity of polymer beads,

$$C.V.value = 100 \times \frac{SD}{AD} \quad (3.1)$$

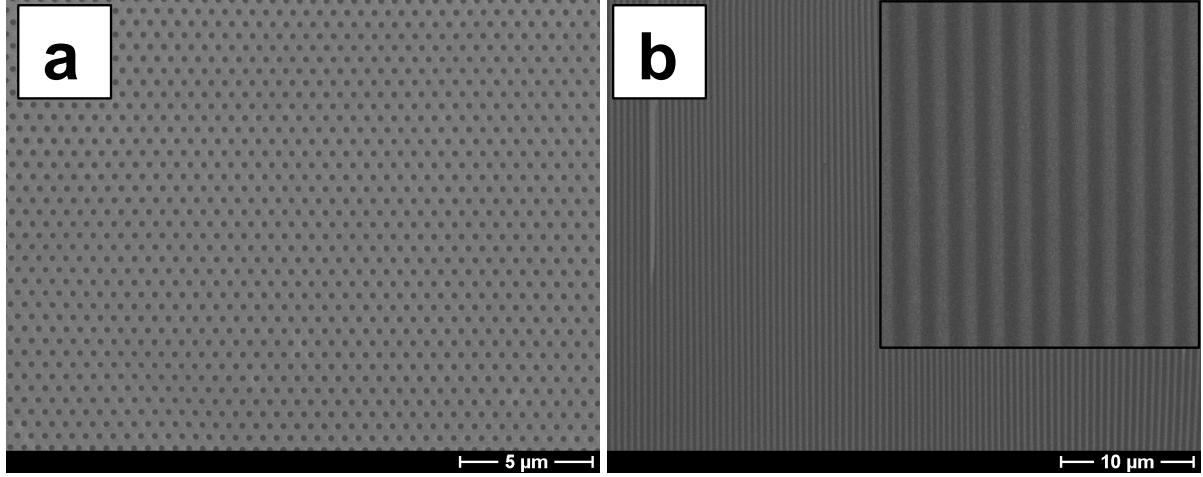


**Figure 3.7:** SEM image of perfectly-ordered porous alumina fabricated by anodization of pre-patterned aluminum (purity: 99.99 %) at 195V in 0.1 M phosphoric acid for 10h : (a) Surface and (b) cross-section of porous alumina. The interpore distance is 500 nm corresponding to the lattice constant of the imprint master. Monodispersity of the channel diameter is highlighted in the inset of Fig. 3.7 (b).

where  $SD$  is standard deviation and  $AD$  is actual diameter. The results show that the monodispersity is highly improved by the nanoimprint-anodization. For a typical example, the analysis indicates 2.1 % for the monodomain porous alumina, 7.8% for the self-ordered porous alumina, and 21% for the disordered porous alumina.

### 3.3.5 Influence of impurities

Si	Fe	Cu	Mn	Mg	Zn	Ti	others each
< 2500	< 4000	< 500	< 500	< 500	< 700	< 500	< 300

**Table 3.1:** Typical concentrations of impurities in 99.5 % Al (ppm) [68].

The influence of impurities of the aluminum substrate on the degree of ordering in monodomain porous alumina is discussed in the following. Anodization of aluminum with a purity of 99.5% (see Table 3.1), which is prestructured in the same way as described previously, is carried out at 195 V in 0.1 M phosphoric acid. Except the purity of Al foil, all preparation procedures are identical as displayed in Fig. 3.7.

Interestingly, defects are even found on the surface in pore arrays (Fig. 3.8 (a)). Defect sites on both surface and bottom as shown in Fig. 3.8 (a) and (b) demonstrate that a high purity aluminum foil is required for the fabrication of defect-free monodomain porous alumina template.

After a long anodization ( $\geq 9$  h), the perfect hexagonal arrangement of pores disappears and disordered porous alumina growth sets in (Fig. 3.8 (c)). In comparison, anodization of the 99.5 % aluminum without prestructuring are also performed in the self-ordering regimes. All results show that there is no self-assembly of pores any more (for example, see Fig. 3.8 (d) and Fig. 3.9).

The effect of the presence of the impurities on the preparation of monodomain or self-ordered porous alumina can be explained by the mobility of metallic foreign atoms. According to Mackintosh *et al.*'s studies [69], species with lower oxidation potentials than Al, e.g., K, Rb, Cs, Ca,

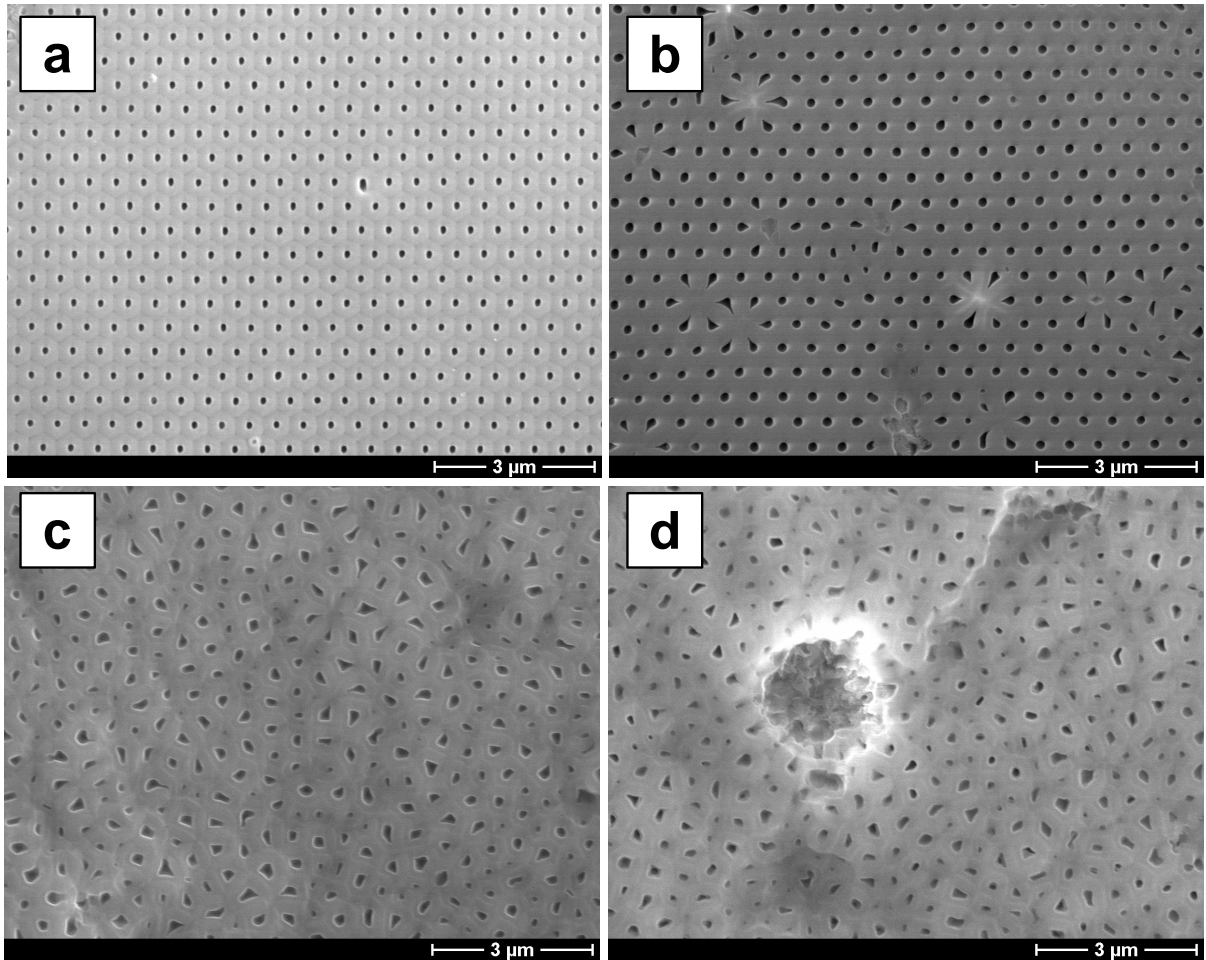


**Figure 3.8:** SEM images of anodized aluminum with a purity of 99.5%. Before anodization, Al is prepatterned by nanoimprint lithography. Except the degree of the purity of the used Al substrate, the anodization conditions are the same as for the sample shown in Fig. 3.7. Anodization of imprinted Al: (a) surface, (b) bottom after 3h anodization, (c) bottom after 9 h anodization. Anodization of Al without nanoindentation: (d) bottom after 9 h anodization in the self-ordering regimes of 195 V.

Sr and Ba, are easily oxidized and incorporated into the alumina oxide (see Table 3.2). Species with higher oxidation potentials than Al are not oxidized and remain in the metallic state. The unoxidized metals may play a role as a barrier hindering further anodization of local sites. This might cause local disordering of pores. As pores grow further, the size of the area of disordered pores increases. Ordered and disordered pore growth compete. Finally, the pore arrangement look as if disordered porous alumina is formed. Fig. 3.9 demonstrates that a large amount of defects with a size of larger than  $1 \mu\text{m}$  stem from the impurities. The pores around the defects are disarranged. However, the self-ordered pore arrays are observed in some local areas (see the enlarged picture in Fig. 3.9)

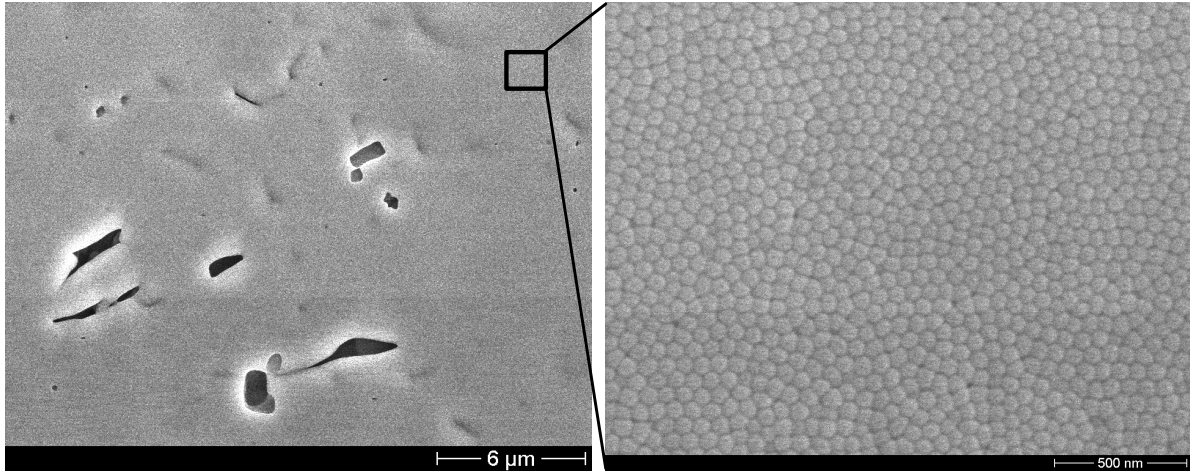


**Figure 3.9:** SEM images of the bottom of porous alumina which is obtained by anodizing 99.5 % Al in 0.3 M sulfuric acid at 25 V for 10 h.

	Reaction	$E^{\circ}/N$
Positive	$\text{Cu}^{2+} + 2e^{-} \longleftrightarrow \text{Cu}$	0.3419
	$\text{Fe}^{3+} + 3e^{-} \longleftrightarrow \text{Fe}$	-0.037
	$\text{Zn}^{2+} + 2e^{-} \longleftrightarrow \text{Zn}$	-0.763
	$\text{SiO} + 2\text{H}^{+} + 2e^{-} \longleftrightarrow \text{Si} + \text{H}_2\text{O}$	-0.8
	$\text{Mn}^{2+} + 2e^{-} \longleftrightarrow \text{Mn}$	-1.185
	$\text{Ti}^{3+} + 3e^{-} \longleftrightarrow \text{Ti}$	-1.37
	$\text{Al}^{3+} + 3e^{-} \longleftrightarrow \text{Al}$	-1.662
Negative	$\text{Mg}^{2+} + 2e^{-} \longleftrightarrow \text{Mg}$	-2.372
	$\text{Ca}^{2+} + 2e^{-} \longleftrightarrow \text{Ca}$	-2.868
	$\text{Sr}^{2+} + 2e^{-} \longleftrightarrow \text{Sr}$	-2.89
	$\text{Ba}^{2+} + 2e^{-} \longleftrightarrow \text{Ba}$	-2.912
	$\text{K}^{+} + e^{-} \longleftrightarrow \text{K}$	-2.931
	$\text{Rb}^{+} + e^{-} \longleftrightarrow \text{Rb}$	-2.98
	$\text{Cs}^{+} + e^{-} \longleftrightarrow \text{Cs}$	-3.026

**Table 3.2:** Electrochemical series of representative foreign metals in Al. Note that species with lower oxidation potentials than Al are easily oxidized (negative) and those with higher oxidation potentials than Al remain in the metallic state (positive) [69, 70].

Note that the impurities which are anodized at a potential lower than Al have different volume expansion coefficients than Al. For example, according to the Pilling-Bedworth ratio (oxide volume produced per unit volume of metal consumed), Mg, which is one of major impurities in

Ce	Al	Pb	Ni	Be	Pd	Cu	Fe	Mn	Co	Cr	Si
1.16	1.28	1.40	1.52	1.59	1.60	1.68	1.77	1.79	1.99	1.99	2.27
K	Li	Na	Mg	Ag	Ti	Ta	Sb	Nb	U	Mo	W
0.45	0.57	0.79	1.21	1.59	1.95	2.33	2.35	2.61	3.05	3.40	3.40

**Table 3.3:** Pilling-Bedworth ratio,  $R$ , of metal oxide indicating the oxide volume produced per unit volume of metal consumed.  $R = \left( \frac{A_0}{\frac{n \times d_0}{d_m} A_m} \right)$ , where  $A_0$  and  $A_m$  are the atomic weights of the oxide and metal, respectively,  $d_0$  and  $d_m$  correspond to the density of each, and  $n$  is the number of metal atoms in a molecular formula of film (example:  $n = 2$  for  $\text{Al}_2\text{O}_3$ ).

the 99.5% Al foil, has small values compared to Al (see Table 3.3)<sup>1</sup>.

### 3.4 Summary

A novel master stamp for nanoindentation of Al was fabricated on 4 inch silicon wafers via modern silicon technology. The master stamp consisted of  $\text{Si}_3\text{N}_4$  pyramids with a 500 nm lattice constant and a height of 260 nm. By applying on optimized pressure (5 kN/cm<sup>2</sup>), the patterns on the master stamp were well transferred onto the electropolished Al, resulting in nanoindented pits with a depth of 50 nm. Subsequent anodization allowed the preparation of monodomain porous alumina with an aspect ratio of  $> 500$ . In addition, effects of impurities on the preparation of monodomain porous alumina were investigated. The results clearly showed that a high purity aluminum is required for the fabrication of a monodomain porous alumina membrane.

<sup>1</sup>volume expansion coefficient ( $\xi$ ) =  $n \times F_w \times$  Pilling-bedworth ratio ( $R$ )

# 4. Porous alumina structures obtained by advanced nanoimprint lithography

Combination of self-assembly of porous alumina (discussed in chapters 1 and 2) and nanoimprint lithography (discussed in chapter 3) allows the preparation of versatile nanostructures which are difficult to prepare with a conventional state-of-the-art lithography. In this chapter, several novel structures fabricated by combining different methods will be discussed.

## 4.1 Smart nanoimprint lithography

In this section, we will discuss that monodomain alumina pore arrays with an interpore distance smaller than the lattice constant of the master stamp can be synthesized if the anodizing conditions, in particular the applied potential, are well adjusted. Here, it will be referred to as smart nanoimprint [71].

### 4.1.1 Experimental

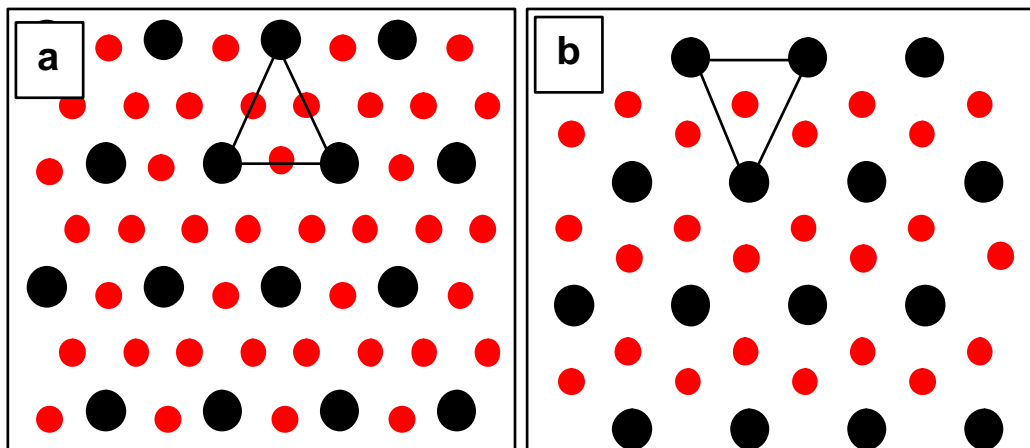


**Figure 4.1:** Schematic diagram of strategies for creating ordered pores in the middle of pre-patterned holes without reduction of the lattice constant of the imprint master. Large circles represent pre-patterned holes with a 500 nm interpore distance, while small circles correspond to new pores resulting from the self-ordering of porous alumina during the anodization: a) two guiding pores to generate new ordered pores in the middle (**Type A**); b) three guiding pores to generate new pores in the center of the three (**Type B**).

It is elucidated how many lithographically defined pores are needed to guide anodization. The basic idea is outlined in Fig. 4.1. The large circles indicate the nanoimprinted pits. The small circles denote the pores created by self-assembly.

First of all, nanoindentation is carried out under the pressure of  $5 \text{ kN/cm}^3$  as discussed in the previous chapter. Subsequently, anodization is performed with two different conditions: A) at  $100 \text{ V}$  ( $0.17 \text{ M}$  phosphoric acid,  $2^\circ\text{C}$ ,  $60 \text{ min}$ ) corresponding to a  $D_{int}/2 = 250 \text{ nm}$  interpore distance (named **Type A**, Fig. 4.1 (a)) to fabricate new periodic pores in the middle of the pre-patterned holes with a  $500 \text{ nm}$  interpore distance, or B) at  $120 \text{ V}$  (same conditions with  $100 \text{ V}$ ) to obtain an interpore distance of  $0.6 \times D_{int} = 300 \text{ nm}$  (named **Type B**, Fig. 4.1 (b)).

## 4.1.2 Results and discussion

### Realization

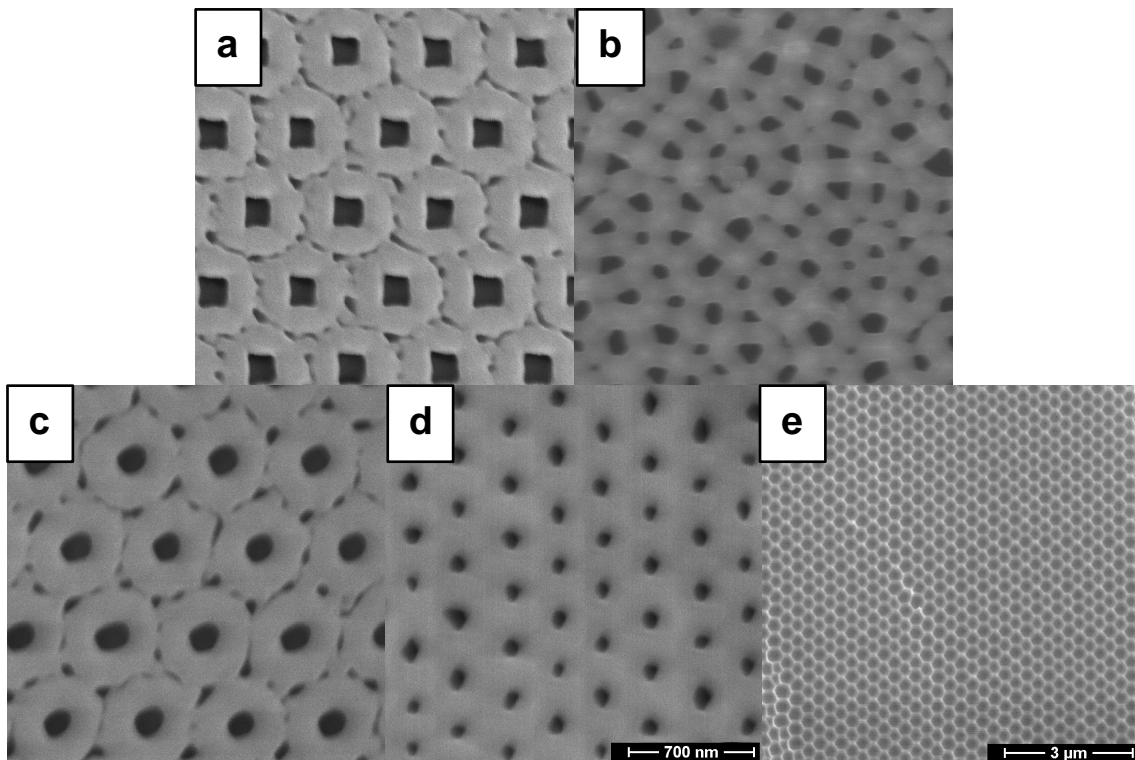


**Figure 4.2:** Realization of the strategies suggested in Fig. 4.1. (a) Top view scanning electron micrograph of pre-patterned alumina anodized at  $2^\circ\text{C}$  at  $100 \text{ V}$  in  $0.17 \text{ M}$  phosphoric acid (**type A**) and (b) bottom view of porous alumina array formed under the conditions for type A. (c) Top view scanning electron micrograph of pre-patterned alumina anodized at  $2^\circ\text{C}$  at  $120 \text{ V}$  in  $0.17 \text{ M}$  phosphoric acid (**type B**). Small (d) and large (e) scale bottom view SEM pictures of the sample of type B exhibiting a perfect hexagonal lattice with  $300 \text{ nm}$  interpore distance. Note that (e) is slightly widened in  $1 \text{ M}$  phosphoric acid for distinguishing view. The scales of (a), (b), (c) and (d) are the same.

The experimental results for  $100 \text{ V}$  and  $120 \text{ V}$  are shown in Fig. 4.2 (a) and (c), respectively. For **type A**, new pores, which do not originate from pre-patterning made by the stamp, initiate irregularly at the boundary of the pre-patterned holes as well as in the middle of two pre-patterned holes (Fig. 4.2 (a)). In contrast, for **type B**, the predicted pores occur in the center of three pores at  $120 \text{ V}$  anodization potential. However, there are some newly-initiated pores on unexpected sites between the three pre-patterned holes. The pores exhibit not all the same size during the initial stages of the anodization. Dissolving selectively the aluminum substrate, the bottom of the pores is investigated (Fig. 4.2 (d)). An ordered  $300 \text{ nm}$  pore array is observed, even on a large scale (Fig. 4.2 (e)). One cannot distinguish anymore between pores originating from

pre-patterning and those developed by self-ordering. Some pores must have vanished or merged during the anodization. Eventually, all the pores tend to be equal in diameter. The coefficient of variation of diameter distribution is 6 % as compared to 2 % for the sample depicted in figure 3.7 (a). The size of the pores resulting from the stamp must have decreased, while that of pores formed newly by the self-ordering must have increased during the anodization. From the above results, it is reasonable to assume that new pores can be guided by three pre-patterned points (**type B**) but not by two pre-patterned points (**type A**). Moreover, we suppose that if there are more than three guiding points on the surface by pre-patterning methods, perfectly self-ordered porous alumina in the center of the guiding points can be obtained without the master stamp having a reduced lattice constant. This method would enable monodomain pore arrays with an interpore distance of 110 nm for a master stamp of 180 nm or even 36 nm for a stamp of 60 nm, which can be produced by e-beam lithography [72].

## Mechanism

The mechanism of smart nanoimprint can be interpreted as shown in Fig. 4.3. When the potential is applied, the electric field lines are focused on the tips of the indented pits. This generates an oxide layer at the tips of the pits (see the checked areas in Fig. 4.3 a). Since the formed oxide acts as an electric insulator, current would flow at the side of the curvatures of the oxide, generating new oxide layers outside the insulator. By the same way, the thickness of the oxide curvatures increases. The oxide curvatures expand until the electric field can expand.

In case of the smart nanoimprint lithography, the expansion of the electric field from the nanoindented pits is not sufficient compared to the distance between the pits. The oxide formed at this stage cannot cover the overlapping point  $M$ . Subsequently, pores by self-assembly start to be randomly formed on the areas where the electric field cannot reach. For example, the areas inside dotted circles in Fig. 4.3 (b) show an electric-field boundary created by the electric field focused on the nanoindented pits.

Fig 4.4 supports the existence of the electric field boundary. For example, there is no random pore formation inside the red circles by self-ordering (see Fig 4.4). Their average diameters increase with increasing applied potential, e.g. around 260 nm for 90 V and 500 nm for 155 V.

This finding is strongly related to the fact that the hexagonal configuration and the hexagonal shape of cell in porous alumina originate from the electric field boundaries which are circularly expanded. For instance, if two pores are created at finite distance so that there is no interaction between them, the cell might have a circular shape. If there are overlapping areas between the two circles, a boundary, which can equally divide the overlapped areas, will be generated (Fig. 4.5). Therefore, the diameter of the circular electric field,  $D_{E-field}$ , is always larger than the cell size,  $D_{cell}$ , in the hexagonal configuration (see Fig. 4.5).

This is simply given by

$$D_{E-field} = D_{cell} / \cos(30^\circ). \quad (4.1)$$

If we consider the approximate relationship between the applied potential and the interpore distance (= cell size) as  $2.5 \sim 2.8 \text{ nm/V}$ , we can obtain an empirical equation for the  $D_{E-field}$  in terms of the applied potential,  $U$ ,

$$D_{E-field}(nm) = 2.89 \sim 3.12(nm/V) \times U(V) \quad (4.2)$$

which is in good agreement with the observation in Fig. 4.4. Fig. 4.6 shows the results of statistic analysis of Fig. 4.4. Actually, the slope of Fig. 4.6 is estimated as 2.89. It can be

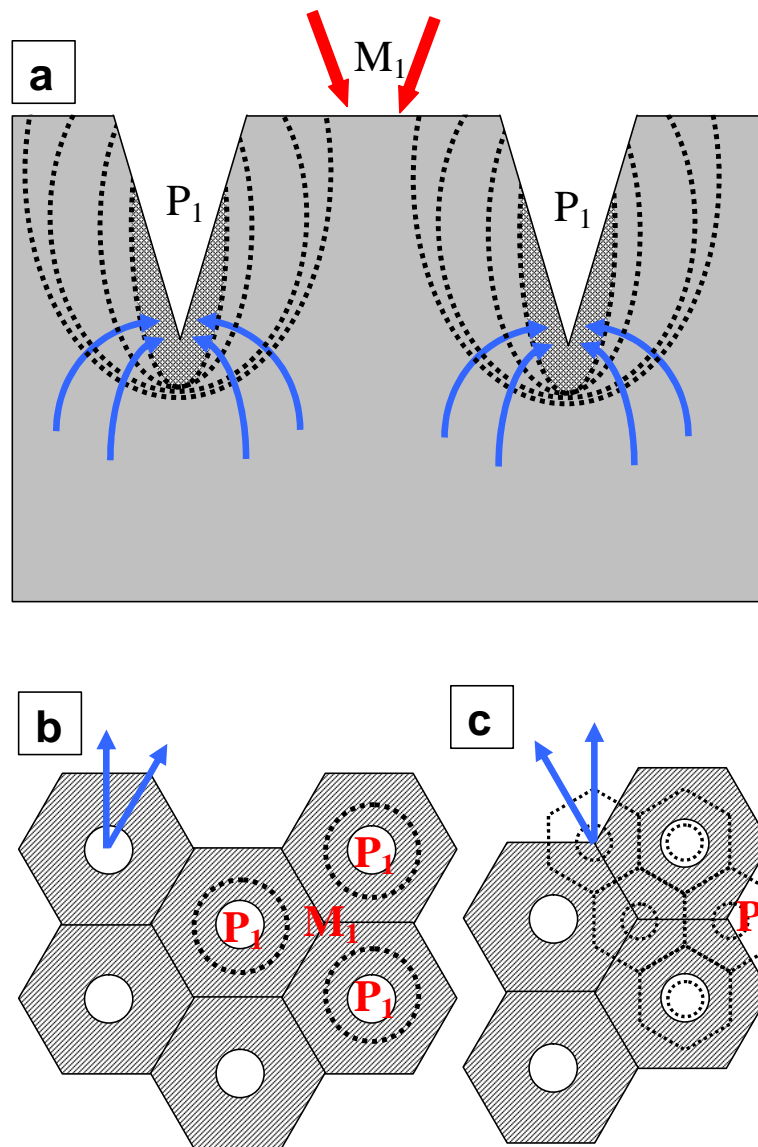


**Figure 4.3:** Mechanism of smart-nanoimprint. (a) Electric field distributions locally focus at nanoimprinted pits ( $P_1$ ) when anodization starts. Since the electric fields lead to the formation of the aluminum oxide with curvatures working as an electric resistor, the current only flows along with the oxide curvatures. This current generates an oxide layer. As a result, the barrier oxide is expanded. The  $M_1$  points indicate the position which is the center from 3 nanoimprinted pits. The oxides caused by the electric field focused at the nanoimprinted pits cannot cover the  $M_1$  points since the electric field is not strong enough in the case of smart-nanoimprint. (b) The dotted circles signify the boundary which the electric fields can reach. There are no random pore formations inside the boundary by the self-ordering. (c) Pores grow stably if the pores initiate by the self-ordering at a suitable position. Note that the direction of the cell is turned by  $30^\circ$ . The arrows shown in Fig. 4.3 (b) and (c) : direction of the cells,  $P_1$ : pores by the nanoimprint,  $P_2$ : pores by smart-nanoimprint, and  $M_1$ : center of three nanoimprinted pits.

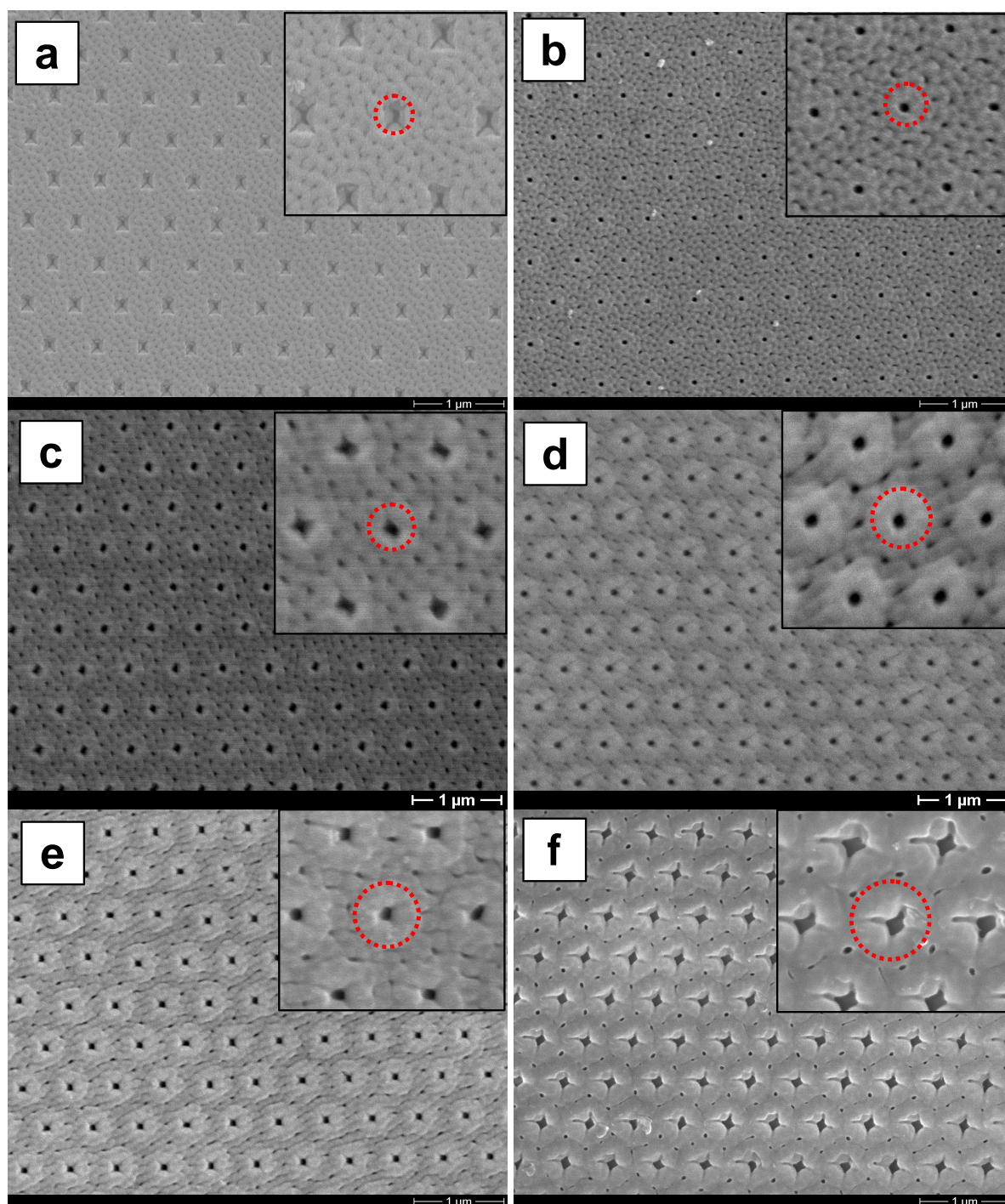


**Figure 4.4:** Formation of protective barrier oxide, which is able to prevent a random creation of pores inside the oxide. This is caused by the electric field focused on the nanoimprinted pits. (a) 40 V (b) 90 V (c) 100 V (d) 116 V (e) 130 V (f) 155 V. Anodization conditions : 0.04 M oxalic acid at 2°C. The red circles in the insets indicate the boundary of the focused electric field.

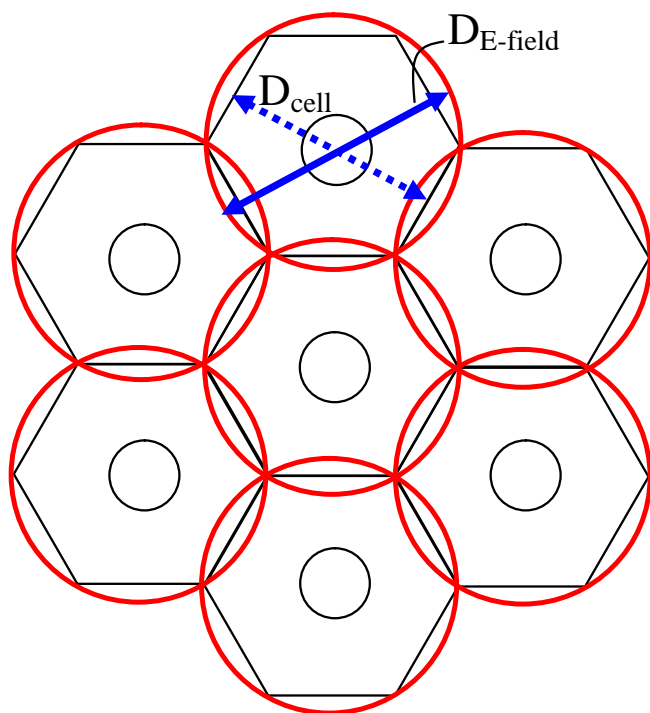


**Figure 4.5:** Schematic diagram of formation of the hexagonal cell configuration and shape which might be caused by the circular electric field. The red circles show the areas influenced by the electric field.

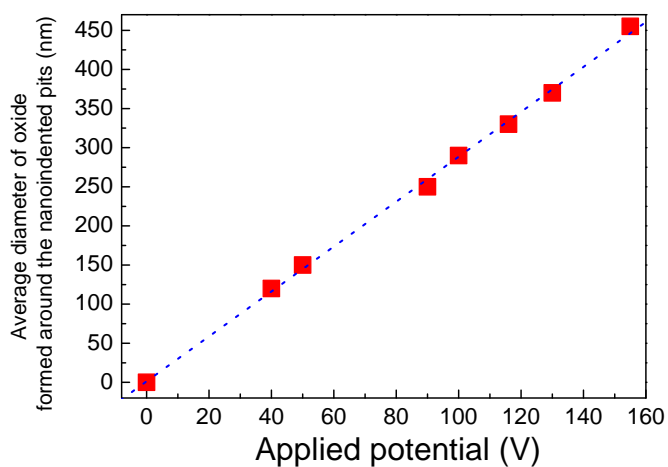


**Figure 4.6:** Average diameter of the protective barrier oxide formed by the circular electric field as a function of the applied potential.

calculated that the boundaries of the electric field touching neighboring boundaries are in the range of  $U = 160 \text{ V} \pm 5 \text{ V}$  (Eq. 4.2). This agrees with the result shown in Fig. 4.4 (f). Note that if the electric field is strong enough, there is no random pore formation in between the nanoindented pits (here, if  $U = 195 \text{ V}$ ).

When we suppose that the oxide boundaries preventing the random creation of pores inside the cells are caused by the concentric electric field at the initial stage, it is reasonable to assume the following: For **type A**, the area in which random pore formation can occur is too broad. Therefore, pores are irregularly created by self-assembly. For **type B**, the area which is not affected by the electric field is restricted to the center of the nanoindented pits ( $M$ ). This enables the guidance of new pore formation (Fig. 4.3 (c)). If the pores are fully developed in the center of the three pits by smart-nanoimprint, the cell orientation would be turned by  $30^\circ$  relative to the original orientation (see the arrows in Fig. 4.3 (b) and (c)).

### Pore shapes

Another important aspect is the change of the pore shape during anodization. The shape of the pores on the surface depends strongly on the shape of the master mold. For example, a rectangular shape of the pores on the surface can be obtained by applying high-pressures during stamping, whereas more or less circular shapes of the pores can be generated by applying low-pressures. However, the shape of the pores at the bottom is not affected by the shape of pre-patterned holes on the surface, but by the current flow and the electrolyte. By comparing surface and bottom view, one can observe that the shape of pores is changed from rectangles into circles during the growth of pores.

### Effects of the flatness of the substrate surface

One can expect that the interpore distance of the pore array can be further reduced to 36 % ( $60\% \times 60\%$ ) of the lattice constant of the master stamp if a 2-step process is adopted. For example, after a first reduction of the interpore distance by 60 % by smart-nanoimprint (at 120 V), the first-formed oxide is removed, followed by anodization at around 72 V. However, this strategy does not work since there are preferred positions for the generation of pores in the scalloped patterns as shown in Fig 4.7. For instance,  $M_2$  would be the ideal position for further reduction. However, the pores are created on the shoulder of the scallops during the second anodization ( $P_3$ ). This underlines importance of surface flatness for smart nanoimprint.

## 4.2 Monodomain porous alumina with branched structures

Hierarchically arranged nanostructures in porous alumina obtained by stepwise reducing the applied potential are discussed in this section [10, 73, 74]. The obtained structures consist of monodomain porous alumina with 500 nm interpore distance on one side and self-ordered porous alumina with either 100 nm or 65 nm interpore distance on the other side. Furthermore, self-ordered structures (500 nm or 100 nm) connected self-ordered structures (100 nm or 65 nm) will be discussed. They can be used as templates for monodisperse silver nanowires with several branches (see Chapter 6).

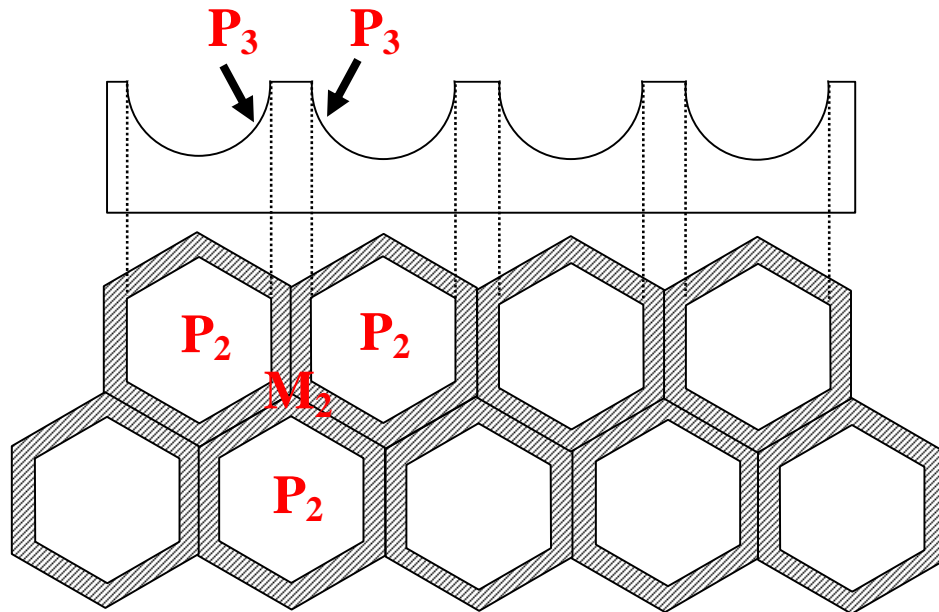


**Figure 4.7:** Suggestion for a strategy to further reduce the interpore distance to 36 % of the lattice constant of the master stamp by a 2-step smart nanoimprint (nanoimprint  $\rightarrow$  anodization at 120 V  $\rightarrow$  removing the oxide  $\rightarrow$  anodization at 72 V) procedure. The strategy does not work due to the surface roughness of the substrate after the first anodization.  $P_2$ : pores formed by anodization at 120 V,  $M_2$ : the ideal center of  $P_2$ , and  $P_3$ : real pores formed by anodization at 72 V.

#### 4.2.1 Experimental

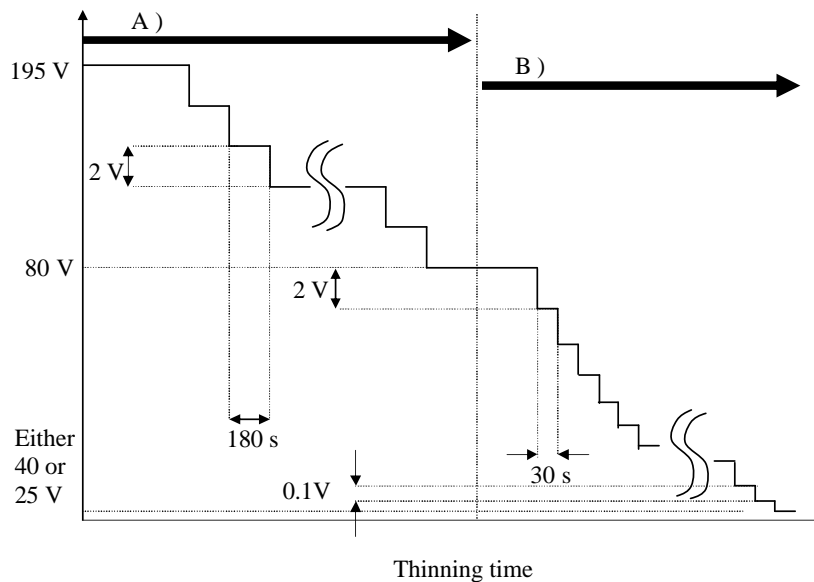


**Figure 4.8:** Sketch of the thinning process: in part (A), a stepwise reduction of potential in steps of 2 V is applied for 180 s in 0.1 M phosphoric acid during each step until 80 V. (B) Stepwise potential reductions with exponentially decaying difference is applied for 30 s in 0.3 M oxalic acid.

After the fabrication of monodomain porous alumina (Fig. 3.7), thinning of the barrier layer is performed. In each thinning step, a stepwise potential of 2 V lower than the previous potential is applied. For homogenous thinning, two subsequent thinning processes as shown in Fig 4.8 are

used; In process **A**, from 195 V down to 80 V, a stepwise potential is applied in 0.1 M phosphoric acid with a step duration of 180 s. In process **B**, from 80 V down to the potential allowing the preparation of self-ordered structures (either 40 V or 25 V), exponentially decaying potential<sup>1</sup> is applied in 0.3 M oxalic acid for 30 s in each step. After the thinning process, the structure with a barrier layer thickness of either around 55 nm ( $40 \text{ V} \times 1.2 \sim 1.6 \text{ nm/V}$ ) or 35 nm ( $25 \text{ V} \times 1.2 \sim 1.6 \text{ nm/V}$ ) is consequently anodized in the appropriate self-ordering regimes, i.e., either in 0.3 M oxalic acid at 40 V or in 0.3 M sulfuric acid at 25 V, respectively. This process allows the preparation of self-ordered branched structures on the bottom of the monodomain porous alumina. In a similar manner, a self-ordered porous alumina structure with 100 nm interpore distance is connected to a self-ordered porous alumina structure with 65 nm interpore distance.

## 4.2.2 Results and discussion

### Monodomain porous alumina with a 500 nm interpore distance connected to polydomain porous alumina with 65 nm interpore distance

A schematic diagram of the transition from monodomain porous alumina to the self-ordered branches is depicted in Fig. 4.9. During the anodization in phosphoric acid at 195 V, a monodomain porous alumina structure with an interpore distance of 500 nm is formed (**A** in Fig. 4.9). Afterward, dendrites with 3-5 branches originating from each pore start to grow during the thinning process (**B** in Fig. 4.9). The thickness of this dendrite layer is about  $5 \mu\text{m}$  and it is mainly determined by the parameters chosen for the thinning process. Subsequently, a second anodization under conditions obeying the 10% porosity rule yields poly-domain porous alumina structures (**C** in Fig. 4.9). For example, Fig. 4.10 (a) shows a perfectly arranged monodomain porous alumina with 500 nm interpore distance and 180 nm pore diameter formed during the first anodization. On the bottom of the structure, well-ordered polydomain porous alumina with 65 nm interpore distance and 25 nm pore diameter is formed during the thinning process and the second anodization (see Fig. 4.10 (b)), corresponding to C of Fig. 4.9.

In fact, the porous alumina shows periodically arranged channels with  $D_{int} = 500 \text{ nm}$  (monodomain region), dendrite channels (buffer region) and self-ordered channels with  $D_{int} = 65 \text{ nm}$  (polydomain region). Fig. 4.10 (c) depicts a cross-sectional view of the structures.

### Monodomain porous alumina with a 500 nm interpore distance connected to polydomain porous alumina with 100 nm interpore distance

A self-ordered branched structure with an interpore distance of 100 nm beneath the monodomain porous alumina is obtained in a similar manner as the 65 nm periodic structure (Fig. 4.10 (d)). It is important to note that any kind of highly-arranged branched structures can be obtained underneath the monodomain pore array, if the branched structure is formed under the self-ordering conditions. The domain size of the porous alumina formed during the subsequent anodization is comparable to that of porous alumina formed by the conventional 2-step anodization, even though squeezed pores are observed (Fig. 4.10 (d)). The squeezed pores indicate that the mechanical stress between pores does not reach the optimized value yet (see the Section 1.5.3). Note that self-ordered porous alumina is only obtained when the volume expansion

<sup>1</sup>Note that the potential differences in the last several steps are a few milli-voltages, whereas that in the initial step is 2 V.

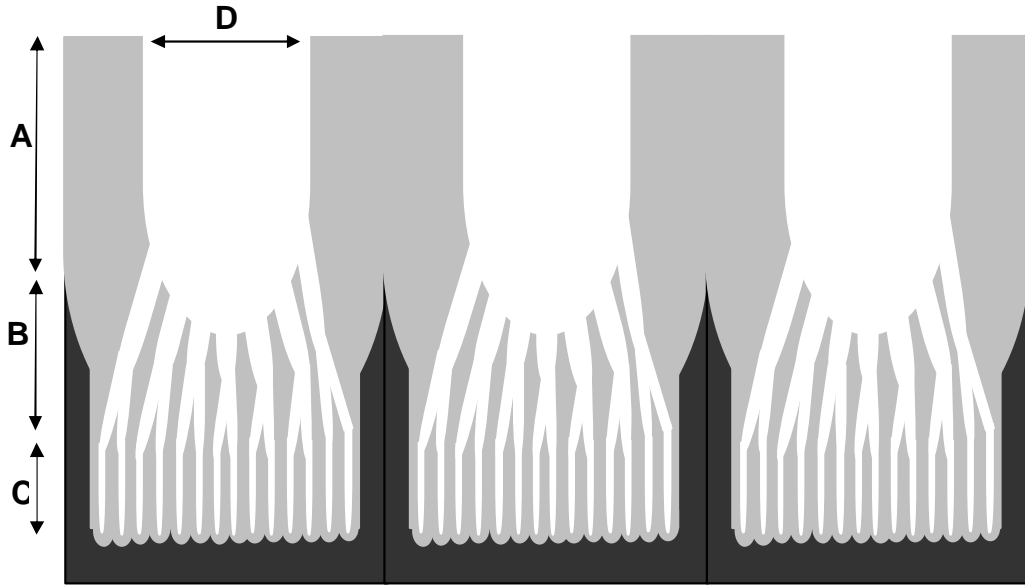


**Figure 4.9:** A schematic diagram of the cross-sectional view of monodomain porous channels with self-ordered branches. A: pores formed by anodization of indented aluminum at 195V (the length is adjustable depending on anodization time. Here, 100  $\mu\text{m}$ ), B: diverging branches created by the thinning process from 195 V down to a self-ordering potential and C: pores created by self-ordering anodization at either 25 V or 40 V.

caused by the stress equals to  $\xi = 1.2$ . However, it is expected that more perfectly arranged pore arrays can be obtained if the anodization time is increased.

### Cell conformation and mismatch

Fig. 4.11 (a) and (b) show conformation and mismatch between the different cell sizes, respectively. The cell with a size of 500 nm whose pores are formed by anodization of nanoimprinted Al does not contain exactly cells with a size of 65 nm. (Note that 500 nm cannot be divided by 65 nm into an integer, see Fig. 4.11 (b)). However, in the case of the combination of 500 nm-and-100 nm (Fig. 4.11 (a)), the total size of 25 unit cells with 100 nm size, which are formed at the second anodization of 40 V, exactly corresponds to that of one unit cell with the 500 nm cell size.

This result demonstrate that the porous alumina consequently formed in the self-ordering regimes can be self-assembled on the bottom of the monodomain layer, not depending on whether the cell sizes between the monodomain and the polydomain layers match or not.

This could be explained as follows: first, during the course of the thinning, the dendritic branches grow with some tendency of self-arrangement, keeping mainly the predetermined position of the pores formed during the first anodization. Therefore, the subsequent second anodization does not lead to a totally disordered structure but to polydomain arrays. Secondly, the mismatch between the two interpore distances is compensated by disordered areas at the domain boundaries of the polydomains.

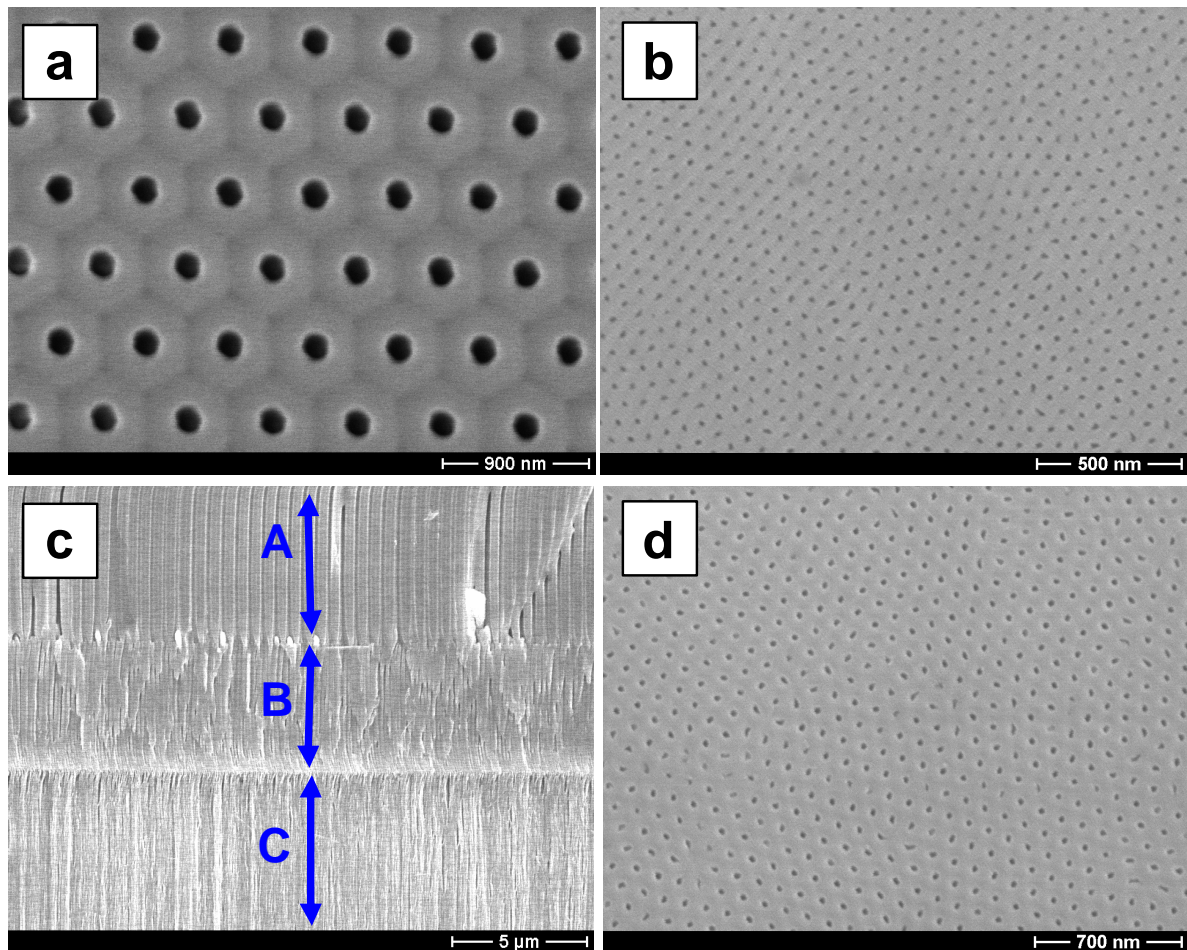


**Figure 4.10:** SEM images of monodomain porous alumina formed at 195 V connected to the polydomain porous alumina formed at 25 V (a, b, c) and at 40 V (d): a) 500 nm periodic monodomain porous alumina (top view), b) 65 nm periodic polydomain porous alumina (bottom view), c) Side view of this structure. The upper layer (**A**) corresponds to the **A** layer in Fig. 4.9, the middle layer (**B**) is formed during the thinning process and the bottom layer (**C**) corresponds to **B** in Fig. 4.9, and d) 100 nm periodic polydomain porous alumina (bottom view).

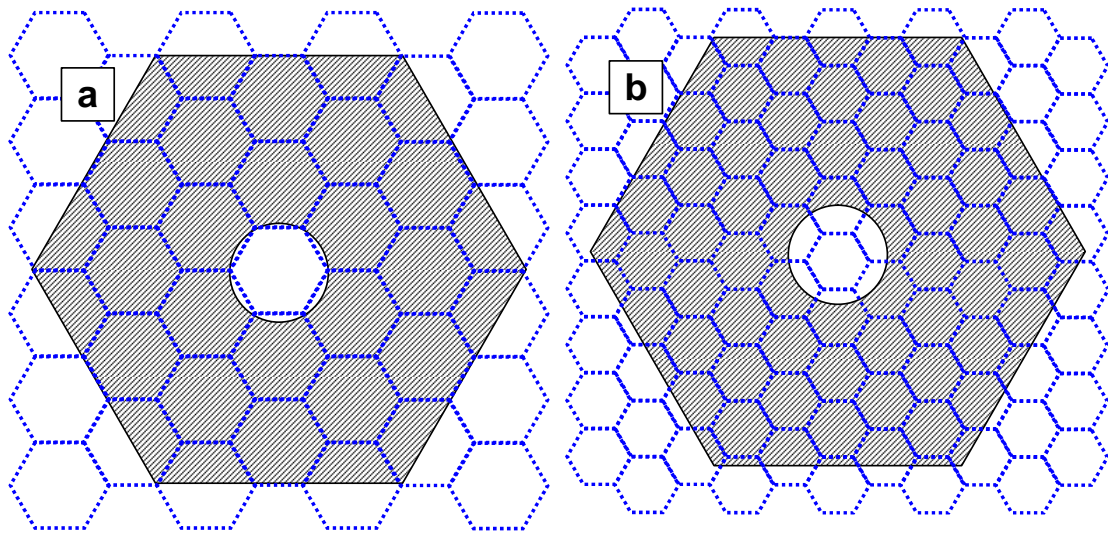


**Figure 4.11:** Mismatch between cells with a size of 500 nm and a size of (a) 100 nm and (b) 65 nm. Solid lines indicate the 500 nm cell. The blue-dotted lines in Fig. 4.11 (a) and (b) indicate the 100 nm and 65 nm cells, respectively.

### **Influence of pore diameter on the arrangement of branches**

Another interesting fact is that the degree of self-arrangement of the pores is hardly influenced by the diameter of the pores formed in phosphoric acid (**D** in Fig. 4.9, result is not shown here), but it is more influenced by the thinning process. For example, pores with 180 nm (the original diameter) and with 300 nm (widened diameter) in the monodomain layer lead to almost the same degree of pore ordering in the underlying self-ordered layer.

### **Polydomain porous alumina with a 100 nm interpore distance connected to polydomain porous alumina with 65 nm interpore distance**

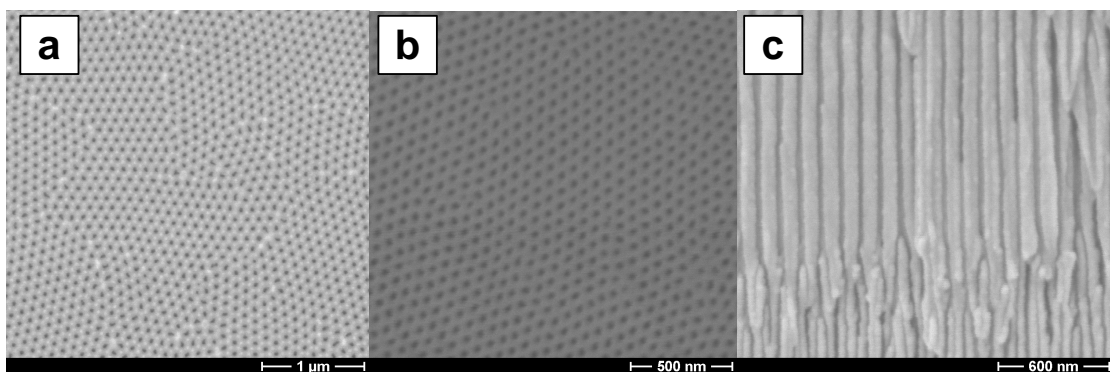


**Figure 4.12:** SEM images of polydomain alumina formed at 40 V connected to polydomain porous alumina formed at 25 V for 10 h: a) top view (40 V region), b) bottom of opened pores (25 V region), and c) side view. Note that the figures are at different scale.

A self-ordered structure having 100 nm interpore distance can also be connected to self-ordered structures having 65 nm interpore distance. In Figs. 4.12 (a) and (b), one can see that both the 100 nm and the 65 nm periodic structures exhibit a good hexagonal arrangement of the pores.

In a cross-sectional view (Fig. 4.12 (c)), a dendritic transition can be found. The results show that two types of porous alumina channels with polydomain arrays can be connected to each other by a simple thinning process.

### Pore arrangement by a stepwise increase of potential

The question arises what happens if the applied potential is stepwise increased from the self-ordering regimes of either 25 V or 40 V to the self-ordering regimes of either 40 V or 195 V.

For example, Al is anodized with a stepwise increase of the potential from 40 V to 195 V which is exactly the opposite way of the previously described stepwise reduction of the applied potential. After reaching the final potential, the sample is further anodized at 195 V for 5 h. In Fig. 4.13, one can observe that the arrangement of pores is very comparable to those formed via the 2-step anodization with the 195 V-self-ordering conditions.

Investigation of the interface layer, which is formed during the stepwise increase of the potential, reveals that the pores, which have not survived, have rather vanished than merged (see the inset in Fig. 4.13).

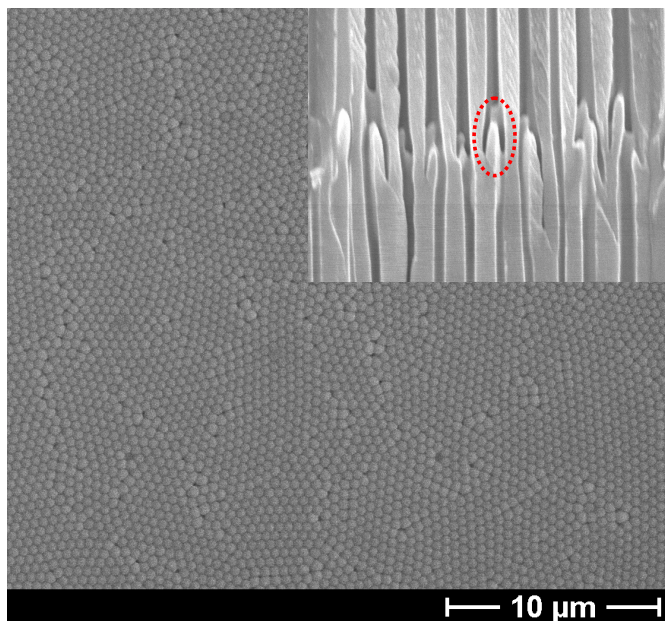


**Figure 4.13:** SEM images of the bottom of a porous alumina template, which is formed by stepwise increase of the potential from 40 V to 195 V, followed by anodization in 0.1 M phosphoric acid at 195 V for 5 h. The inset shows the interface layer which is formed during the stepwise potential increase.

These results demonstrate that self-ordered pores can be connected to self-ordered branches not only by the stepwise reductions but also by the stepwise increase of the potential if the anodization is carried out in the self-ordering regimes.

## 4.3 Monodomain porous alumina on Si

Nowadays, most real devices are fabricated based on modern silicon technologies. Several attempts to integrate alumina templates with modern silicon technologies are progressing [64, 75, 76, 77, 78, 79, 80]. It has turned out that the fabrication of self-ordered porous alumina on silicon by the conventional two-step methods is not possible because the thickness of the evaporated aluminum is limited. Anodization of nanoimprinted aluminum is a promising method

to obtain perfectly ordered porous alumina on silicon. Here, the fabrication of monodomain porous alumina on a silicon wafer is discussed.

### 4.3.1 Experimental

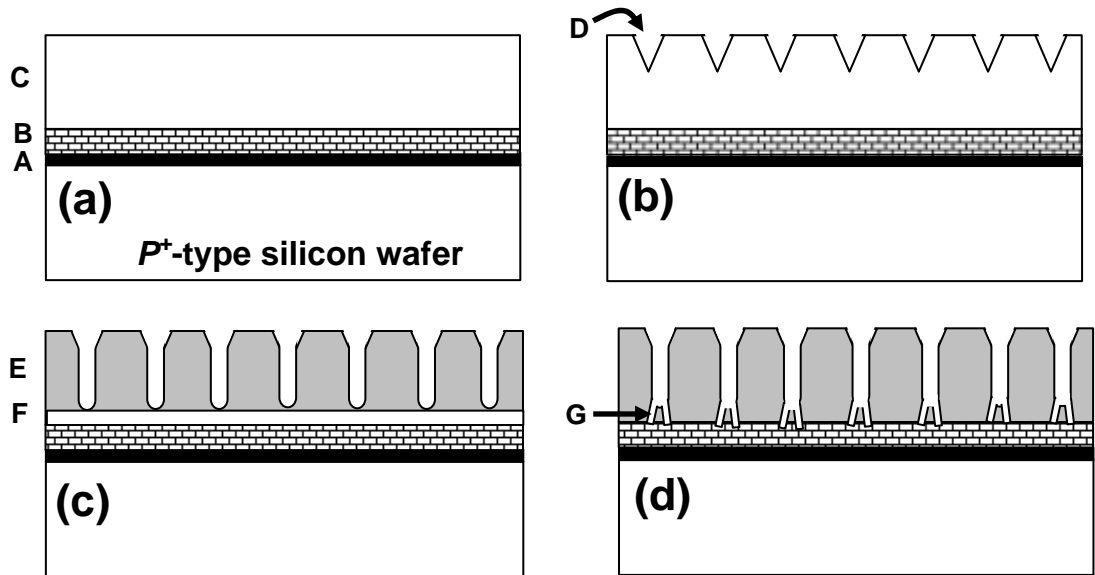


**Figure 4.14:** Schematic diagram of the preparation of monodomain porous alumina on silicon: (a) Al layer evaporated on Si substrate, (b) Prepattern transfer into the Al layer by nanoindentation under  $5 \text{ kN/cm}^2$  pressure, (c) Porous alumina growth by electrochemical anodization, (d) Thinning process, which allows the pores to homogenously contact the Pt layer. A: Ti layer with 5 nm thickness, B: Pt layer with 50 nm thickness, C: Al layer with 2000 nm thickness, D: Prepattern formed by nanoindentation using a master stamp, E: Porous alumina film converted from the Al film by electrochemical anodization, F: Remaining Al layer after the anodization, and G: Dendrite formation during a thinning process.

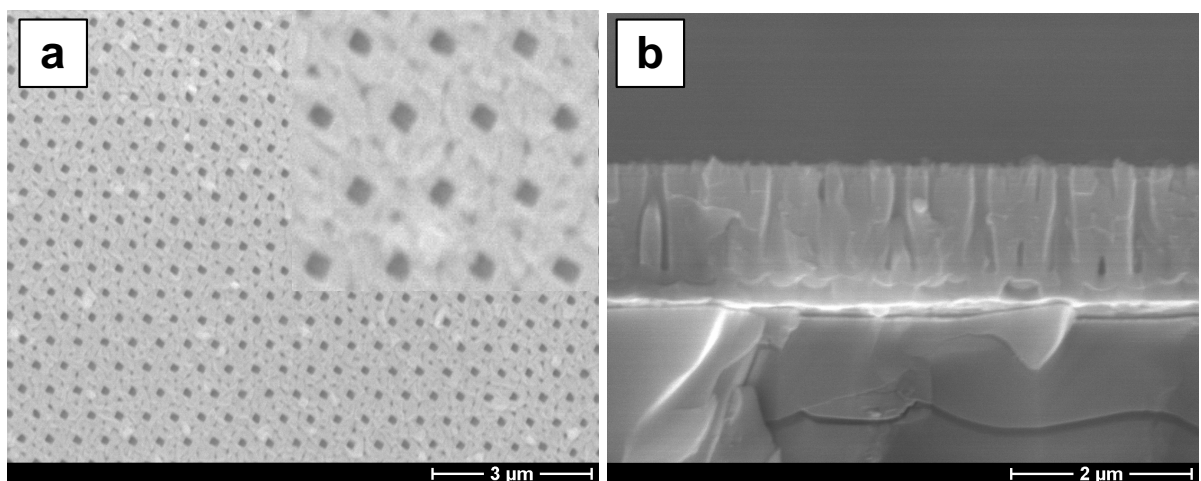


**Figure 4.15:** SEM images of an Al film on Si anodized under constant current density ( $4 \text{ mA/cm}^2$ ) in 1 M phosphoric acid (anodizing condition A): (a) top view and (b) cross-section view. Pores with rectangular features are clearly shown at high magnification (inset).

First, a Ti diffusion barrier layer with 5 nm thickness is evaporated on a 4 inch silicon wafer ( $\langle 111 \rangle$ ,  $p^+$ -type,  $0.01 \Omega\text{cm}$ ). It improves the adhesion of the subsequent Pt layer with 50 nm

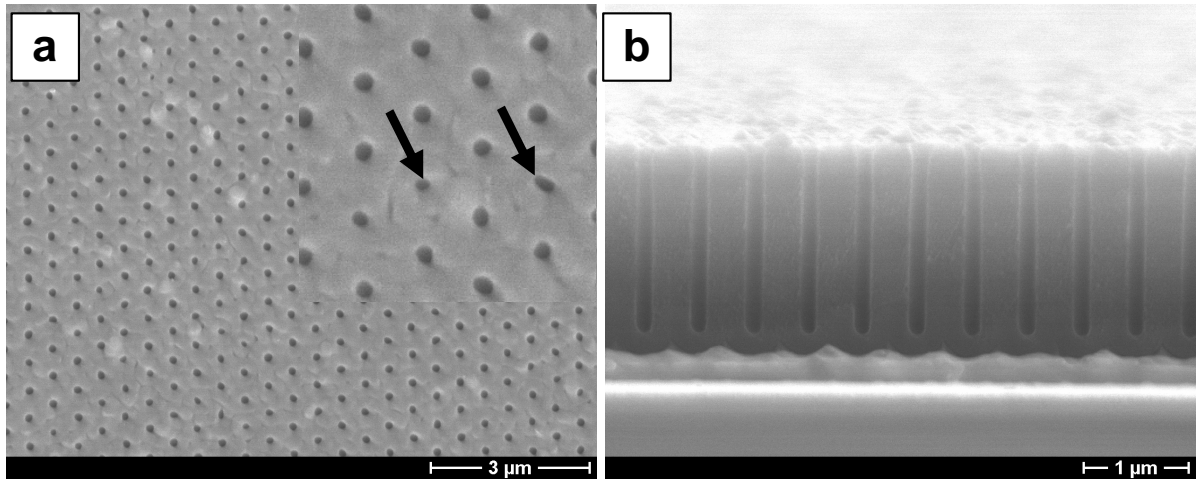


**Figure 4.16:** SEM micrographs of an Al film on Si anodized under constant potential (195 V) in 0.05 M phosphoric acid (anodizing condition **B**): (a) top view and (b) cross-section view. The arrows in the inset indicate defect sites having different sizes or features.

thickness. Then, an aluminum layer with about 2000 nm thickness is thermally evaporated as shown in Fig. 4.14 . The roughness of the surface of the Al layer is less than 200 nm for a piece of wafer with a size of  $1 \times 1 \text{ cm}^2$ . Subsequently, a piece of stamp with the size of  $1 \times 1 \text{ cm}^2$  is placed on the Al on Si substrate. The pattern of the master stamp is transferred onto the Al under  $5 \text{ kN/cm}^2$  with the oil press. This value is equivalent to the pressure for nanoindentation of bulk Al (see Fig. 3.6).

Due to the limited thickness of the evaporated Al film, the electropolishing process which is usually carried out before the anodization of bulk aluminum metal is omitted. Subsequently, the imprinted Al film is anodized under two different conditions: **A**) with a constant current density of  $4 \text{ mA/cm}^2$  in 1 M phosphoric acid; or **B**) with a constant potential of 195 V in 0.05 M phosphoric acid. These conditions differ from those required for monodomain porous alumina with 500 nm interpore distance with a very high aspect ratio (195 V, 0.1 M phosphoric acid). The conventional conditions very often lead to local heating, causing a dielectric breakdown of the oxide during anodizing. The modified conditions allow to circumvent this problem during the anodization of the thin Al film (Fig. 4.14 (c)).

### 4.3.2 Results and discussion

Fig. 4.15 shows SEM images of porous alumina arrays formed under **condition A**. Hexagonally arranged porous alumina with a lattice constant of  $D_{int} = 500 \text{ nm}$  and rectangular pore features can be seen in the top view image. The rectangular pore features are replicas of the pattern of the master stamp, indicating that the repulsive force between neighboring pores during the anodizing is very weak. This is in good agreement with the course of the potential during the anodization. The potential increases up to 150 V and then it very slowly decreases. Finally, it reaches a stable value at around 145 V. Since the volume expansion which is needed to form circular pores with a 500 nm interpore distance can be created at 195 V, the rectangular pores can be explained as the result of weak repulsive forces. If the repulsive force is sufficiently high, the dissolution at the corners of the rectangular pores will be enhanced so that the pore shape changes to circular. However, regardless of the repulsive force, the pores start to grow preferentially from the prepatterned holes. The cross-section image shows that the pores grow

up to 500 nm guided by the prepatterned holes (Fig. 4.15). For larger thickness than 500 nm, the pores split into two or three branches. This structure is similar to the dendrite structures formed by the constant current limit method [10].

Perfect monodomain porous alumina is obtained under **condition B** (Fig. 4.16). Even though defects and a relatively large size distribution of pores are observed compared to the monodomain porous alumina formed on bulk aluminum, straight and monodisperse pore channels can be obtained as illustrated in the cross-sectional view as shown in Fig. 4.16(b). Since the imprinted patterns in the aluminum are inverse pyramids, the pores in the mouth are larger than in the body. During the anodization under potentiostatic condition, the current is constant. Then, it increases abruptly, indicating that the first pores arrive at the Pt layer [76, 77, 78]. The results show that perfectly ordered porous alumina on Si with variable aspect ratios (pore length / pore diameter) up to  $\sim 10$  can be obtained under slightly modified conditions, while porous alumina with an extremely high aspect ratio, e.g.  $\sim 500$ , can only be prepared under the conditions obeying the 10 % porosity rule [41].

## 4.4 Superposition of successive nanoimprint patterns

It is well known from classical optics that superposition of two regular patterns, e.g., parallel lines, concentric circles, hexagonal dots, produce Moiré patterns which are never observed in single element patterns [81, 82, 83]. Artificial synthesis of porous arrays with Moiré patterns is very difficult to achieve with current state-of-the-art conventional lithography since the demanding lattice spacing is complicated [84]. In this section, fabrication of porous alumina arrays with Moiré patterns by means of nanoimprint lithography is introduced. In addition, it is demonstrated that a polymer replica of the patterns can be obtained by spin-coating.

### 4.4.1 Experimental

Fig. 4.17 shows a schematic diagram of the preparation procedure for porous alumina arrays with Moiré patterns. The pattern of the master stamp is transferred on the Al under  $5 \text{ kN/cm}^2$  (see the Section 3.3.2). As a result, inverse-pyramidal concaves consisting of a square of  $70 \times 70 \text{ nm}$  and a depth of  $50 \text{ nm}$  are formed on the Al. To generate a complex pattern, nanoindentation has to be conducted twice (Figs. 4.17 A and B). The pressures should be identical in the course of two-step nanoindentation. Different Moiré patterns can be created by changing the rotation angle. After two times nanoindentation, anodization is carried out with constant current density ( $2 \text{ mA/cm}^2$ ,  $1 \text{ M H}_3\text{PO}_4$ ,  $3 \text{ }^\circ\text{C}$ ) for several minutes in order to obtain pore channels with the Moiré patterns (Fig. 4.17 C). Subsequently, a photoresist (ARP-351, Allresist GmbH) is spun on the porous arrays with the Moiré patterns (6000 rpm, 30 s, baking temp. =  $90^\circ$ ) (Fig. 4.17 D). To allow handling of the polymer film, a piece of silicon wafer is bonded on top of the resist (Fig. 4.17 E)). Since alumina can be selectively dissolved in a chromic acid containing solution without destroying the polymer film, a nanostructured polymer film with the transferred pattern is obtained on Si (Fig. 4.17 F).

### 4.4.2 Theoretical description

From the theory of Moiré patterns published by Oster *et al.* [81], the theory of the superposition of two hexagonal patterns is deduced. Here, the periodicity in Moiré pattern,  $D_{moi}$ , is described

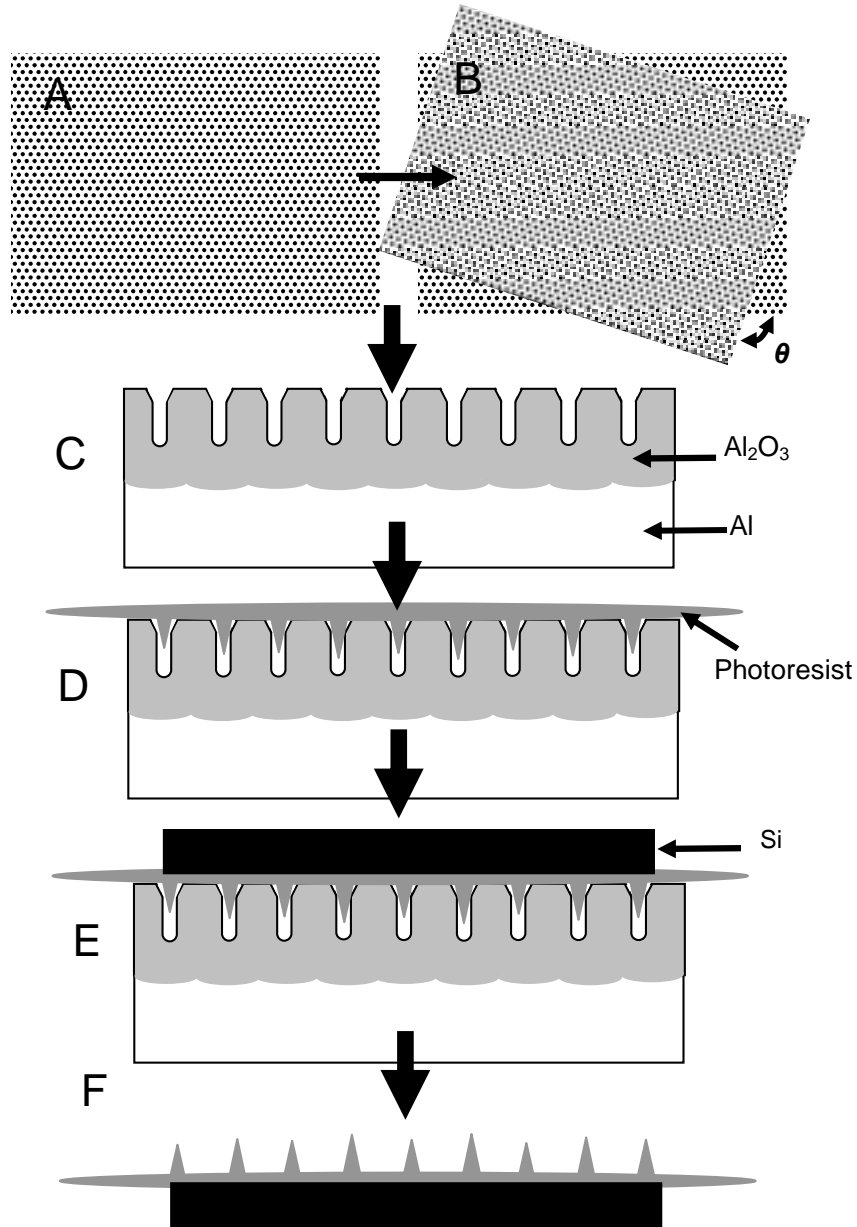


**Figure 4.17:** Fabrication procedures of polymer replicas with Moiré pattern on Si. A: First nanoindentation, B: Second nanoindentation with a rotation angle  $\theta$ , C: Anodization with constant current density ( $2 \text{ mA/cm}^2$ ) in 1 M phosphoric acid for several minutes ( $1 \sim 60 \text{ min}$ ) at  $3 \text{ }^\circ\text{C}$ , D: Spin coating with photoresist (6000 rpm for 30 s, baking temperature =  $90^\circ$ ), E: Bonding a silicon substrate with the photoresist by epoxy resin, and F: Selective removal of the aluminum oxide in a chromic acid containing solution.

as

$$D_{moi} = ab/\sqrt{(a^2 + b^2 - 2 a b \cos(\theta))} \quad (4.3)$$

where  $a$  and  $b$  are the lattice constants of the first pattern and of the second pattern, respectively, and  $\theta$  is the rotation angle between the two nanoindentation. Since  $a$  and  $b$  are identical ( $= D_{int} = 500$  nm) in our case, the equation is simply given by

$$D_{moi} = a/\sqrt{(2 - 2 \cos(\theta))} \quad (4.4)$$

which can be further simplified to

$$D_{moi} = a/[2 \times \sin(\theta/2)] \quad (4.5)$$

The equations 4.4 and 4.5 are only valid when  $0 < \theta \leq 30^\circ$  since both the element patterns are hexagonal. If the angular periodicity in the hexagonal pattern is considered, the following boundary condition is found;

$$\begin{aligned} \theta - 60^\circ \times n \text{ when } 60^\circ \times n < \theta \leq 60^\circ \times (n + 0.5) \\ 60^\circ \times (n + 1) - \theta \text{ when } 60^\circ \times (n + 0.5) \leq \theta < 60^\circ \times (n + 1) \end{aligned}$$

where  $n = 0, 1, 2 \dots$ . For example, for the rotation angle  $\theta = 3^\circ, 57^\circ, 63^\circ \dots$ , the distance between fringes is  $D_{moi} = 9.55 \mu\text{m}$ . In addition, if the rotation angle is equal to multiples of  $60^\circ$ , for example  $\theta = 0^\circ, 60^\circ, 120^\circ, 180^\circ \dots$ , the overlapping two patterns have no angular difference. As a result, the single element pattern can be created from the superimposed patterns if the second nanoimprint position is chosen properly relative to the first nanoimprint position.

### 4.4.3 Results and discussion

As predicted by Eq. 4.5, the smaller the rotation angle, the larger is the periodicity of the formed Moiré pattern. For example, Figs. 4.18 (a) (b) and (c) show porous alumina arrays with Moiré patterns, formed by anodization of aluminum nanoindented with a rotation angle of  $2.2^\circ, 11.5^\circ$ , and  $30^\circ$ , respectively. From the equation 4.4 or 4.5, the Moiré pattern periodicities of Figs. 4.18 (a), (b) and (c) are calculated as 13, 2.5 and  $0.97 \mu\text{m}$ , respectively. These are in good agreement with the real measurement of the periodicity. Fourier transform (FT) analyzes of the Figs. 4.18 (a) to (c) by an imaging processing method demonstrate homogenous periodic patterns over an large area (see the inset in each picture). The superstructures with a six-fold symmetry can be clearly seen from the FTs in Figs. 4.18 (a) and (b). For Fig. 4.18 (c), a 12-fold symmetry can be observed since  $D_{moi} \sim 2 D_{int}$ .

Since the interpore distance  $D_{int}$  of the pores is linearly proportional to the applied potential ( $U$ ) (see Eq. 1.9) [18], potentiostatic methods are not able to generate pore arrays with different interpore distances as shown in Fig. 4.18. If the electrolyte is too diluted, the ohmic resistivity in the electrolyte becomes significant so that a galvanostatic mode can easily switch to a potentiostatic mode. This is the reason why anodization is carried out with constant current density in a concentrated electrolyte to form such porous arrays. It was already demonstrated that straight pore channels with around 500 nm thickness can be fabricated not only with constant potential but also with constant current density, if Al is nanoindented prior to the anodization (see Section 4.3) [79].

Since the anodization is performed under conditions deviating from the self-ordering regimes, the pore arrangement at the bottom is expected to be disordered if the anodizing time is too

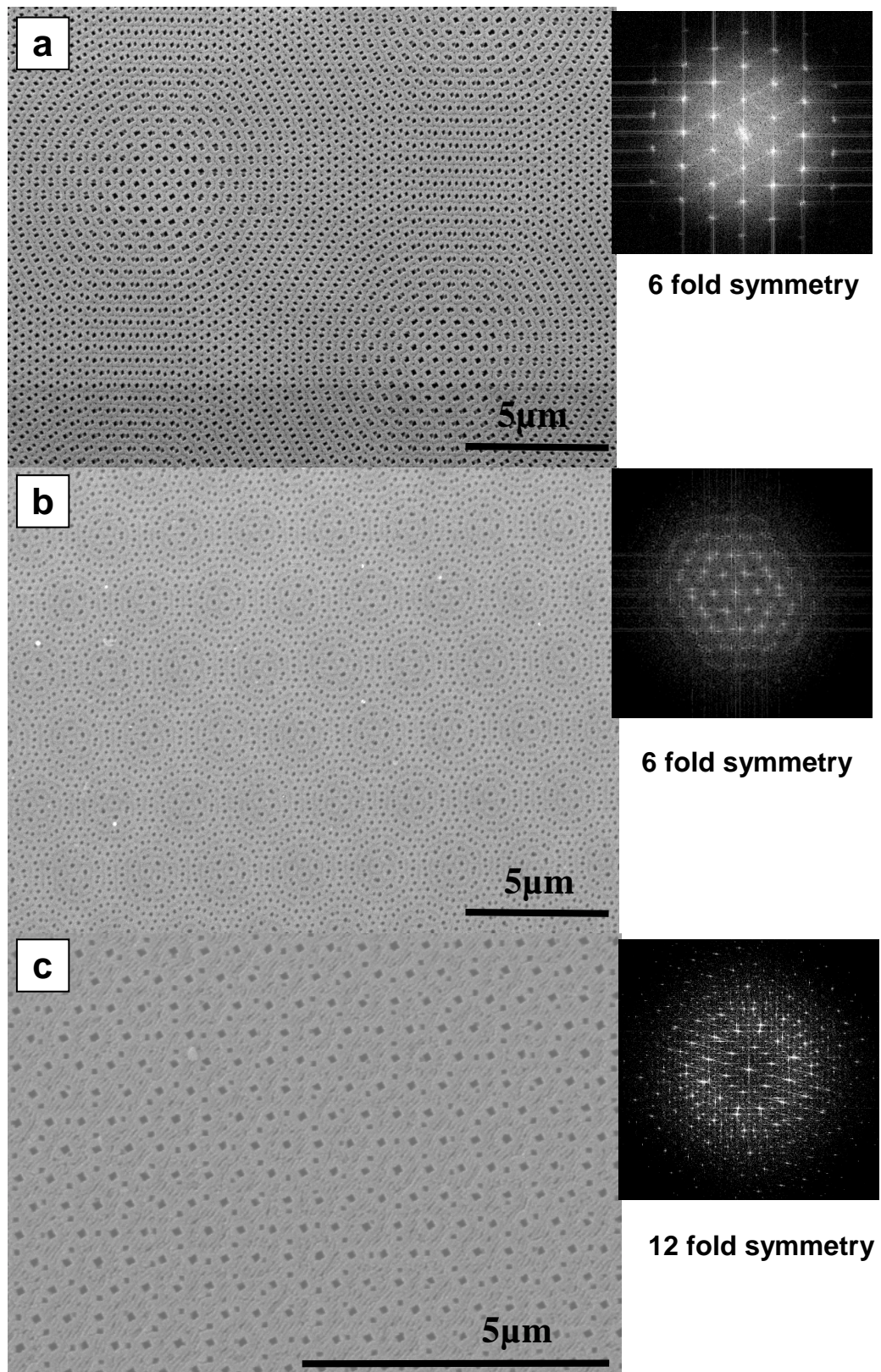


**Figure 4.18:** SEM images of the surface of porous alumina arrays with Moiré pattern. The patterns are formed by anodization of aluminum nanoidented with a rotation angle of (a) 2.2°, (b) 11.5° and (c) 30°. The Fourier-transform (FT) of the Moiré pattern is shown in the inset. The FT analyzes of the Moiré patterns are made from SEM pictures containing at least four superstructures.

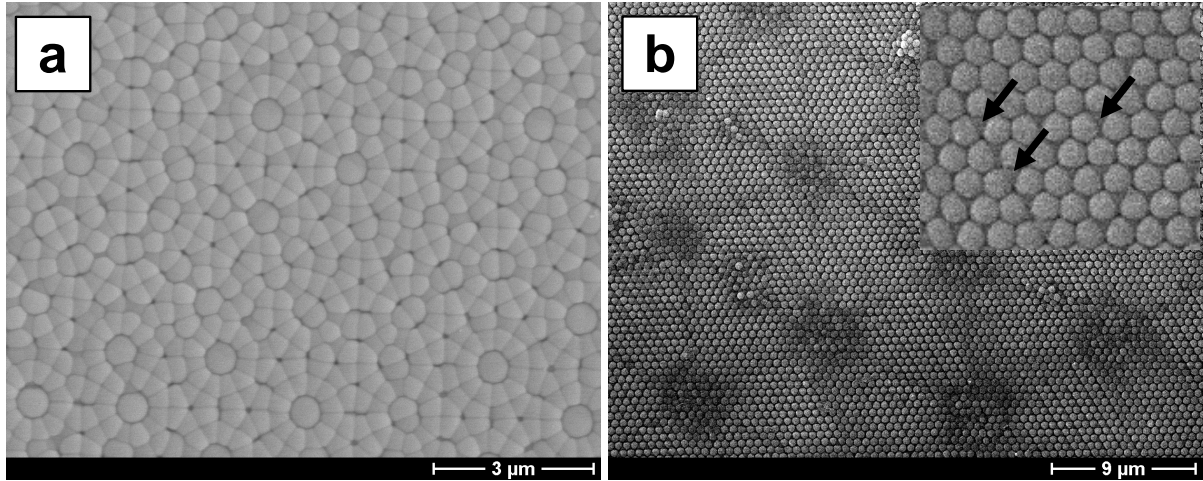


**Figure 4.19:** SEM image of (a) bottom view of Fig. 4.18 (c), which has been anodized for 10 min. Fig. 4.19 (b) shows SEM image of bottom view of Fig. 4.18 (a), which is anodized for 20 min. Pores, which have vanished during the course of anodization, are indicated by the arrows in the inset of Fig. 4.19 (b).

long. However, the Moiré patterns remain at the bottom of porous alumina, when the thickness of the alumina layer is less than about 500 nm. Note that before the anodization, the original depth of the patterns is about 50 nm, which is nanoindented under the pressure of 5 kN/cm<sup>2</sup> [66, 71]. Fig. 4.19 (a) shows the backside view of the porous alumina array of Fig. 4.18 (c) after selectively removing the aluminum in a Cu-containing solution. The pores grew for 10 min, which corresponds to a porous alumina thickness of around 500 nm. In comparison, the bottom view of Fig. 4.18 (a) is shown in Fig. 4.19 (b), which is twice as thick as that of Fig. 4.19 (a). Interestingly, even though a debris of Moiré pattern is still observed, the result looks like the single element pattern (Fig. 4.19 (b)). This can be explained as follows: during the pore growth, pores, which might be indented under a lower pressure than the others, are dying and pores originating from stronger pressure are surviving. If anodization is carried out for a much longer time, the nanoimprinted patterns disappear on the entire area [79].

In addition, the superposed patterns are replicated on a polymer film on Si. Fig. 4.20 shows an atomic force microscope (AFM) topography of the photoresist film which is spun on the porous alumina array of Fig. 4.18 (b). It indicates that the pattern of the porous alumina is well transferred to the resist. It is observed that the Moiré pattern of the polymer consists of a hexagonally arranged hillocks with a diameter of  $D_m = 2 \mu\text{m}$  and valleys in between them. The height difference between the hillocks and the valleys is measured to be less than 40 nm.

One strong advantage of the Moiré pattern method is that a position control of the master stamp during a second subsequent nanoimprint is not necessary to form reproducible patterns provided that the rotated angle is well controlled. Note that precise manipulation of position on the nanometer scale is very difficult while the angular control is very accurate regardless of the scales. In other words, a second nanoindentation with an arbitrary position and accurately controlled rotation angle can construct various Moiré patterns with high reproducibility (see Eq. 4.5). In particular, if  $D_{moi} \sim 2 D_{int}$ , a porous alumina array with a 12-fold symmetry can be obtained which is of great importance for low-refractive index photonic crystals [85].

This work shows that nanoimprint methods could be used not only for low cost and high resolution mass production but also for the fabrication of new types of patterns which cannot easily be achieved with conventional lithography [86].

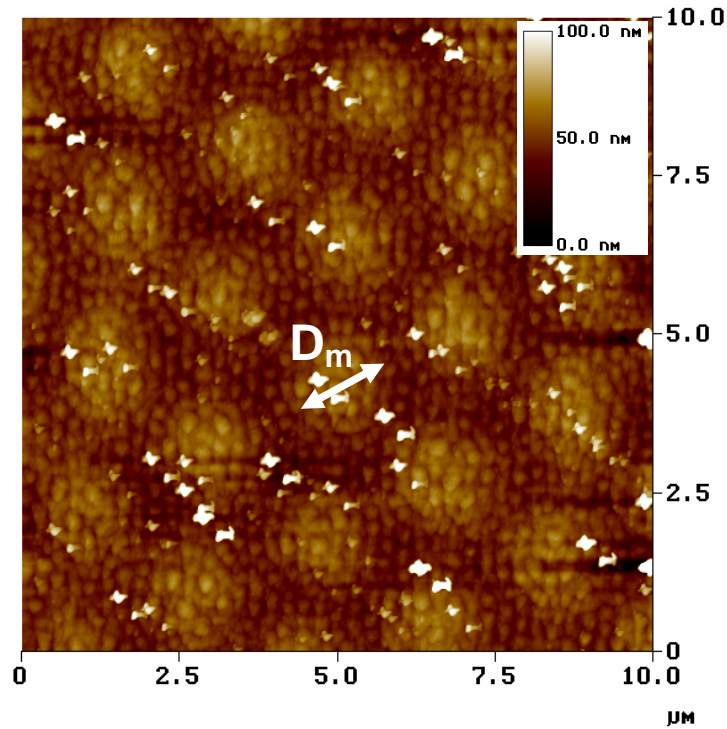


**Figure 4.20:** Atomic force microscope (AFM) topography of a photoresist replica with Moiré patterns of Fig. 4.18 (b).  $D_m$  is the diameter of the center of the superstructure which is slightly higher. The inset shows the height difference.

## 4.5 Monodomain porous alumina with modulated pore diameter

Three-dimensional structures having a periodic modulation of the channel diameter are of great interest for various applications. For example, 3D-phonic crystals are able to completely localize light in all directions. Schilling *et al.* demonstrated that based on a photoelectrochemical etching process in *n*-type Si, the channel diameter can be modulated by changing the illumination intensity [87]. However, the preparation of 3-D structures with a sub-100 nm feature size is still a challenge. Here, the feasibility of the preparation of such 3-D structures in monodomain porous alumina, which is able to be scale-down to a sub-50 nm size, is demonstrated.

As we already discussed in the chapters 1 and 2, the pore diameter is strongly influenced by the electrolytes. If the electrolytes are very acidic, porous alumina structures with a smaller diameter are obtained. With this knowledge, several attempts to achieve a modulation of the pore diameter was carried out.

### 4.5.1 Experimental

A schematic diagram of the procedures that is applied to achieve a modulation of the pore diameter in monodomain porous alumina is depicted in Fig. 4.21. The underlying principle is to change the electrolytes at regular intervals.

First of all, anodization of the nanoimprinted aluminum is carried out in 0.1 M phosphoric acid for 5 h (A in Fig. 4.21, it is the same process as in Fig. 3.7). After the fabrication of the monodomain porous alumina, second anodization is performed in 0.01 M oxalic acid for 10

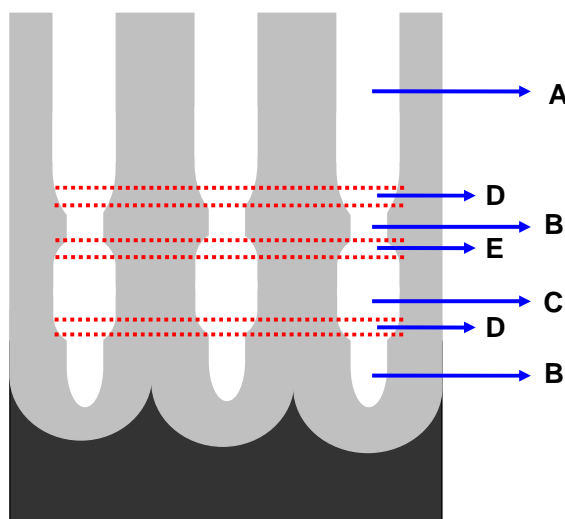


**Figure 4.21:** Schematic diagram of a periodic modulation of the pore diameter by changing the electrolytes at regular intervals. The modulated porous alumina channels are obtained as follows. **A:** By a long anodization in 0.1 M phosphoric acid, **B:** by 10 min in 0.01 M oxalic acid, and **C:** by 15 min in 0.1 M phosphoric acid, **D** and **E** in Fig. 4.21 show intermediate layers of increasing diameter and decreasing diameter, respectively.

min (**B** in Fig. 4.21). Then, the sample is anodized by changing the electrolytes at regular intervals. For example, it is anodized with 0.1 M phosphoric acid for 15 min (**C** in Fig. 4.21) and 0.01 M oxalic acid (**B** in Fig. 4.21) for 10 min at 195 V for each step.

## 4.5.2 Results and discussion

### Modulated features

The first layer formed in phosphoric acid after 5h (**A** in Fig. 4.21) allows preventing the breakdown of the oxide, which might occur under anodization in oxalic acid at a very high potential. If the protecting layer is not sufficient, the electrolyte species are able to penetrate the oxide insulator, leading to the breakdown of the first formed oxide. If the thickness of the oxide insulator is sufficient to prevent electrolyte penetration, a reaction due to a field-enhanced dissolution can only take place at the tips of pores. Therefore, the modulation by the anodization with oxalic acid is possible. Note, that if the anodization is performed in the potential range where oxalic acid is working, the first protective oxide layer is not required (see the Section 1.5.4).

The porous alumina structures with modulated diameters are shown in Fig. 4.22. By a numerical image treatment, the porosities are measured as 11 % and 7 % for the diameters obtained in phosphoric acid (**A** and **C** in Fig. 4.22) and in oxalic acid (**B** in Fig. 4.22), respectively. It is to expect that modulated pore channels with a higher contrast in diameter can be obtained by increasing the concentration of oxalic acid. However, the high concentration also leads to an increase in the probability of the electrical breakdown of the oxide.

### Oxide growth rate

The rates of porous oxide growth during anodization in phosphoric acid and in oxalic acid are determined by measuring the lengths of the modulated channels. For example, the modulated

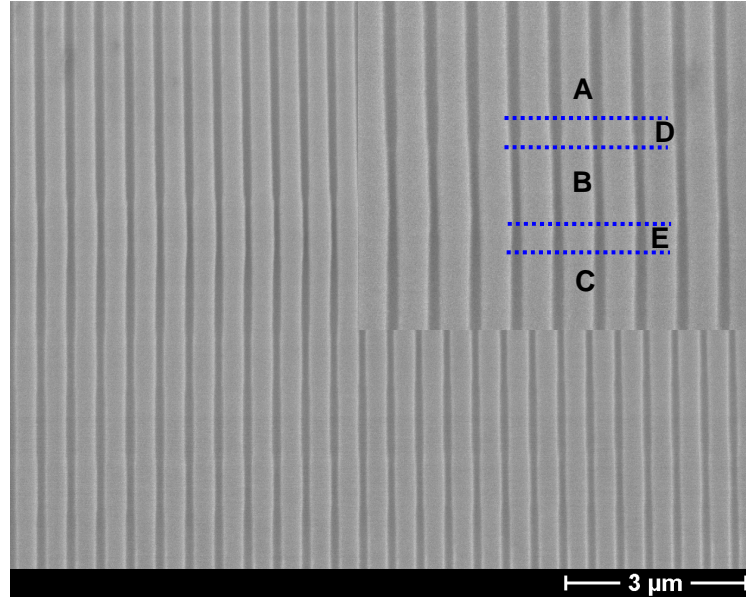


**Figure 4.22:** SEM images of modulated porous alumina channels. **A**, **B**, **C**, **D**, and **E** in Fig. 4.22 correspond to **A**, **B**, **C**, **D**, and **E** in Fig. 4.21.

channels as shown in Fig. 4.21 and Fig. 4.22 consist of four segments with different diameters; porous alumina channels with a larger diameter formed in phosphoric acid (**C** in Fig. 4.22), an intermediate layer with a decreasing pore diameter (**D** in Fig. 4.22), porous alumina channels with a smaller diameter formed in oxalic acid (**B** in Fig. 4.22), and an intermediate layer with an increasing pore diameter (**E** in Fig. 4.22). In fact, the lengths of **D** and **E** are equal. For the layers **B** and **C**, the lengths are determined to be around 730 and 930 nm, respectively. If we assume that the formation of the intermediate layers takes places during the course of anodization in the oxalic acid and phosphoric acid in the same proportions, the rates of the porous oxide growths are determined as 6.1  $\mu\text{m/h}$  for the oxalic acid, and 4.8  $\mu\text{m/h}$  for phosphoric acid.

### Inner oxide, outer oxides and modulated pore diameter

It is a very interesting question which part of the oxides, i.e., the inner oxide layer or the outer oxide layer (see the Chapter 2.1), compensates the reduced or increased pore diameter? One can consider that the the sum of these three contributions is always constant if the sample is anodized at a constant potential:

$$D_{int} = D_p + D_{inner} + 2D_{outer} = constant \quad (4.6)$$

where  $D_{int}$  is interpore distance,  $D_p$  is diameter of the pore, and  $D_{inner}$  and  $D_{outer}$  are wall thicknesses of the inner and the outer oxide, respectively.

It is obvious from Fig. 4.23 that the thickness of the inner oxide increases if the size of the pores is reduced. Then, the thickness of the inner oxide does not decrease again to the original thickness of the oxide that is typical for pores obtained in phosphoric acid even though the anodization is carried out again in phosphoric acid. According to the 10 % porosity rule [41], the ratios of  $D_{inner}/D_{outer}$  should be constant if the pores have high aspect ratios. The change of the ratios of  $D_{inner}/D_{outer}$  reflects the limitation of the modulation time. Therefore, modulations of more than 10 times should be very difficult to achieve with this method.

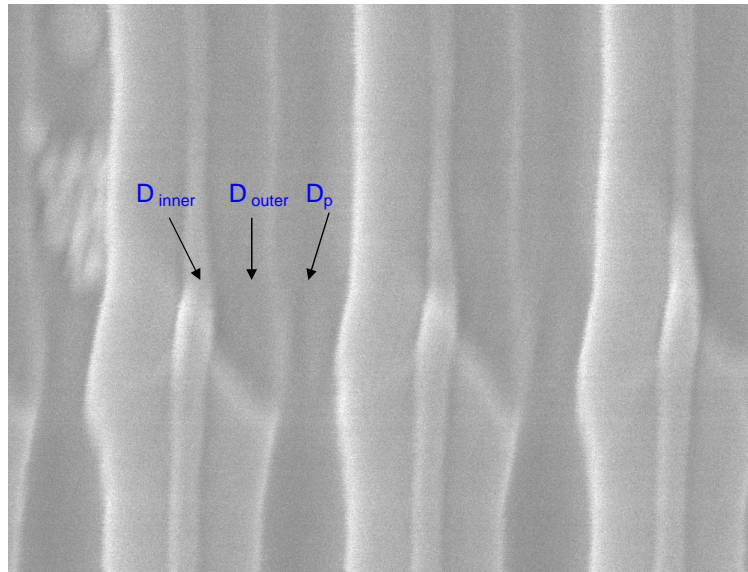


**Figure 4.23:** SEM images of variation of the thickness of the inner oxide layer and the outer oxide layer within the pore wall. The image shows a part of the pores where the diameter changes.

## 4.6 Summary

The combination of self-assembly and nanoimprint lithography allowed to prepare various porous alumina structures which are not accessible by conventional lithography or by self-ordering. For example, the interpore distance of porous alumina was reduced to 60% of the lattice constant of the master stamp by so-called smart nanoimprint. In other words, perfectly ordered porous alumina with 300 nm interpore distance by means of a 500 nm periodic master stamp was obtained. To explain the mechanism of smart nanoimprint, the theory of electric field boundaries was suggested, which was in good agreement with the experimental data.

Another achievement of this work was the preparation of monodomain porous alumina connected to nanobranches via a simple thinning process, followed by an anodization in the self-ordering regimes. The procedure could be a useful and easy technique to fabricate templates for nanowires with several outlets for distributing current, for studying electrical transport through nanowires or as antennas for amplifying signals. It was demonstrated that any kind of highly-ordered branches can be created underneath the monodomain porous alumina, if the branches is formed under the self-ordering conditions.

The third achievement was the fabrication of pore arrays with the Moiré patterns. Fabrication of porous alumina with a 12-fold symmetry, which is of great importance for low-refractive index photonic crystals, was demonstrated.

Modulation of the pore diameter was performed. It was demonstrated that the thickness in the inner oxide layer of the pore wall does not recover into its original thickness, and thus the number of modulation steps is limited.

Furthermore, monodomain porous alumina on Si can be obtained by the anodization of nanoimprinted Al deposited on a Si wafer.

# 5. Ti anodization: A comparison with aluminum anodization

In the previous chapters, the understanding of the parameters ruling self-ordering as well as imprint lithography to fabricate perfectly ordered porous alumina templates were described. Applying this understanding to other valve metals may allow not only to fabricate self-ordered porous oxides grown on other valve metals, but also potentially to improve our understanding of the growth of porous alumina. In this chapter, porous anodic oxide layers grown on titanium by electrochemical methods will be studied. The growth mechanism will be compared to the one governing the formation of porous alumina.

## 5.1 Titanium metal among valve metals

Al, Ti, Ta, Nb, V, Hf, W are classified as valve metals because their surface is immediately covered with a native oxide film of a few nanometers when these metals are exposed to oxygen containing surroundings [88, 89]. Inherently, these oxides retard the rate of reaction on the metal surface. Therefore, they have been widely used as highly protective layers resisting corrosion. Recently, valve metals again gained considerable interest, because some of their oxides have unique and excellent properties in optics, electronics, photochemistry and biology. For example, titanium oxide is a promising material for photoelectrocatalysis [90] and implants [91]. Titanium implants have intensively been investigated due to their superior strength and biocompatibility. However, an interface layer, e.g., a hydroxyapatite (HA) coating or porous titania layer, on the surface of the Ti substrate is necessary to osseointegrate with bones [92] because native  $\text{TiO}_2$  coatings have no ability to form a strong bond with bony tissue due to their rather low surface energy compared to  $\text{SiO}_2$  and  $\text{Al}_2\text{O}_3$ .

Porous templates based on other valve metals have been rarely studied since the 1970's. There were a few attempts to compare anodic oxide growth on other valve metals with porous alumina [93, 94, 95]. Zwillling *et al.* reported that porous titanium oxide is created in a chromic acid solution in the presence of a small amount of HF, whereas only a barrier layer titanium oxide is formed in pure chromic acid contrary to porous alumina [93]. According to their results, the  $\text{TiO}_2$  barrier oxide thickness is time-independent whereas the thickness of the porous oxide of titania increases with anodizing time. However, they did not report on the maximal obtainable thickness of the anodic porous titanium oxide. Gong *et al.* claimed that the final thickness of porous  $\text{TiO}_2$  structures formed in dilute HF solution is independent of the anodizing time [94]. They discussed that the dissolution rate of the formed  $\text{TiO}_2$  oxide is very high in HF even in the absence of an anodizing process.

## 5.2 Experimental

### 5.2.1 Preparation of polished substrates

High purity titanium foil (99.99%) with a thickness of 0.5 mm is purchased from Alfa Aesar Inc. After mounting the foil on a 4" glass substrate, it is mechanically lapped and polished using alumina suspension 0.04  $\mu\text{m}$  (OPS suspension, Struers) for 5h. Afterwards, the mechanically polished Ti is separated from the glass substrate in a non-solvent-cleaning-fluid (Logitech LTD, U.K.) at 80°C. Then, it is cut into the size of  $2 \times 2 \text{ cm}^2$  with a mechanical cutter (Profiform AG, Feather Products Modellbahnen GmbH, Switzerland). Electropolishing, e.g., in the mixture solution of 25 ml  $\text{HClO}_4$  (60 %, Merck) + 75ml  $\text{C}_2\text{H}_5\text{OH}$  (99.8%, Merck) which is typically used to obtain smooth aluminum surfaces (see the Section 1.5.4), is skipped because it would yield an oxide layer on the titanium substrate [52].

### 5.2.2 Nanoimprint

The fabrication procedure of a master stamp was already described in the chapter 3 (see Fig. 3.4). Prior to the indentation, dust on the surface is removed by a strong stream of  $\text{N}_2$  gas. Subsequently, a cut piece of our stamp ( $1 \times 1 \text{ cm}^2$ ) is placed on the mechanically polished Ti. The pattern on the master stamp is transferred onto the surface of titanium under a pressure of  $25 \text{ kN/cm}^2$  using the oil press (see Fig. 5.1) <sup>1</sup>.

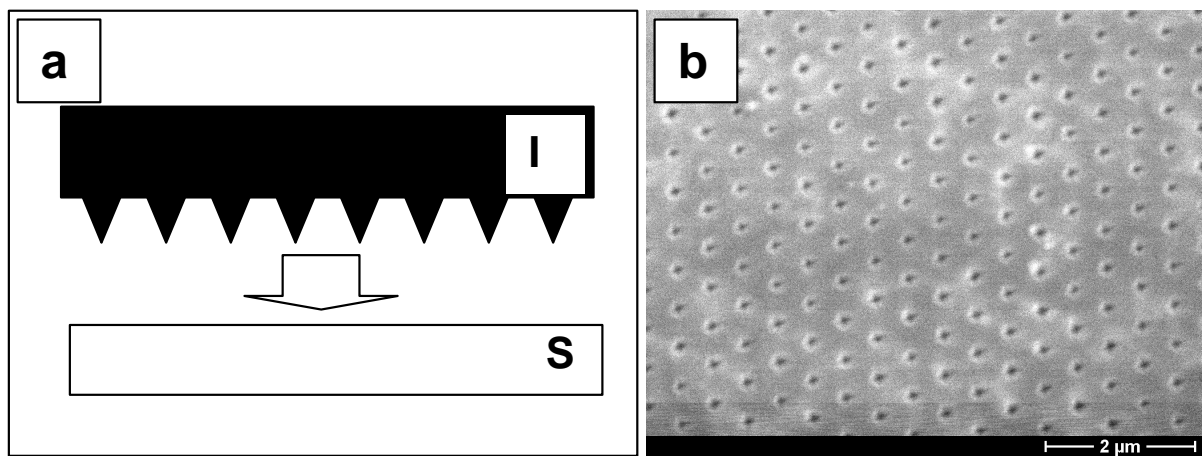


**Figure 5.1:** (a) Schematic diagram of the indentation of Ti under a pressure of  $25 \text{ kN/cm}^2$ . I: Imprint master stamp consisting of a hexagonal array of pyramids of  $\text{Si}_3\text{N}_4$  with a height of 260 nm and a lattice constant of 500 nm. S: mechanically polished Ti substrate. (b) SEM image of nanoindented surface of a Ti substrate.

### 5.2.3 Anodization and analysis

The Ti substrate is anodized under constant potential in aqueous phosphoric acid (1M ~ 4 M  $\text{H}_3\text{PO}_4$ ) or ethanolic hydrofluoric acid (0.5 M HF), using a potentiostat (Keithley 2400) interfaced to a computer. The cell is a two-electrode system consisting of a Pt mesh acting as the counter electrode and Ti as the working electrode. During the anodization, the temperature

<sup>1</sup>Young's modulus: 25 GPa for Al and 116 GPa for Ti [96]

and the speed of stirring of the electrolytes are kept constant. The morphology of porous titanium oxide is characterized by SEM (JEOL JSM-6300F). The thickness and the composition of the titanium oxide formed at different potentials are measured by Auger electron spectroscopy (Physical Electronics, PHI 600). The depths of the pores formed in ethanolic HF are analyzed by AFM (Digital Instruments 5000 microscope) using standard  $\text{Si}_3\text{N}_4$  tips. The scanning speed of AFM is 0.5 Hz.

## 5.3 Results and Discussion

### 5.3.1 Pore formation above the breakdown potential of the anodic oxide

#### Influence of the potential

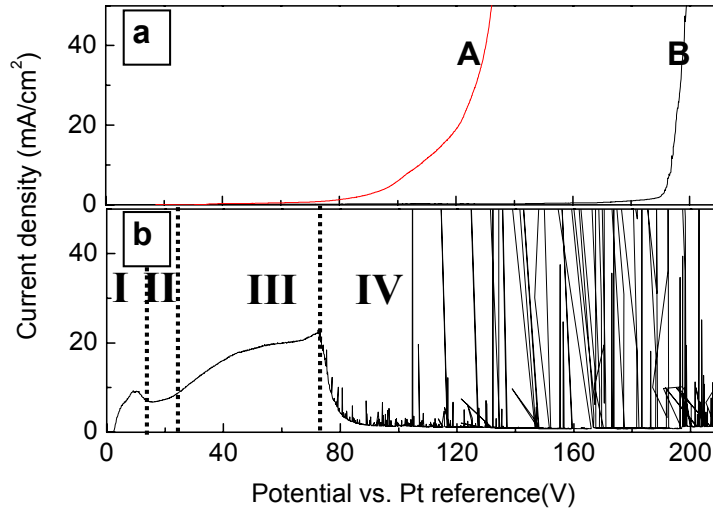


**Figure 5.2:** Linear sweep voltammogram (LSV) of aluminum and titanium. LSV is conducted with the sweep rate of 0.1 V/s in the range from 0 to 210 V. (a) LSV of aluminum. A: 0.26 M  $\text{K}_2\text{HPO}_4$  at 60 °C and B: 0.1 M  $\text{H}_3\text{PO}_4$  at 5 °C. (b) LSV of titanium at 60 °C in 4 M  $\text{H}_3\text{PO}_4$ . The LSV can be divided into four regions: amorphous oxide formation (Regime I), transformation into anatase (II ~ III), and transformation from anatase into rutile(IV) (Ref.[97, 98, 99, 100]).

Results of the titanium anodization are influenced by the growth modes, for example, constant potential, constant current density or both [101]. Here, we only discuss on the constant potential method to compare the fabrication process with that of porous alumina.

To investigate the effect of the cell potential, linear sweep voltammetry (LSV) with the sweep rate of 0.1 V/s is performed in the range of 0 V to 210 V in 4 M phosphoric acid at a constant temperature of 60°C. To minimize the influence of a reaction at the counter electrode on the LSV, a Pt wire acting as a quasi-reference electrode is inserted to the 2-electrode cell, placed adjacent to working electrode.

LSV's of aluminum in 0.1 M  $\text{H}_3\text{PO}_4$  and 0.26 M  $\text{K}_2\text{HPO}_4$  show a behavior that is typical for anodic oxides (Fig. 5.2 (a)). Initially, the current is very low and then suddenly increases at the breakdown potential of the anodic oxide.

In the case of titanium (Fig. 5.2 (b)) four different regimes can be observed, indicating there are transitions in the structure or changes in the reaction on the surface during the anodization.

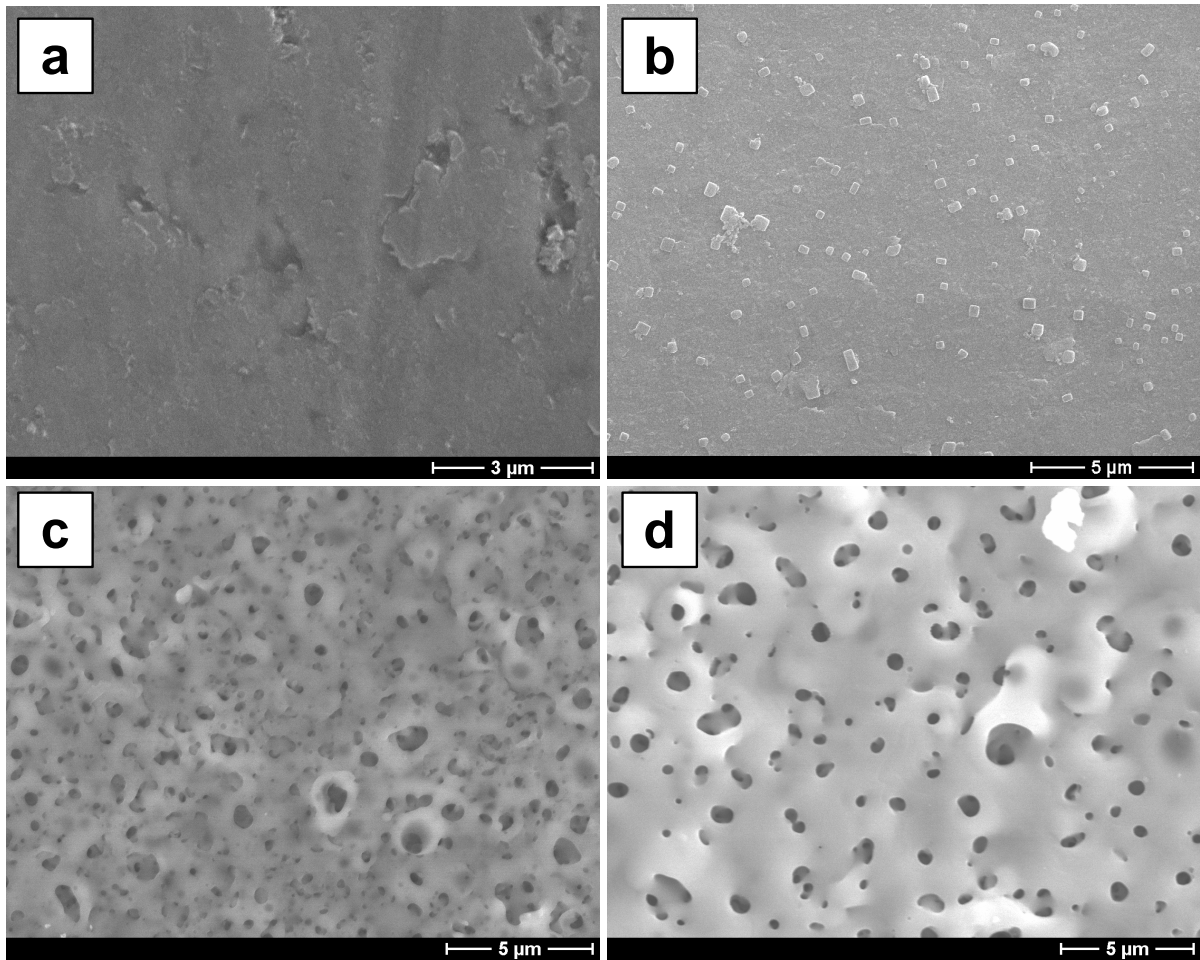


**Figure 5.3:** Effect of applied potential on the formation of pores. (a) 40 V, (b) 66 V, (c) 110 V, and (d) 160 V. Anodization conditions: 4 M  $\text{H}_3\text{PO}_4$  at 60 °C.

In fact, the current density below the breakdown potential is much higher than in the case of aluminum, demonstrating the higher conductivity of titanium oxide with respect to alumina. In the case of the anodization of titanium, the oxide is transformed as the potential increases from an amorphous phase into a crystalline phase such as anatase or rutile (brookite structure was rarely reported) [97, 98]. The potential increase in regime I in Fig. 5.2 (b) can be ascribed to the formation of an amorphous oxide on the entire surface [99]. Even though an exact understanding of the current density transients in the regimes II and III is missing, the phase transformation into anatase occurs in these ranges. Considering that the resistivity of the rutile phase is by a factor of around 1000 higher than that of anatase (at 100 °C), the decrease in the current density in the regime IV of Fig.5.2 (b) can be attributed to the transformation of anatase into rutile [100]. Rutile ( $\rho_{TiO_2} = 4.25 \text{ g/cm}^3$ ) is denser and thermodynamically more stable than anatase ( $\rho_{TiO_2} = 3.9 \text{ g/cm}^3$ ). The exact potentials at which the phase transformation occurs depend on the anodization conditions such as electrolyte and temperature [102, 103]. For example, Arsov *et al.* reported that during the anodization of titanium in sulfuric acid amorphous oxides are formed below 20 V, mixed oxide between 20 and 50 V and fully crystallized anatase at voltages higher than 50 V [102]. A sparking of the current is observed at higher potentials than 80 V (Fig. 5.2 (b)), indicating that the breakdown potential might be around 80 V. Interestingly, porous oxide structures are only obtained at potentials where sparking occurs (see Fig. 5.3). This is in agreement with the observation that pore-like morphologies are only formed above 100 V (sparking potential region) in sulfuric acid. The breakdown potential has been proposed to be related to the crystallization which leads to compressive stress in the oxide or to the threshold potential of oxygen evolution [98, 104, 105].

### **Influence of the temperature**

In the case of the anodization of aluminum, the temperature is typically kept below room temperature during the anodization to prevent the formed oxide from dissolving in the acidic solution. For example, if a porous alumina structure is formed at 65 °C in sulfuric acid, the porous alumina thickness does not increase because the rate of dissolution equals that of the growth of porous alumina [19, 106]. Furthermore, a constant temperature at the pore tips maintains a homogenous field-enhanced dissolution over the entire area, resulting in a porous alumina structure with straight pore channels and a narrow pore size distribution. Anodization of titanium was performed at 210 V in 1 M phosphoric acid at various temperatures. Fig. 5.4 reveals that porous structures formed at relatively low temperatures have veins of interconnected pores (or craters) and cracks caused by mechanical stress (Figs. 5.4 (a) and (b)). In addition, thick rims around the craters with diameters on the  $\mu\text{m}$ -scale are observed in the enlarged view of the SEM image (Fig. 5.4 (e)). In contrast, pore-like morphologies are created on the entire specimen at higher temperature (Figs 5.4 (c), (d) and (f)), even though the distribution is relatively broad. If the temperature is too high (here:  $T > 70 \text{ }^\circ\text{C}$ ), the rate of the dissolution would be as fast as that of the oxide growth.

### **Comparison with alumina anodization**

In table 5.2, a comparison of the physical properties of alumina and titania is given [88]. Since titanium oxide is a n-type semiconductor (with a high donor density of typically  $2 \sim 6 \times 10^{20} \text{ cm}^{-3}$ ) [101], the current is expected to be significantly larger than that of alumina. Anodic titanium oxide transforms from an amorphous to a crystalline phase depending on the applied

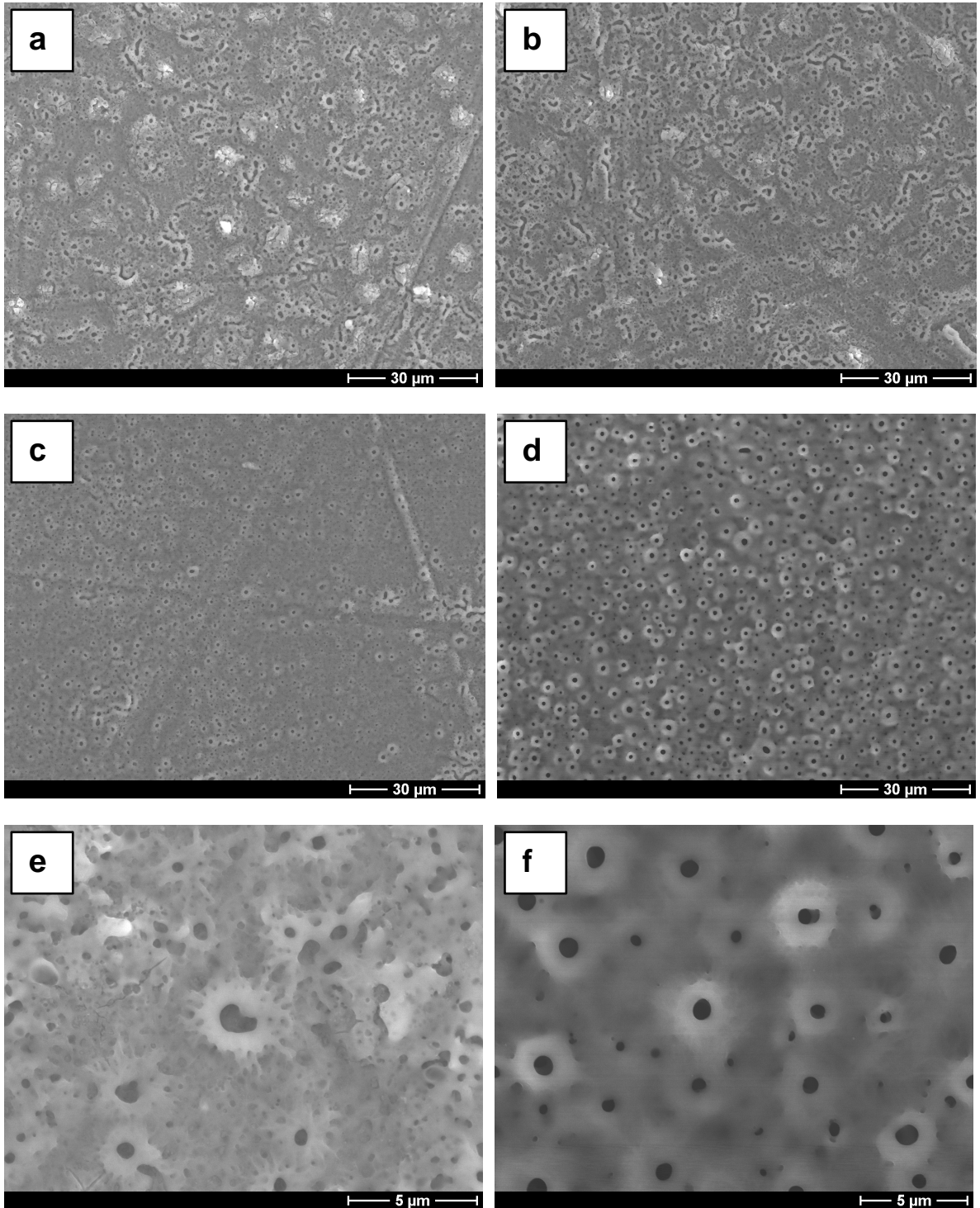


**Figure 5.4:** SEM top views of titanium anodized in 1M phosphoric acid at 210 V: (a) 5°C, (b) 20°C, (c) 45°C, (d) 60°C, (e) and (f) are enlarged views of (a) and (d), respectively.

	Compact alumina structures (so called barrier oxides)	Thick porous alumina structures with barrier layers	Aluminum etch tunnel or aluminum dissolution
<b>Schematic pictures</b>			
<b>Type of electrolytes</b>	Very weak acidic or neutral solutions	Medium or weakly acidic solutions	Strong acidic or basic solutions
<b>Pore density</b>	No pores	Constant with increasing anodizing time	Increase with increasing anodizing time
<b>Thickness</b>	Determined by applied potential	Determined by anodization time	Determined by diffusion limits of electrolytes

**Pitting potential/breakdown potential**

**Table 5.1:** Categories of anodically treated aluminum.

	Conduction type	Band gap(eV)	Type of anodic oxide
Aluminum oxide	Insulator	7 ~ 9.5	Mainly x- ray amorphous
Titanium oxide	n-type	3.2 ~ 3.8	Amorphous + crystalline

**Table 5.2:** Physical properties of aluminum oxide and titanium oxide.

potential or current density, whereas in the case of anodic aluminum only the amorphous phase is obtained.

It is well known that electrochemical anodic treatments of aluminum can be classified into three categories with respect to the formation of pits, pores, or a barrier layer (see Table. 5.1) [37]: 1) compact alumina structures (so called barrier oxides) in very weak acidic or neutral solutions (insoluble electrolytes) such as  $\text{H}_3\text{BO}_3$  or ammonium tartrate; 2) thick porous alumina structures with barrier layers at the interface Al/electrolyte in medium or weakly acidic solutions (slightly soluble in these electrolytes) such as  $\text{H}_2\text{SO}_4$ ,  $(\text{COOH})_2$ , or  $\text{H}_3\text{PO}_4$ ; 3) aluminum etch tunnels (pits) or aluminum dissolution by wet-etching in strong acidic or basic solutions such as HCl or  $\text{NaOH}^2$  [46].

Bearing in mind that porous titanium oxide structures are created above the breakdown potential, for aluminum, dissolution occurs above the breakdown potential (or pitting potential) whereas pores in aluminum grow below the breakdown potential. The breakdown potential in Al strongly depends on the electrolyte and temperature, and is, for example, more than 500 V in non-dissolving electrolytes like  $\text{H}_3\text{BO}_3$  but only a few milli-volts in HCl [19, 37].

These different growth regimes also influence the density of pores. In the case of pore growth in aluminum occurring below the breakdown potential, pores grow continuously with time. The formation of new pores on the surface can be neglected. The formed oxide layer acts as insulator to the flow of an ionic current. Thus, the reactions only occur at the pore bottom where a relatively thin oxide layer exists. However, in the case of aluminum dissolution above the breakdown potential, tunnel growth competes with the formation of new pits because not yet etched areas between tunnel pits are not insulating. Therefore, the density of pits on the surface increases with Al etching time [107].

In the case of titanium anodization, the density of pores formed above the breakdown potential increases with time, which is similar to the formation of etch tunnels in Al (Fig. 5.5). In Fig. 5.6, the density of pores in titania is analyzed as a function of the anodizing time. The density of pores increases linearly as a function of the logarithm of the anodization time. In addition, it is observed that new pores inside existing pores are created.

The thickness of the oxide layer grown on titanium has a maximum, mainly determined by the applied potential (2.5 ~ 3 nm/V) [89, 102, 108] but not by the anodizing time. In the case of porous alumina growth, the thickness of the porous layer increases with anodizing time but that of the barrier oxide is solely determined by applied potential [19, 37].

Fig. 5.7 shows Auger depth profiles<sup>3</sup>, demonstrating that the thickness of the anodic oxide on titanium depends on the applied potential rather than on the anodizing time. Assuming that all the samples formed at 210 V for 120 min or 1000 min, and at 80 V for 240 min consist of the rutile phase, the rate of depth-profiling is the same<sup>4</sup>.

It is observed that there is hardly a difference in the oxide thicknesses with increasing anodization time for a fixed potential (Fig. 5.7 (a) and (b)). Fig. 5.7 (c) shows that a much thinner oxide is produced because the anodization is carried out at a lower potential even though the anodization time is twice as long as in Fig. 5.7 (a).

---

<sup>2</sup>The meaning of anodization should be distinguished from that of etching. Anodization means an oxidation method to convert aluminum to alumina, e.g., the porous layer or the barrier layer (this is classified into the categories 1 and 2 in Table 5.1). Etching means a method to make pits, e.g., so-called tunnel etch pits, based on dissolution of metal (category 3).

<sup>3</sup>This provide quantitative compositional information as a function of depth below the surface.

<sup>4</sup>Therefore, the sputter time (Fig. 5.7) is proportional to the thicknesses of porous titania layers.

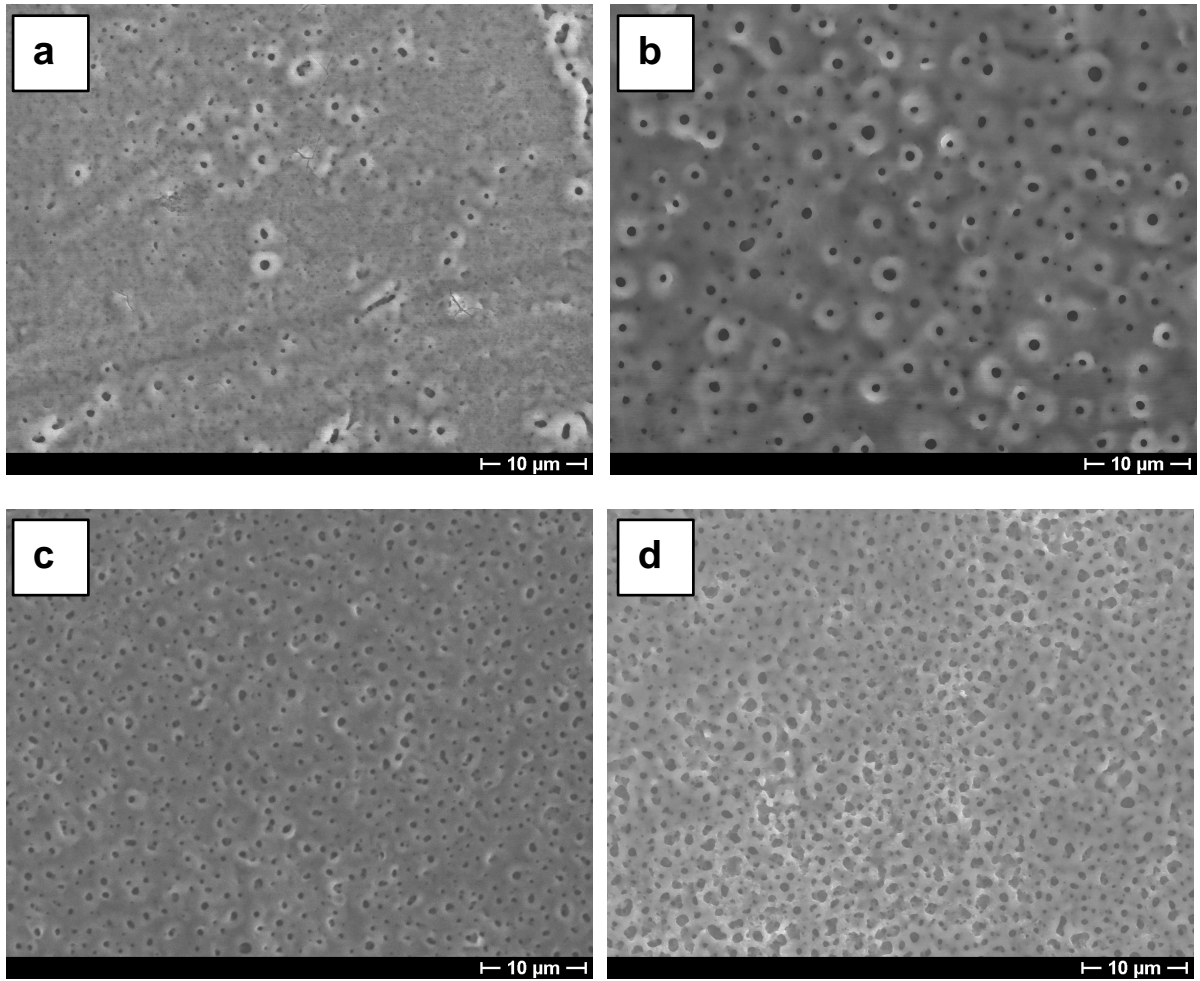


**Figure 5.5:** SEM top views of titanium anodized for different times. Anodization (210 V, 60°C, 1M phosphoric acid) is performed for: (a) 45 min (b) 120 min and (c) 1000 min (d) 3500 min.

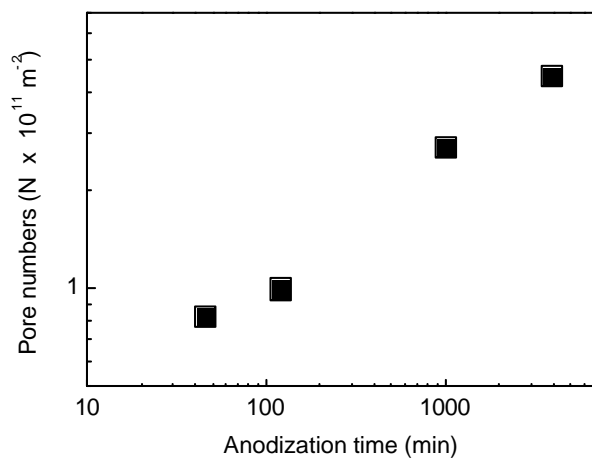


**Figure 5.6:** Statistic analysis of the density of pores shown in Fig. 5.5. Note that the pore density in porous alumina formed at 195 V (ideal case) is  $4.61 \times 10^{12} \text{ m}^{-2}$ .

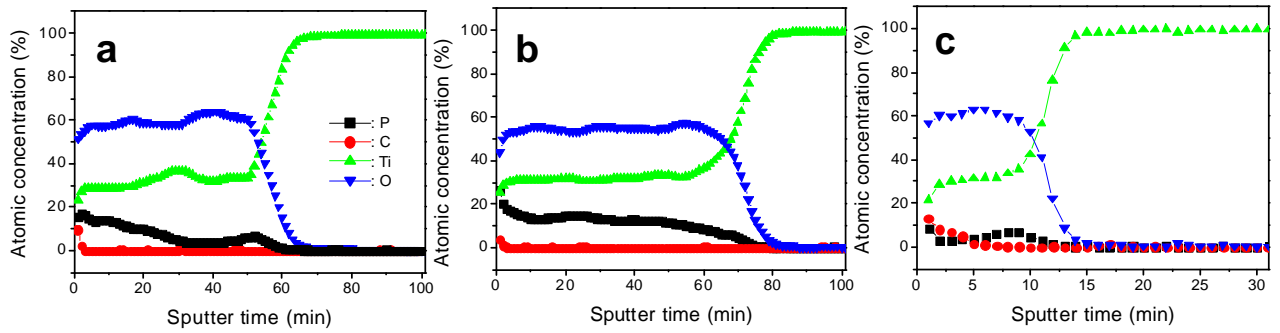


**Figure 5.7:** Auger electron spectroscopy (AES) depth profiles for oxide layers grown on titanium under different anodization conditions: (a) 210 V, 120 min, (b) 210 V, 1000 min and (c) 80 V, 240 min.

### Growth models

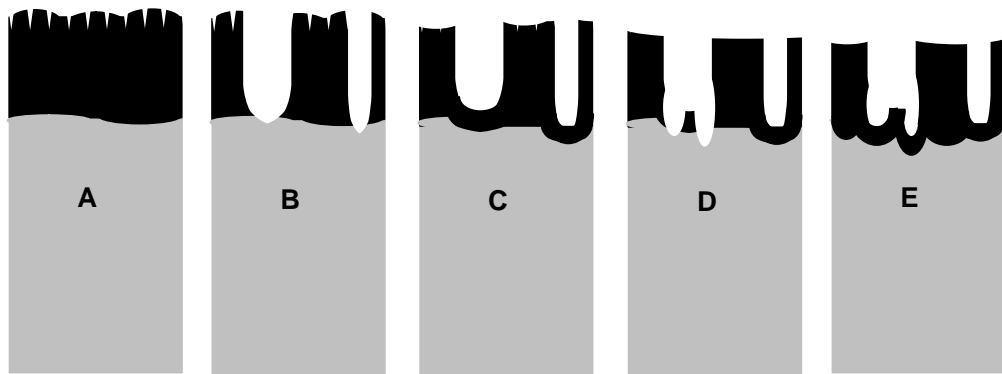


**Figure 5.8:** Schematic diagram of porous titanium oxide formation above the breakdown potential: (a) Oxide growth to maximal thickness, (b) Burst of oxide by the formation of crystallites (pore formation), (c) Immediate repassivation of pore tips, (d) Burst of repassivated oxide, and (e) Dissolution of the formed oxide and second repassivation.

The mechanism of growth of porous titanium oxide at high potentials is quite different than that of porous aluminum oxide because porous titanium oxide is formed above the breakdown potential.

The sparking potential might be related to pore formation on the surface as follows: As the thickness of a non-porous titanium oxide increases with the anodizing voltage, its structure undergoes transitions [Fig. 5.8 (A)]. If it is transformed to a dense crystalline structure such as anatase or rutile, the compressive stress in the oxide increases significantly. Breakdown of the oxide film occurs and new pores between the crystallites are formed [Fig. 5.8 (B)]. This corresponds to the occurrence of the sparking. However, the areas of electrical breakdown of the oxide are immediately covered with titanium oxide again [repassivation, Fig. 5.8 (C)] due to the characteristics of valve metals. If the breakdown occurs again inside the repassivated pores [Figs. 5.8 (D) and (E)], it looks like the formation of small pores inside the pores. Since current can flow through the whole oxide, the thickness of oxide cannot linearly increase with anodizing time.

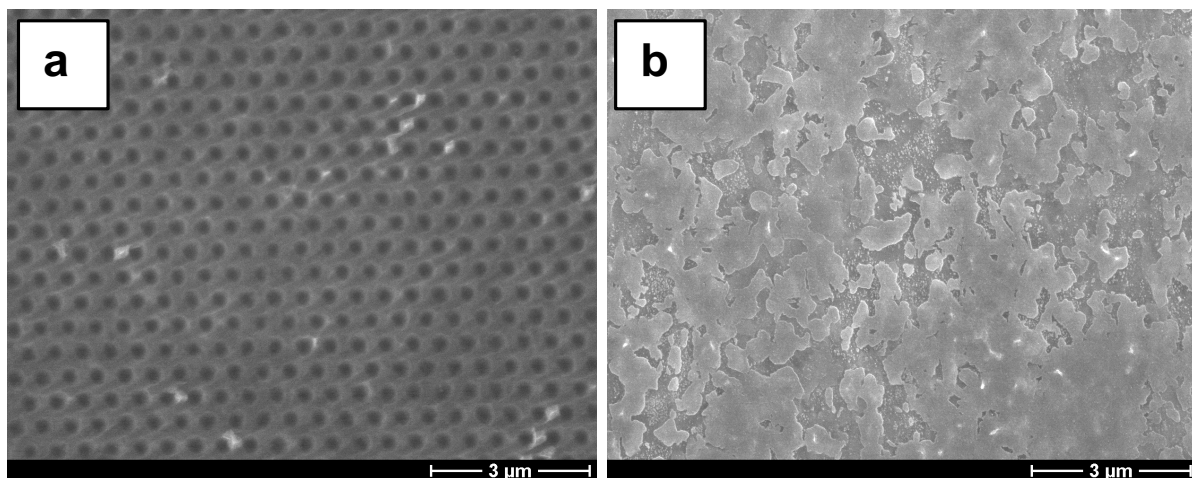


**Figure 5.9:** SEM images of anodized titanium at 10 V with prepatterns of 500 nm lattice constant: (a) in ethanolic 0.5 M HF for 240 min, (b) in aqueous 0.5 M HF for 20 min.

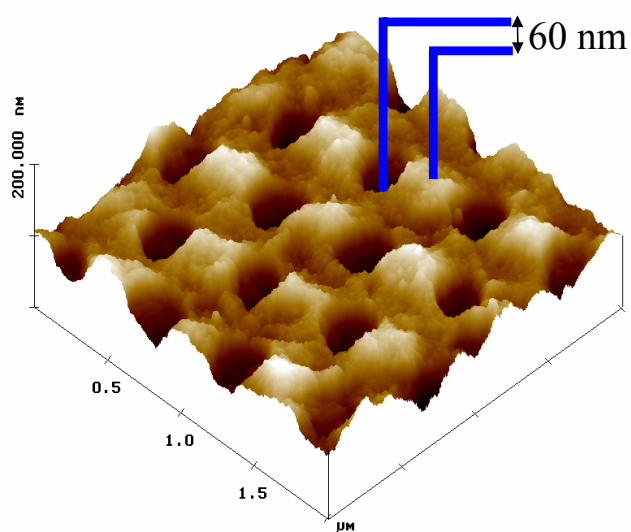


**Figure 5.10:** AFM topography of a titanium oxide array with 500 nm periodic pores. The average depth of pores is about 60 nm as determined by AFM.

### 5.3.2 Pore formation below the breakdown potential of the anodic oxide

Since pores are randomly formed above the breakdown potential as discussed in the previous section, the anodization of lithographically structured titanium cannot lead to form titania templates with an arrangement of pores remaining constant with time. In this section, the anodization of nanoindented titanium below the breakdown potential is studied to fabricate porous titania templates with a monodomain pore arrangement.

In Fig. 5.9 (a), a titanium oxide array with 500 nm interpore distance is shown which has been anodized in ethanolic 0.5 M HF at room temperature for 240 min at 10 V. Ethanol based electrolytes are used since anodization in aqueous HF electrolyte below the breakdown potential yields a coarse oxide layer on the surface of titanium [Fig. 5.9 (b)]. Under these conditions, the prepatterns on the Ti substrate disappear and porous structures like those formed above the breakdown potential are not created. This originates from the very fast dissolution rate of titanium oxide in aqueous HF. In the case of anodization in ethanolic HF, an oxide layer is formed whereas the structure of the prepatterns is maintained. AFM analysis reveals an average depth of the pores of about 60 nm after 240 min anodization (Fig. 5.10).

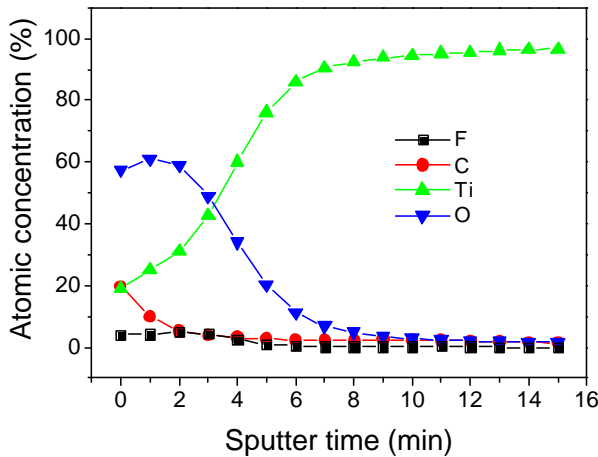


**Figure 5.11:** AES depth profiles for oxide layers grown on titanium in ethanolic 0.5M HF at 10 V for 240 min.

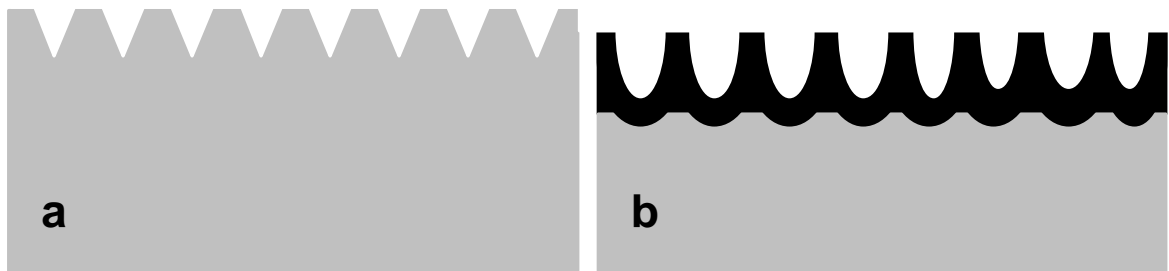


**Figure 5.12:** Schematic diagram of the formation of titanium oxide below the breakdown potential. (a) imprinted Ti substrate before anodization, and (b) oxide growth in inverted prepatterns after anodization.

The oxide formation on the surface can be confirmed by AES analysis (Fig. 5.11). Even though the deviation of the initial size of prepatterned holes is large at the beginning of anodization, the sizes become identical during the anodization. However, after a long time anodization ( $> 5h$ ), the monodomain titania structure becomes flat and eventually disappear due to the dissolution of the titanium oxide film. Note that the rectangular shape of the original prepatterns on the surface

of the Ti substrate is changed into more circular-like shapes during the anodization [Fig. 5.9 (a)]. This is also observed during the anodization of prepatterned aluminum [71]. It is also noteworthy that the areas which are not imprinted by the stamp have no pores but stay flat even after anodization, demonstrating the formation of barrier oxide under these conditions (Fig. 5.12).

## 5.4 Summary

The electrochemical anodization of titanium in different electrolytes, and their potential and temperature dependence were investigated in detail. It turned out that due to the semiconducting properties of titania, an analogous behavior to that of porous alumina cannot be accomplished. So-called porous titania in literature [93, 94, 95] corresponds to the pitting regime of aluminum where pores are created due to dielectric breakdown of titania or alumina, respectively. Below the breakdown potential of titania, only thick barrier layers can be formed. However, by nanoindentation of titanium and successive anodization of titania below the breakdown potential, monodomain porous titanium oxide with a pore depth of 60 nm on a  $\text{cm}^2$ -scale can be prepared. This work is a first step on the way to find new ordered porous structures for different valve metals.

## 6. Application I - Templates for silver nanowire growth

Monodomain porous alumina templates have versatile applications. For example, porous alumina can be used as template to prepare nanowires by various infiltration methods, e.g. sol-gel processes [12, 109, 110, 111, 112, 113, 114, 115, 116], electro-plating [9, 8, 10, 77, 79, 117, 118, 119, 120, 121, 122, 123, 124], electroless methods [125, 126] or chemical vapor deposition [127, 128, 129]. Synthesis and characterization of nanowires are very active research areas. Size-dependent physical phenomena that do not occur in the case of the corresponding bulk materials may emerge. Due to their unique properties, such as a large specific surface, nanowires are of considerable interest for applications in nanoscience [130, 131, 132].

Monodispersity of the nanowires is essential for many applications. Their size distribution is largely determined by the pore size distribution of the template. Monodomain porous alumina discussed in the previous chapters is very suitable as template material because it fully satisfies several requirements for the growth of nanowires: It is an inert material in a medium acid or base ( $4 \leq \text{pH} \leq 10$ ). On the other hand, since the alumina templates are dissolved in strong acids or bases, one can selectively remove them from the nanowires in a proper acid or base. The templates have a high thermal stability. Note that the melting point,  $T_m$ , of 99.9 %  $\text{Al}_2\text{O}_3$  is 2054 °C. The structures have a very narrow size distribution (see the Section 3.3.4). Both, pore diameter and pore length, are controllable with a very high reproducibility. Moreover, porous alumina can be fabricated at low cost.

The alumina templates themselves can be used as photonic crystals, membranes for filtering, or supports for catalyst. Applications of templates for nanowire growth and photonic crystals will be discussed in this chapter and the next chapter, respectively.

### 6.1 Electrochemical silver deposition into monodomain porous alumina

Since the thickness of the barrier oxide ( $D_B$ ) is proportional to the potential applied for aluminum anodization ( $D_B = 1.2 \text{ nm/V} \times \text{applied potential}$ ), the thick barrier film formed at high voltages is a big obstacle for a subsequent electrochemical deposition. Small fluctuations in the barrier oxide thickness lead to large current fluctuations and thus a very inhomogeneous filling. Therefore, a well controlled process for homogeneously thinning the barrier is vital to achieve a degree of nearly 100% filling with metals by electrochemical deposition. For thinning the thick barrier layer by more than 100 nm, a modified thinning process to that used by Nielsch *et al.* is developed [9].

It involves two different electrolytes: phosphoric acid is used for the thinning process from 195 V down to 80 V, and oxalic acid from 80 V down to 1V (See the Chapter 4.2). In this adopted thinning process, the applied potential is reduced stepwise similar to what is displayed in Fig.

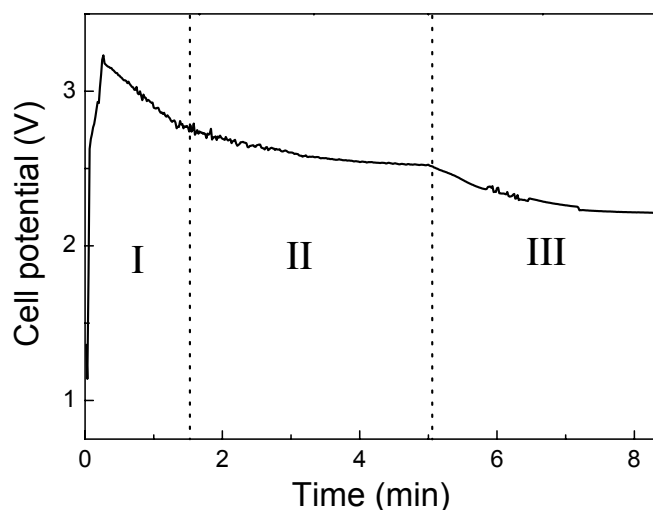


**Figure 6.1:** Initial potential curve during electrochemical silver deposition. I: overpotential regime to nucleate seeds of silver nanowires, II: stable nanowire growth regime, and III: potential drop regime where the Ag nanowires reach the top of the template.

4.8. In each step, a constant potential with 2 V lower than that of the former step is applied for 180 s in the range of phosphoric acid thinning. During the oxalic acid thinning, an exponentially decaying potential difference is applied for 30 s. The potential difference of the last step is only 0.01 V, whereas that of the first step is 2 V. Note, that if the thinning process is too fast, some pores will not be thinned. In contrast, if thinning is too slow, the undesired dendritic structures becomes very thick.

A commercial electrodeposition bath (Silver 1025, Technic Corp. [133]) under DC plating conditions ( $10 \text{ mA/cm}^2$ ) is used for the deposition of silver into porous alumina templates. The cell potential during the electrodeposition of silver is about 2.5 V, thus significantly larger than the breakdown potential of the remaining barrier layer. Therefore, DC electrodeposition is possible. During the deposition, the temperature is kept at  $25^\circ\text{C}$ . When the Ag nanowires reach the top of the template, there is a significant potential drop and deposition is stopped (see Fig. 6.1). SEM observations are performed to characterize the silver nanowires. The overgrown silver layer is removed by Ar sputtering with an ion mill (Gatan Duo Mill 600) for the top view images. Free standing silver rods are fabricated by dissolving the aluminum substrate in a Cu-containing solution for cross-section view images [9, 8].

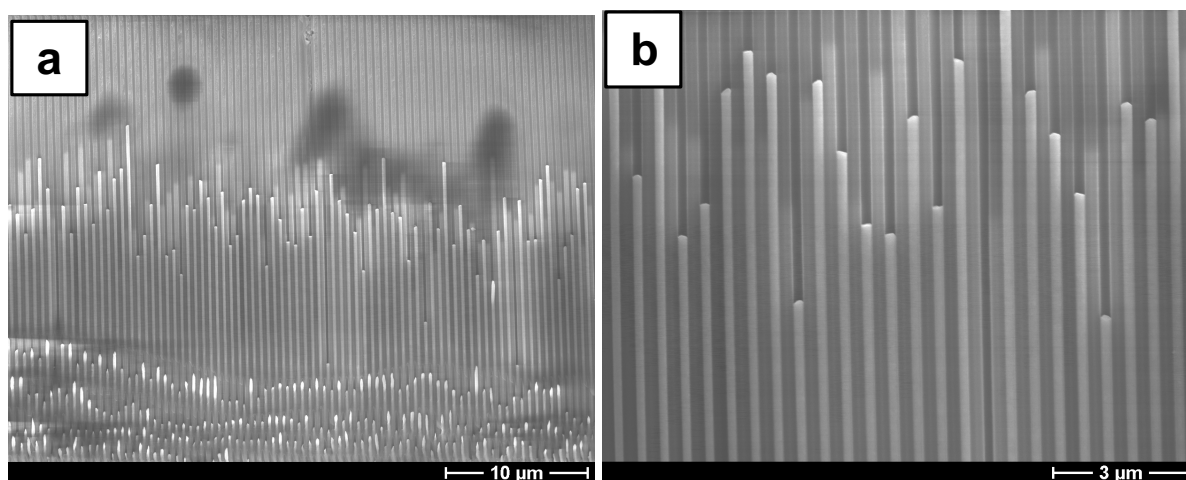


**Figure 6.2:** SEM image of a cross-section view of silver wires infiltrated in a monodomain porous alumina template with a pore diameter of 180 nm. The bright strips are silver wires. (a) Overview; (b) Magnification.

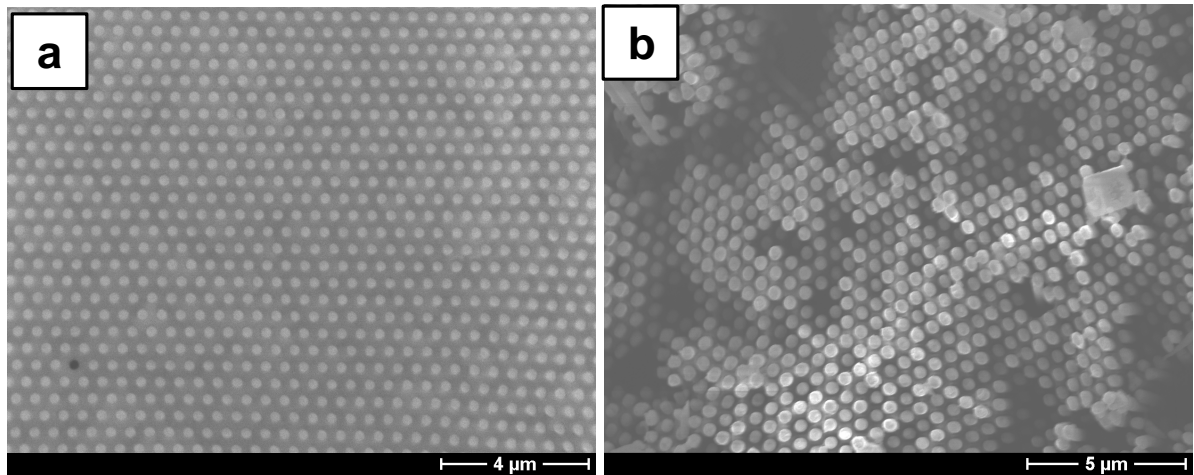


**Figure 6.3:** Top view SEM images of silver wires embedded in monodomain porous alumina with a) 300 nm pore diameter (top view after removing overgrown wires) and b) 400 nm pore diameter (top view after partly dissolving the alumina matrix in a chromic acid containing solution). Note that the difference in the darkness of color in Fig. 6.3 (b) indicates fluctuations of the height of the silver rods. The higher the rods, the brighter they appear.

The results for silver deposition achieved by DC deposition for 10 min are shown in Fig. 6.2. The average length of the silver rods is about  $22 \mu\text{m}$ . The filling of silver in the monodomain porous alumina template with straight long channels is almost 100% on large areas, thus enabling their usage as metallo-dielectric photonic crystals [134]. The growth rate of silver wires in the porous alumina channels is rather swift, compared to results obtained by either pulsed or electroless deposition [8]. By comparing the height of the silver rods as determined by SEM with the theoretical value obtained by considering the charge flow during the deposition, the current efficiency for the silver deposition is determined to be about 75%. In other words, the current consumed by hydrogen evolution, which is regarded the main side reactions, is rather low. This could be caused by the high concentration of  $\text{Ag}^+$  in the bath ( $\rho_e = 18 \Omega \text{ cm}$ ,  $\text{AgCN}$ : 2.5-10 wt% in the bath) as already pointed out by Sauer *et al.* [8].

To verify the general applicability of this method, porous alumina templates with widened pores ( $\sim 300 \text{ nm}$  and  $\sim 400 \text{ nm}$  diameter) are also infiltrated with silver. Subsequently, the alumina matrix is partly dissolved in a chromic acid containing solution for SEM observation of free standing silver wires. From the top view, it is observable that the silver wires embedded in the alumina structure are rods and not hollow tubes (Fig. 6.3 (a) and (b)). Furthermore, the filling degree is nearly 100 % and a coefficient of variation of diameter distribution is as low as 2.1% due to the high monodispersity of the template obtained via imprint process. As already mentioned in chapter 3 and 4, this is a significant improvement compared to disordered (21% dispersity) or even self-ordered pores (7.8% dispersity). However, there are some fluctuations in the height of the silver rods. This might be caused by the electrostatic instability which is inherent to electrodeposition of metal in parallel [8].

For comparison, silver electroplating on free standing porous alumina membranes is also performed. However, the preparation of such membrane structures is rather complicated and uniform metal back contacts on the porous alumina membrane are difficult to achieve. These problems result in lower degrees of filling compared to the method described above and a poor reproducibility.

## 6.2 Silver deposition into templates with branches

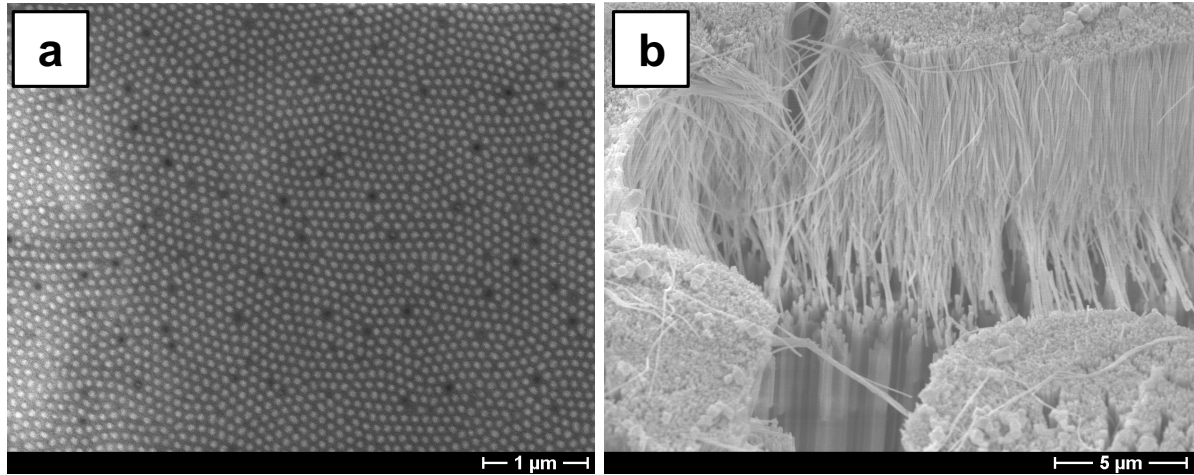


**Figure 6.4:** SEM images of branched silver nanowires. Monodisperse 180 nm diameter silver wires are connected with 40 nm diameter wires. Bottom view: (a) Silver wires deposited in a self-ordered branched alumina template with 100 nm interpore distance. Tilted side view: (b) Silver wires with several small branches. Typically 2-5 nanowires start to grow from one large nanowire. For the view with 10 degree tilting, the alumina matrix is partly dissolved in a chromic acid containing solution.

As already mentioned, it is possible to prepare hierarchically ordered structures, for example, monodomain porous alumina having 500 nm periodic pores connected with polydomain porous alumina having either 65 or 100 nm interpore distance (see the Section 4.2). For such self-ordered branches underneath monodomain pore channels, the thinning process is stopped at 40 V or corresponding to the self-ordering regimes of oxalic acid, instead of completely thinning down to 1 V. A self-arranged structure is grown during subsequent anodization in 0.3 M oxalic acid. Subsequently, the barrier layer is thinned down to 1 V for the electrochemical deposition of silver similar to the method described in the previous section. There are typically a few tens of small pores ( $\simeq 25$ ) branching from one large pore. A total length of 50  $\mu\text{m}$  is deposited with silver by the procedure as described above (Fig. 6.4 (a) and (b)). This type of structure consists of four parts: monodomain channels formed during anodization of imprinted aluminum, a dendrite layer formed during the thinning, self-ordered branches evolved during the second anodization and a dendrite layer formed during subsequent thinning from the self-ordering potential down to 1 V. Therefore, electrochemical silver plating into such a structure leads to monodisperse long silver wires with well-arranged branches. From a nanoscience perspective, this procedure could be a useful and easy technique to fabricate nanowires with several outlets for distributing current, for studying electrical transport through nanowires or as antennas for amplifying signals.

## 6.3 Silver deposition into porous Al films on Si

It is also possible to electrochemically deposit Ag into the pores after the fabrication of the monodomain porous alumina on Si substrate.

To obtain a homogeneously thinned barrier layer allowing to achieve a high degree of filling over the entire area, a thinning process is performed as described in the previous section. Since the

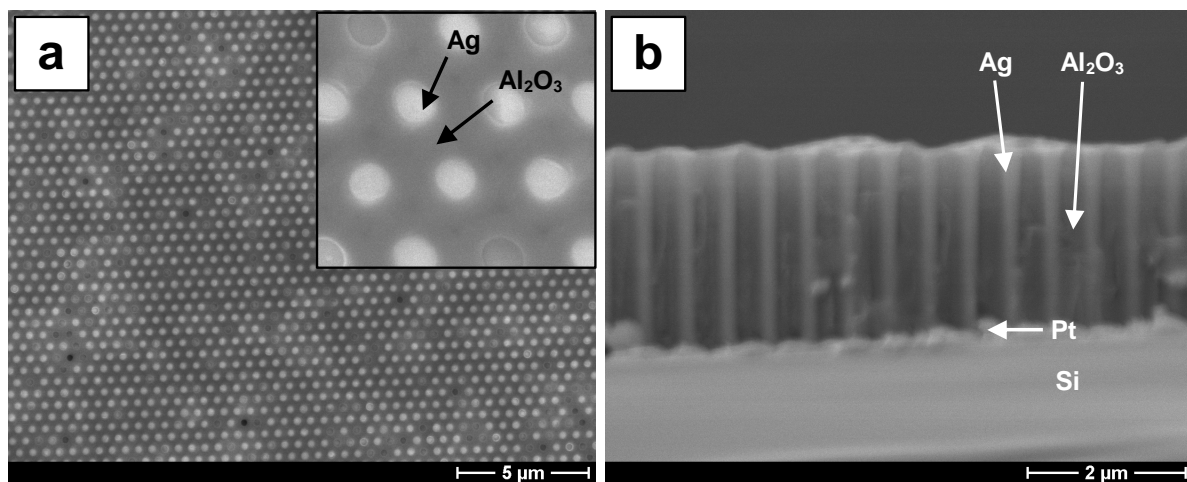


**Figure 6.5:** SEM images of silver deposited into an alumina template on a Si substrate: a) Top view and b) Cross-section view. Note that the different brightness indicates the height deviation of the wires. The degree of the filling of the silver rods is  $\geq 98\%$ .

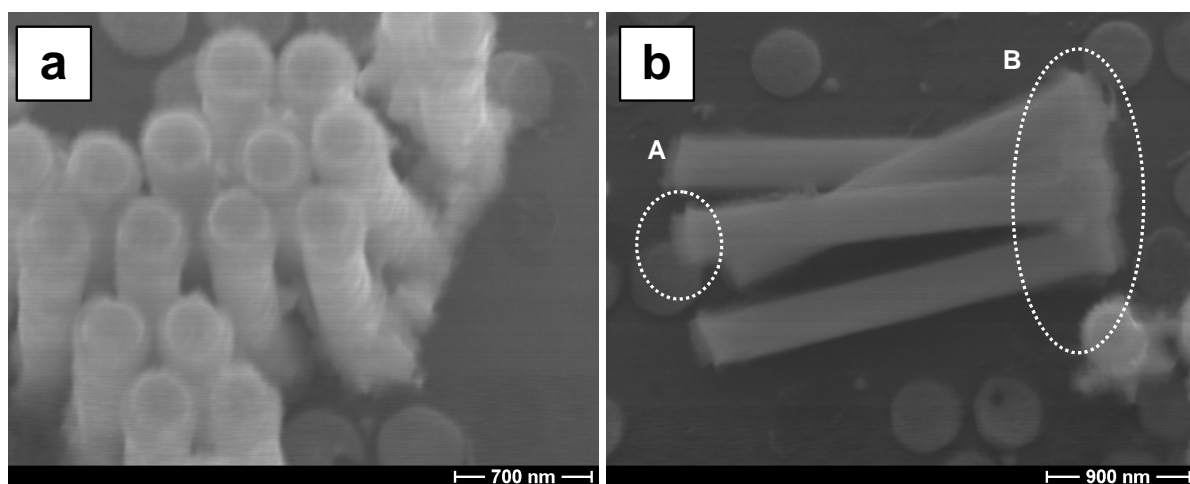


**Figure 6.6:** SEM micrographs of free standing silver nanowires on Si after dissolving the alumina matrix. Nanowires perpendicular to Si substrate are shown in Fig. 6.6 (a). Fig. 6.6 (b) shows nanowires which are lying on the Si substrate. A: dendrite layers and B: Ag layers overgrown on top of the alumina matrix.

remaining aluminum layer under the porous alumina is extremely thin, the dendrites diverging from the bottom of the porous alumina reach the Pt layer at about 135 V. In other words, almost all pores will directly be connected to the Pt layer at 135 V.

Figs. 6.5 (a) and (b) show silver nanowires embedded in the monodomain porous alumina on Si. The different brightness of the spots in Fig. 6.5 (a) indicates fluctuations of the height of the wires. Nevertheless, the homogeneity of the infiltration is very good over the entire area. It can be estimated that the degree of silver filling of the pores is  $\geq 98\%$ . In addition, free standing silver nanowires on Si are obtained after selectively dissolving the alumina matrix. Fig. 6.6 (a) shows that the wires on the Si substrate are perpendicularly oriented. Note that because of the aspect ratio ( $> 1$ ), the nanowires may break off in the course of the preparation of the free standing wires (Fig. 6.6). In the area **A** of Fig. 6.6, the nanowires are lying on the Si substrate. One can observe the dendrites formed during the thinning. Due to the overgrown silver layers on top of the wires, the silver nanowires are sticking to each other (see **B** in Fig. 6.6 (b)). However, Fig. 6.6 (b) demonstrates that the uniformity of the diameter is very good.

## 6.4 Summary

The preparation of Ag nanowires embedded in various alumina templates, e.g., monodomain structures, branched structures, alumina films on Si, by using electrochemical methods was discussed.

In contrast to the usually applied method of metal back contact based on free-standing porous alumina membrane, nearly 100 % pore filling was obtained due to a thinning process which allows a barrier layer of homogenous thickness of a few nanometers.

# 7. Application II - Porous alumina photonic crystals

Periodic dielectric materials allowing to control the flow of light are classified as photonic crystals (PCs) [135]. Numerous publications have already been dedicated to realize this concept with various materials. For example, PCs based on silicon are of great interest since they can be easily integrated into the already existing modern VLSI systems [7, 136]. Also, opal structures formed by self-assembly have been intensively exploited because of the potential to fabricate three-dimensional PCs [137, 138, 139].

## 7.1 Definition of photonic bandgaps

The definition of the photonic bandgaps is borrowed from that of the bandgaps in solid-state physics. For example, in a crystal, the interaction between the periodically arranged atoms and electrons moving through this lattice results in the formation of allowed and forbidden energy states, determining the properties of crystals.

Similarly, we can consider photons moving through transparent dielectric material with a periodic potential. If absorption of the light by the material is negligible and the contrast in refractive index between the two regions is high enough, light can not propagate in certain directions with specified energies due to the photonic band gap.

The photonic band gaps are determined by the configuration (geometry and spacing) of air holes and the contrast in refractive index. The size of photonic bandgap is determined by the refractive index contrast and by the filling ratio<sup>1</sup> of the higher-index material [140]. The location of the gap is determined by the lattice constant. For example, the wavelength of light in photonic band gaps can be roughly estimated by the spacing between the air holes (or the lattice size) times the sum of refractive index of the dielectric materials ( $\lambda_{gap} \sim 2(n_1 \times D_p + n_2 \times D_{Alox})$ ) [135].

## 7.2 Porous alumina photonic crystals

Due to their low absorption coefficient, excellent thermal stability and easy handling, porous alumina structures could be potential materials for PCs in the visible and infrared. The electronic bandgap of alumina is  $7 \sim 9.5$  eV.

Up to now, there have been no detailed studies in terms of real porous alumina structures of two layers: an inner layer consisting of a high purity alumina, an outer layer of alumina incorporated with anions, for example,  $\text{PO}_4^{3-}$  (see the Chapters 1 and 2) [24, 41, 141].

---

<sup>1</sup> = Pore radius ( $r$ )/Interpore distance ( $D_{int}$ )

In this chapter, we will discuss in detail large-area PCs based on porous alumina. The measured reflectivity will be compared with theoretical predictions. Moreover, a distribution of anions in the duplex oxide layers of the porous alumina wall to explain the optical properties is suggested.

### 7.2.1 Optical characterization of porous alumina

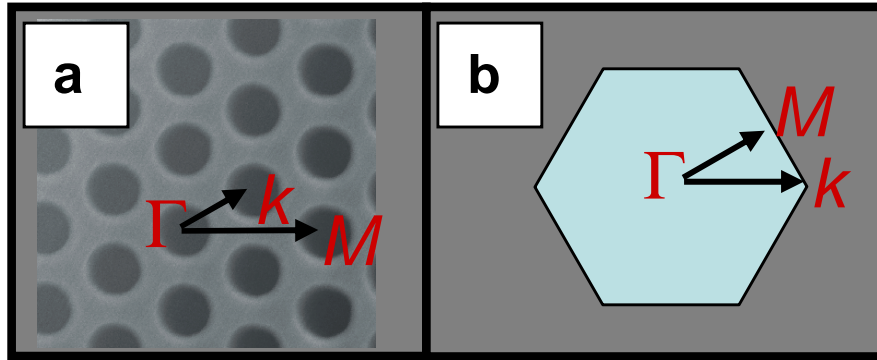


**Figure 7.1:** Hexagonal lattice (a) in real lattice space; (b) in reciprocal space. The high-symmetry directions  $\Gamma - M$  and  $\Gamma - k$  are indicated.

Before optical characterization, porous alumina membranes are prepared by selective etching of aluminum in a  $\text{CuCl}_2$ -containing solution. Afterwards, the membranes are cleaved mechanically and good cleaved planes are confirmed by SEM. For the optical characterization, the reflectivity of the porous alumina structures with different  $r/D_{int}$ -values are measured along  $\Gamma - M$  direction (see Fig. 7.1) with Fourier Transform InfraRed (FT-IR) Spectrometer (Bruker, IFS 66) equipped with a UV- $\text{CaF}_2$ -beamsplitter, a tungsten lamp, and a MCT detector.<sup>2</sup>

### 7.2.2 Optical setup

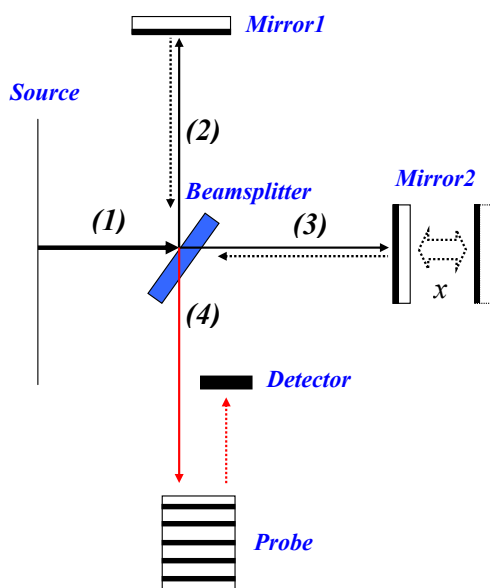


**Figure 7.2:** The Michelson interferometer.

<sup>2</sup>(HgCdTe) photoconductive detector. This fast detector is suitable for measuring the infrared radiation.

The underlying principle of the reflectivity measurement with the FT-IR microscope is based on a Michelson interferometer and Cassé - grain method. The Michelson interferometer consists of a beamsplitter, a fixed mirror (Mirror 1), and a translatable mirror (Mirror 2) (see Fig. 7.2). The beam radiated from the source (beam 1) is separated into two beams by the beamsplitter: half of the radiation is reflected to the fixed mirror (beam 2) and the other half is transmitted to the moving mirror (beam 3). The fixed and moving mirrors reflect the beams back to the beamsplitter. Again, half of this reflected beams is transmitted and half is reflected at the beamsplitter, resulting in one beam passing to the detector (beam 4) and the second back to the source.

The optical path difference ( $\Delta$ ), which is defined as the difference between the beams travelling through the fixed and moving mirrors, is

$$\Delta_p = 2 x n \cos(\delta) \quad (7.1)$$

Where  $x$  is the moving mirror displacement,  $n$  is the index of refraction of the medium filling the interferometer arms,  $\delta$  is the angle of the inclination of the beam relative to the optical axis. For a normal beam ( $\cos(\delta) = 1$ ) and for the air medium ( $n = 1$ ),  $\Delta_p = 2 x$ . The net optical path difference is  $\Delta = \Delta_p + \Delta_r$ , where the equivalent path difference arising from phase change on reflection,  $\Delta_r$ , is  $\pi$  due to two external reflections in the case of beam 2, whereas only one for beam 3.<sup>3</sup> If  $\Delta = m\lambda$  or  $(m + \frac{1}{2})\lambda$ , constructive or destructive interference of the two beams is produced, respectively, for every  $\lambda/2$  translation of one of the mirrors [142].

An interferogram<sup>4</sup> of a signal is collected as a function of the optical path difference. Afterward, the spectrum is obtained by performing a Fourier Transform (FT) on the interferogram as a function of wavelength. The measurement with the FT-IR spectroscopy is performed twice with and without the sample present. The signal originating from the sample is calculated from the difference between the two computed spectra.

To measure the reflectivity of the sample, the Cassé - grain method is employed as shown in Fig. 7.3. The angular apertures of the IR-objective is  $30^\circ$  (see Fig. 7.3).

A background measurement is performed on a silver mirror as a reference prior to the actual measurements.

### 7.2.3 Calculations of reflectivity and bandstructure

Bandstructures of the porous alumina PCs are calculated with the MIT package [143]. In addition, numerical calculations of reflectivity are performed by the transfer-matrix method [144]. The theoretical predictions are compared to the experimental results.

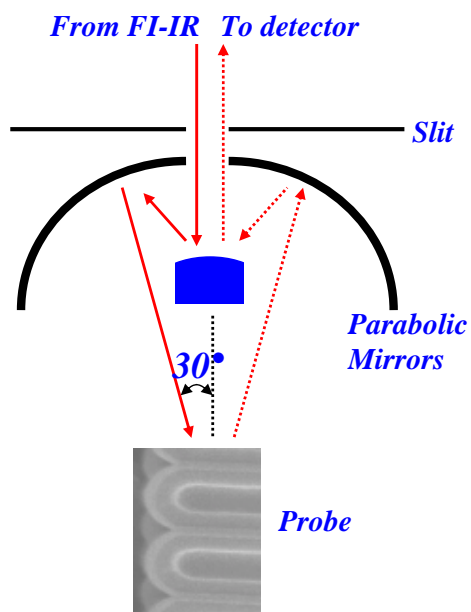
### 7.2.4 Duplex structure of porous alumina: inner and outer oxide

Fig. 3.7 shows monodomain porous alumina with 500 nm interpore distance and 100  $\mu\text{m}$  in length. The structure shows a defect-free array and straight channels. It should be suitable as PCs.

Details of porous alumina structures are very similar to those shown in Fig. 2.1 [41]. Fig. 7.4 reveals that the inner oxide layer near the cell boundary is about 50 nm thick. The outer

<sup>3</sup>A relative phase shift of  $\pi$  occurs by reflection of the light going from a lower index toward a high index, so-called the external reflection.

<sup>4</sup>The name of the signal format acquired by an FT-IR spectrometer.



**Figure 7.3:** Cassegrain mirror objective in the FT-IR microscope.

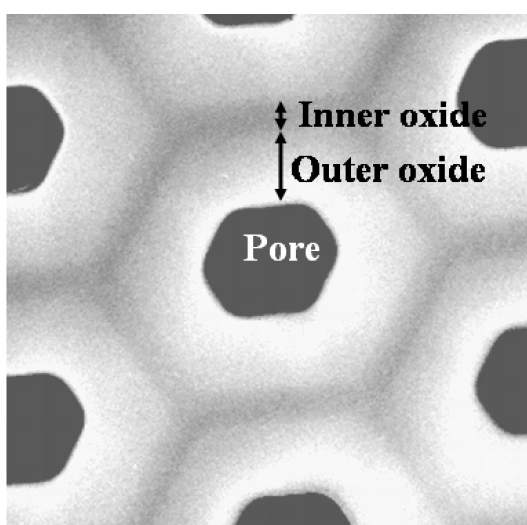


**Figure 7.4:** TEM image of a porous alumina array obtained by imprint lithography and subsequent anodization (195V, 1 wt%  $\text{H}_3\text{PO}_4$ ). The duplex oxide layers consist of an inner oxide and an outer oxide are visible. The thickness of the inner oxide is 50 nm, whereas that of the outer oxide decreases with increasing the pore diameter (initial diameter : 180 nm) by isotropic etching.

oxide layer is between the inner oxide layer and the air pore. As already discussed, the inner oxide layer is known to be composed of pure aluminum oxide, whereas the outer oxide layer has impurities such as incorporated anions [141]. The nomenclature of the inner oxide and the outer oxide was discussed in the Section 1.4.1.

It is reasonable to assume that phosphorus (P) and water ( $H_2O$ ) are major impurities since  $H_3PO_4$  is used as the electrolyte. Previous studies revealed that in the case of barrier oxide formation in phosphate solution, phosphorus in the form of  $PO_4^{3-}$  exists in the outer part and some protons are incorporated in the oxide at the electrolyte/oxide interface [145].

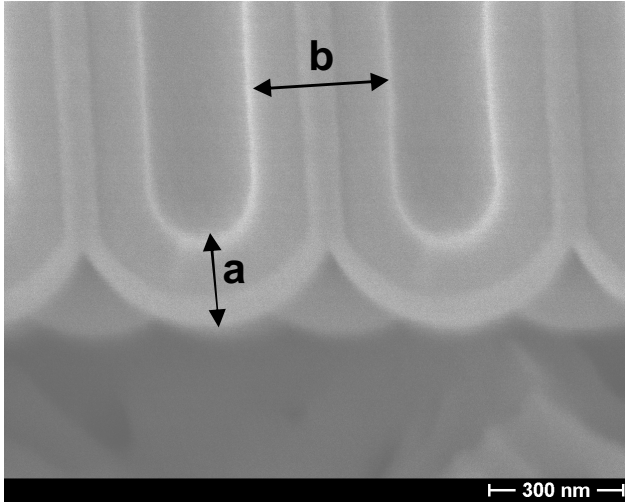


**Figure 7.5:** SEM micrograph of a cross-section of porous alumina formed under the same conditions of Fig. 3.7 and Fig. 7.4. The barrier oxide layer, the inner oxide, the outer oxide and the pore are clearly distinguishable. The interpore distance  $D_{int}$  is 500 nm. The arrows labelled as  $a$  and  $b$  indicate the thicknesses of the barrier layer and the wall, respectively.

The duplex layers of inner and outer oxides exist not only in the wall but also in the barrier layer at the pore bottoms (Fig. 7.5). The thickness of the outer oxide layer in the barrier is exactly the same as that in the wall. However, the inner oxide layer in the center of the hemisphere of the barrier layer is twice as thick as that in the wall, while the inner oxide at the edge of the hemisphere is the same thickness as that in the wall. This observation could be explained by the fact that maximum electric field is concentrated at the pore center [26].

## 7.2.5 Optical characterization

The reflectivity of porous alumina with different values of the  $r/D_{int}$ -ratio is measured along the  $\Gamma - M$  direction by an FT-IR equipped with a microscope. The measurement is carried out on a plane parallel to the long axes of the pores. The samples are prepared by carefully cleaving them. As described in the previous section, the porous alumina structures have duplex oxide layers with different dielectric constants. As a result, the effective dielectric constant of the whole structure is not constant for different values of  $r/D_{int}$ -ratio. In particular, we will see later that the outer oxide layer has a non-homogeneous effective dielectric constant depending on the concentration of impurities at different point.

As indicated previously [41], for the lattice constant  $D_{int} = 500$  nm, the porous alumina structure is only composed of the inner oxide layer when the pore radius  $r \geq 200$  nm. Therefore, the reflectivity of a sample with  $r/D_{int} = 0.4$ , which is composed of only inner oxide, is measured first. Note that pores are hexagonal and not round for this pore radius.

Figs. 7.6 (a), (b) and (c) show the reflection spectra in the  $\Gamma - M$  direction for the porous

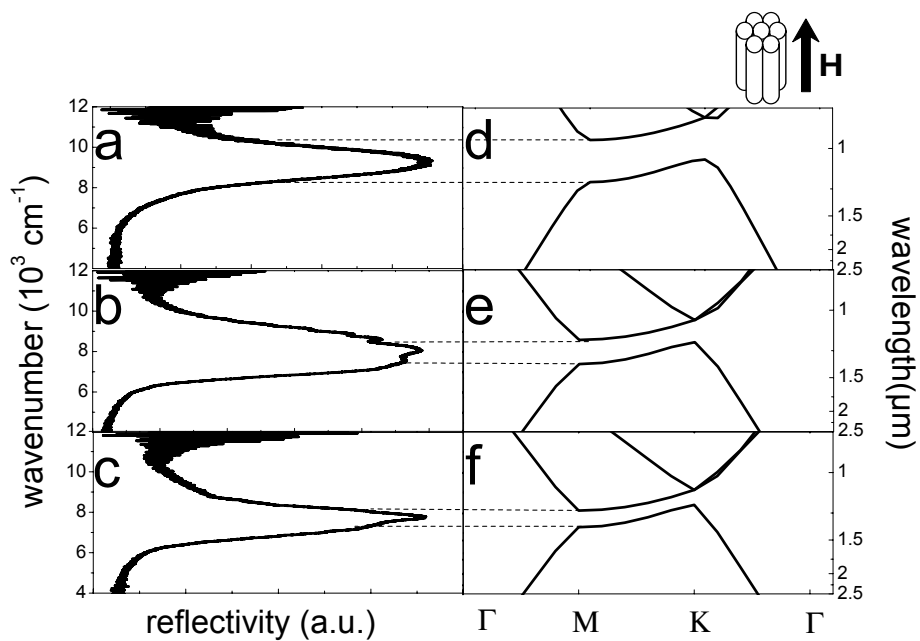


**Figure 7.6:** Comparison of the reflectivity measurements and bandstructure calculations ( $\Gamma$ -M direction, TE (H)-polarization) for different values of  $r/D_{int}$  ratio: (a)  $r/D_{int} = 0.4$ ; (b)  $r/D_{int} = 0.24$ ; (c)  $r/D_{int} = 0.18$ ; (b), (e), and (f) are bandstructure calculations of (a), (b), and (c), respectively.

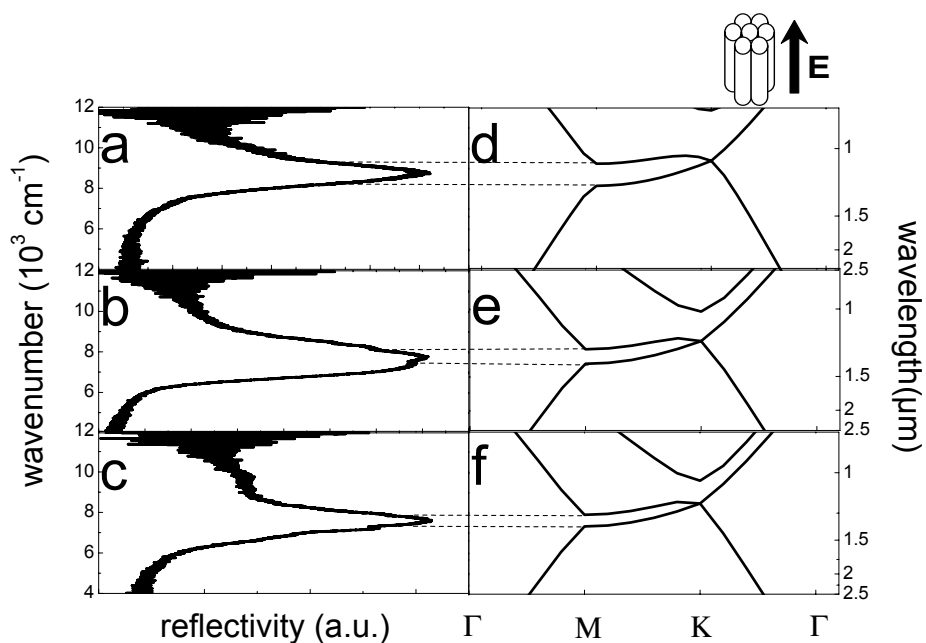


**Figure 7.7:** Comparison of the reflectivity measurements and bandstructure calculations ( $\Gamma$ -M direction, TM (E)-polarization) for different values of  $r/D_{int}$  ratio: (a)  $r/D_{int} = 0.4$ ; (b)  $r/D_{int} = 0.24$ ; (c)  $r/D_{int} = 0.18$ ; (b), (e), and (f) are bandstructure calculations of (a), (b), and (c), respectively.

alumina with  $r/D_{int} = 0.4, 0.24$  and  $0.18$ , respectively. The stopgaps<sup>5</sup> of TE polarization in  $\Gamma - M$  direction for these three  $r/D_{int}$  ratios are  $0.96 \mu\text{m} - 1.20 \mu\text{m}$ ,  $1.17 \mu\text{m} - 1.36 \mu\text{m}$  and  $1.28 \mu\text{m} - 1.41 \mu\text{m}$ , respectively. Fig. 7.7 shows that stopgaps of the TM polarization exist only in the  $\Gamma - M$  direction for all  $r/D_{int}$  ratios.

**Table 7.1:** Literature survey of refractive index,  $n$ , of alumina. Here, we assume that the dielectric constant of alumina,  $\epsilon$ , is equivalent to  $n^2$  due to a low absorption coefficient in the visible and infrared ranges.

Authors	Refractive index $n$	conditions
K. Huber [146]	1.65	unknown
G. Hass [147]	1.67 - 1.62 @ $\lambda = 0.3 - 0.6 \mu\text{m}$	3% Ammonium tartrate
S. Nakamura <i>et al.</i> [148]	1.64 @ $\lambda = 0.546 \mu\text{m}$	4.25% Phosphoric acid (140 V)

For both polarizations, the dielectric constant of the inner oxide is deduced by the position and width of the maximum reflection (photonic stopgap in  $\Gamma - M$  direction) compared to the theoretical calculation for different values of refractive indices. The dielectric constant of the inner oxide,  $\epsilon_{inner}$ , is determined by the bandstructure calculation which matches best the measured reflection in the porous alumina with  $r/D_{int} = 0.4$ . Here,  $\epsilon_{inner}$  is estimated around 2.8 (corresponding to  $n = 1.67$ ) for both E- and H- polarization, which is in a good agreement with the previously reported dielectric constant of pure aluminum oxide (Table 7.1). Note that among the three dispersion relations (Fig. 7.6 (d), (e) and (f)) for TE mode, a bandgap in all direction is opened for  $r/D_{int} = 0.40$  and  $r/D_{int} = 0.24$ . The dispersion relation for  $r/D_{int} = 0.18$  does not open a bandgap in all directions, but a stopgap in the  $\Gamma - M$  direction.

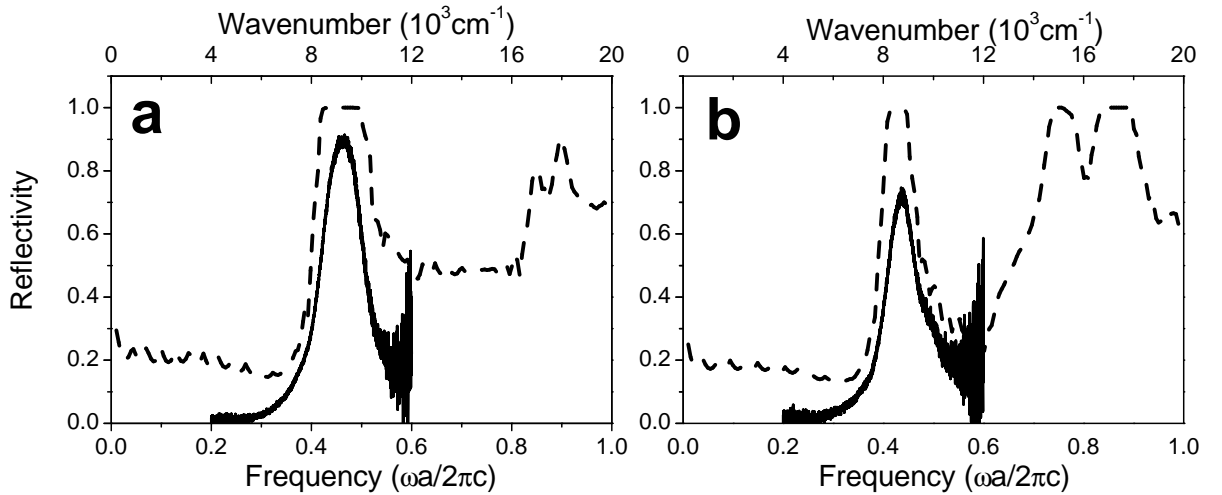


**Figure 7.8:** Reflectivity measured using an FT-IR microscope (solid lines) and calculations computed by the transfer matrix method (dashed lines) in case of  $r/D_{int} = 0.4$ . (a) TE (H-) polarization and (b) TM (E-) polarization.

In Fig. 7.8, the measured reflection spectrums of alumina PCs with  $r/D_{int} = 0.4$  in  $\Gamma - M$  direction for both polarizations are compared to calculation by the translight package. For both E- and H- polarization, the bandgap positions observed in the measurement are in good agreement with the calculated ones. In addition, for the TE mode, more than 90 % reflectivity within the stopgap is observed, indicating very low losses and high quality structures. For the

<sup>5</sup>Complete (Full) photonic bandgap: all directions and both polarizations, Photonic bandgap: all directions and one polarization, Photonic stopgap: one direction and one polarization.

TM mode, a slight blue shift on the high frequency side implies a stronger angular dependence of the E-polarization since the IR-objective has an angular aperture of  $30^\circ$  (see Fig. 7.3).

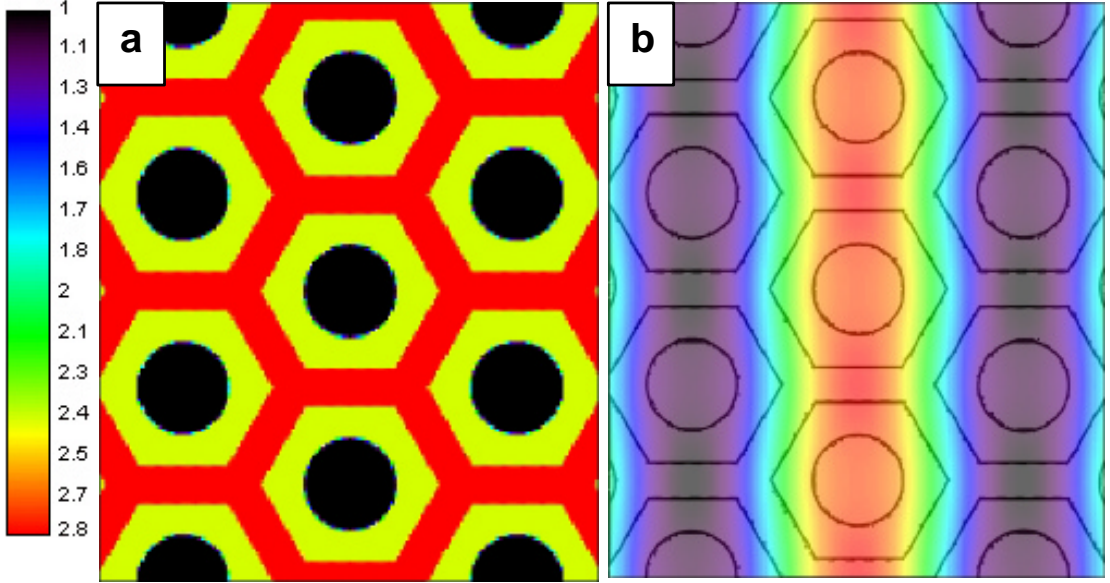


**Figure 7.9:** (a) Map of the dielectric constant for the theoretical calculation in which different values of dielectric constants are shown in the left scale bar. The corresponding H-field distribution of the TE mode at the  $M$ -point of the air band of the fundamental bandgap is described in (b).

After determining the refractive index of the inner oxide, a series of reflectivities of both polarizations for different values of the  $r/D_{int}$ -ratio, which represent the different thicknesses of the outer oxide layer, are measured. For each polarization, bandstructures are calculated for every value of  $r/D_{int}$  with a series of dielectric constants of the outer oxide, taking into account that the porous alumina structure has duplex oxide layers. As shown in Fig. 7.9 (a), the duplex porous alumina structure is composed of dielectric constants of the air pores ( $\epsilon = 1$ ), the outer oxide layers (non-uniform values of  $\epsilon$ , e.g.,  $2.4 \sim 2.7$ ), and the inner oxide layers ( $\epsilon \simeq 2.8$ ), which are represented by the black, yellow, and red colors, respectively. The corresponding magnetic field distribution at the  $M$ -point of the fundamental dielectric band is shown in Fig. 7.9 (b). The color indicates the amplitude of the magnetic field. Note that this mode has the tendency to concentrate most of its displacement energy in the high  $\epsilon$ -area in order to lower its frequency. Since the displacement field is largest along the nodal planes of the magnetic field, the light blue regions are where the displacement energy is concentrated. These regions represent the alumina part, especially the inner oxide layer.

For each polarization, the value of the dielectric constant which gives the best fitting to the measured bandstructure is selected as the effective refractive index of the outer oxide. This effective dielectric constant in the outer oxide,  $\epsilon_{\text{eff,outer}}$ , is not a constant for different  $r/D_{int}$  values. As shown in Fig. 7.10, for a value of the  $r/D_{int}$ -ratio between 0.18 and 0.33,  $\epsilon_{\text{eff,outer}}$  varies from 2.6 to 2.4 and then to 2.6 for the TE mode, from 2.6 to 2.4 and then to 2.7 for the TM mode. Note that when the  $r/D_{int}$  value is between 0.28 and 0.40, the  $\epsilon_{\text{eff,outer}}$  is different for E- and H- polarization. This reveals the birefringence of the porous alumina structure.

Fig. 7.11 shows the gapmap of the first stopgap positions in  $\Gamma - M$  direction calculated by MIT package as well as measured by the FT-IR microscope. The agreement between theory and measurement is very good. As the filling factor  $r/D_{int}$  increases, the bandgap edges for both polarizations shift to higher frequency. The bandgap widths also increase due to the higher

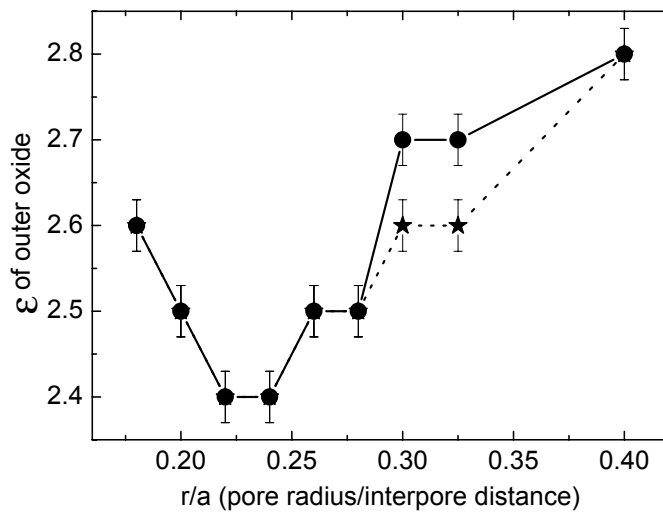


**Figure 7.10:** Effective dielectric constant of the outer oxide as a function of the  $r/D_{int}$  value ( $\star$  : TE mode and  $\bullet$  : TM mode). Note that the points where  $r/D_{int} = 0.4$  represent the dielectric constant of the inner oxide.

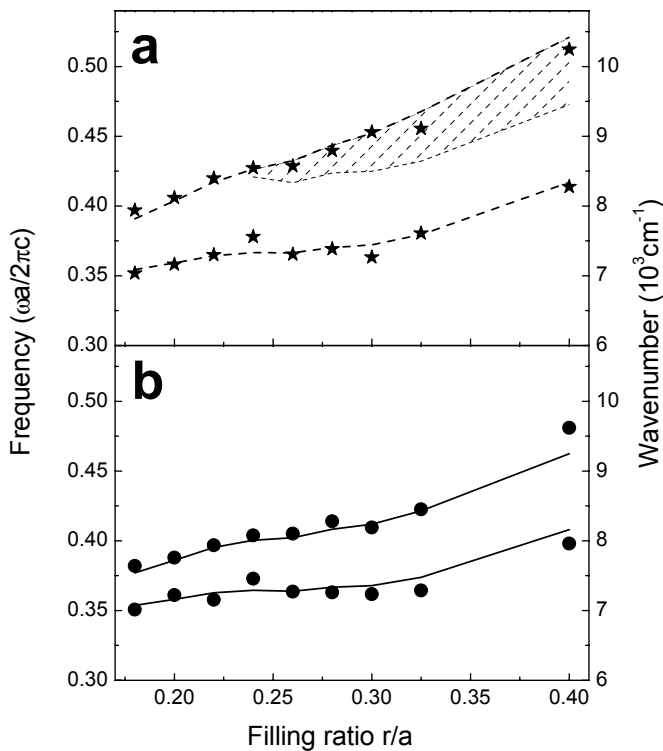


**Figure 7.11:** Map of stopgaps as a function of the filling ratio  $r/D_{int}$ . (a) The TE-mode: Stars ( $\star$ ) indicate stopgap from the reflectivity measurements in  $\Gamma$ -M direction. Dashed lines correspond to theoretical calculations of the stopgap. The hatched area indicates the calculated photonic bandgap in all in-plane directions which is deduced from bandstructure calculations. (b) The TM-mode: Dots ( $\bullet$ ) represent the stopgap from the reflectivity measurements in  $\Gamma$ -M direction. The calculated stopgap is shown in solid lines. Note that there is no photonic bandgap in all in-plane directions for the TM mode due to the low dielectric constant contrast.

dielectric contrast of the whole structure. In the figure 7.11 (a), the hatched area shows the calculated photonic bandgap frequency range for the TE mode. The maximum gap-midgap ratio<sup>6</sup> is 9.73 % for  $r/D_{int} = 0.40$ . The bandgap frequencies are higher compared to the results in reference [7]. This is due to the facts that the real structure of the porous alumina consists of the duplex oxide layers and that the interface between the two oxide layers has a hexagonal shape.

In fact, Masuda *et al.* reported that stopgaps for both polarizations in the porous alumina PCs with  $r/D_{int} = 0.18$  are observed, which are in a good agreement with theoretical predictions assuming a dielectric constant of 2.8 [150]. Note that if we take 2.8 as dielectric constant of the inner oxide and 2.6 as dielectric constant of the outer oxide, the effective dielectric constant of the whole oxide structure is only slightly lower than the value used by Masuda *et al.* [150].

## 7.2.6 Discussion

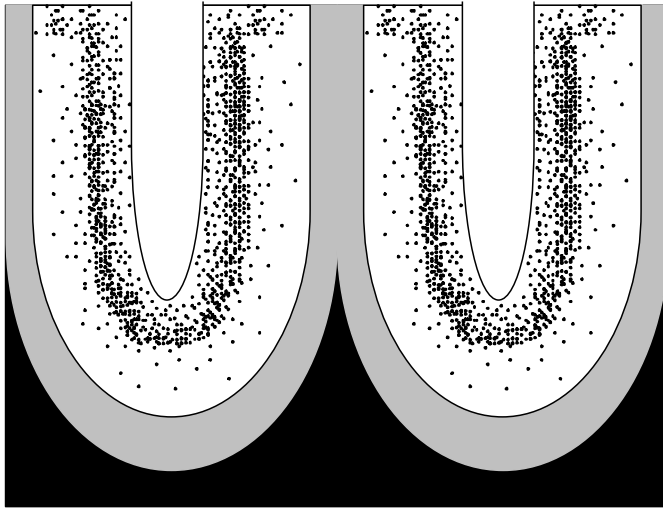


**Figure 7.12:** Schematic diagram of porous alumina oxide layers consisting of inner oxide and outer oxide. Anions (black points) are enriched in the intermediate part of the outer oxide. Note that the inner oxide in the center of the hemispherical scallop of barrier layer is twice as large as that in the edge of hemispherical scallop of the barrier layer or in the wall.

In this section, the reason for the distribution of the effective dielectric constant in the outer oxide layer will be discussed.

The inhomogeneities of the dielectric constant within the outer oxide layer might be explained by the nonuniform distribution of anions in the outer oxide layer. Several possible alumina minerals with different refractive indices could be considered as shown in Table 7.2.

Compared to the dielectric constant of the pure alumina, the anion-incorporated alumina minerals have lower dielectric constants. The more anions are incorporated in the alumina, the lower the dielectric constant. In addition, as the degree of hydrates in the minerals decreases from tri- to mono-, the corresponding refractive index increases. The density of the materials is increased in a similar way, so that the change in the effective dielectric constant can be attributed to a density modification. For example, for both augelite and wavellite containing phosphorus, the refractive index is similar to or smaller than that in hydrated alumina oxides. It is reasonable to assume that anion complexes containing phosphorous are concentrated in the intermediate part (Fig. 7.12). This region corresponds to the minimum dielectric constant in Fig. 7.10. As the anion-contamination decreases towards the inner oxide layer and the outermost oxide layer, the effective dielectric constant for both regions increases. This interpretation

<sup>6</sup>It is the ratio of  $\frac{\Delta\omega}{\omega_0}$ , where  $\Delta\omega = \omega_c - \omega_v$ .  $\omega_v$  and  $\omega_c$  are the lower and upper band edge frequencies of the gap, respectively.  $\omega_0$  is the midgap frequency. This parameter is dimensionless, not depending on the scale of the photonic crystal [149].

**Table 7.2:** Possible alumina minerals with the different refractive indices [70].  $n_\alpha$ ,  $n_\beta$ , and  $n_\gamma$  are the three coordinate axes in the order of least, intermediate, and greatest index.

Name	composition	Refractive index	Density(g/cm <sup>3</sup> )
<b>Wavellite</b>	Al <sub>3</sub> (OH) <sub>3</sub> (PO <sub>4</sub> ) <sub>2</sub> ·5H <sub>2</sub> O	$n_\alpha=1.527$ $n_\beta=1.535$ $n_\gamma=1.553$	2.36
<b>Augelite</b>	Al <sub>2</sub> (PO <sub>4</sub> )(OH) <sub>3</sub>	$n_\alpha=1.574$ $n_\beta=1.576$ $n_\gamma=1.588$	2.70
<b>Gibbsite</b>	$\alpha$ -Al(OH) <sub>3</sub>	$n_\alpha=1.57$ $n_\beta=1.57$ $n_\gamma=1.59$	2.42
<b>Diaspore</b>	$\beta$ -AlO(OH)	$n_\alpha=1.694$ $n_\beta=1.715$ $n_\gamma=1.741$	3.4
<b>Boehmite</b>	$\alpha$ -AlO(OH)	$n_\alpha=1.64$ $n_\beta=1.65$ $n_\gamma=1.66$	3.44
<b>Corundum</b>	$\alpha$ -Al <sub>2</sub> O <sub>3</sub>	$n_\alpha=1.761$ $n_\beta=1.769$	3.97

is in line with a model for the porous alumina structure suggested by Fukuda and Takahashi *et al.* [151, 152, 153, 154]. According to their model, the pore wall of porous alumina consists of an inner oxide layer composed of pure alumina and an outer oxide layer. The outer oxide layer again consists of an outermost oxide part and an intermediate oxide part. Takahashi *et al.* claim that the mobility of PO<sub>4</sub><sup>3-</sup> is responsible for the nonuniform anion concentration [151, 152, 153]. Adsorbed anions, for example, PO<sub>4</sub><sup>3-</sup>, OH<sup>-</sup> and O<sup>2-</sup>, are pulled into the negatively charged electrode by the electric field. Since the size of the phosphorus anion complex is larger than the size of the other anions, the adsorbed PO<sub>4</sub><sup>3-</sup> migrates more slowly compared with OH<sup>-</sup> and O<sup>2-</sup>. The phosphorus anion complex is delayed in the intermediate part since the attracting force in the intermediate part is weaker than that in electrolyte/outermost oxide interface. As a result, PO<sub>4</sub><sup>3-</sup> is concentrated in the intermediate part of the outer wall.

### 7.3 Summary

Porous alumina PCs with different values of  $r/D_{int}$ -ratio were fabricated via nanoindentation and subsequent anodization. The porous alumina structures consisted of an inner oxide layer of pure alumina with 50 nm thickness and an outer oxide layer containing impurities such as incorporated anions.

The reflectivity of the porous alumina PCs with the series of  $r/D_{int}$  ratios (0.18 ~ 0.40) was measured and compared with the corresponding bandstructure calculations. Even though complete photonic bandgaps were not observed due to the low dielectric contrast, photonic stopgaps in both TE-and TM-polarizations in the  $\Gamma$  - M direction were detected in near-infrared regime. In addition, comparison of theory with experiment showed that the outer oxide layer has a non-homogenous dielectric constant depending on the degree of impurity concentration. For example, the  $\epsilon_{\text{eff,outer}}$  varies from 2.6 for  $r/D_{int} = 0.18$ , to 2.4 for  $r/D_{int} = 0.22$ , and to 2.7 for

$r/D_{int} = 0.33$  for the TM mode. It can be concluded that the outer oxide layer consists again of an outermost part and an intermediate part. It was suggested that the phosphorous anion complexes incorporated in the outer oxide layer are enriched in the intermediate part of the outer oxide layer.

## 8. Conclusions

In chapters 1 and 2, the anodization parameters in the self-ordering regimes to obtain the highly-ordered porous alumina structures were discussed in detail. All the self-ordered porous alumina structures exhibit a porosity of 10 % when the conditions such as the applied potential, the type and the concentration of the electrolytes, and temperature match. The 10 % porosity rule is in good agreement with the mechanical stress model [48]. The attainable thickness of porous alumina with straight pore channels is limited due to diffusion limitations in long channels. This can be explained with an deviation from the 10 % porosity rule.

In chapter 3, the preparation of a novel master stamp for nanoindentation of Al and nanoimprint lithography to obtain monodomain porous alumina was discussed. The master stamp consisted of  $\text{Si}_3\text{N}_4$  pyramids with a lattice constant of 500 nm and a height of 260 nm. The hexagonal patterns on the master stamp were well transferred onto the Al under the optimized pressure (5  $\text{kN/cm}^2$ ). Afterwards, monodomain porous alumina with an aspect ratio of  $> 500$  was prepared in the self-ordering regime of 195 V. In addition, effects of impurities of the Al substrate on monodisperse porous alumina was studied. The results showed that a high purity aluminum is required for the fabrication of a monodomain porous alumina membrane.

In chapter 4, the combination of self-assembly and nanoimprint lithography was discussed. The method allows the preparation of various porous alumina structures that are not accessible by other methods. For example, smart nanoimprint lithography that enables the preparation of perfectly ordered porous alumina with 300 nm interpore distance by means of a 500 nm periodic master stamp was discussed. Moreover, nanobranched structures were prepared by a thinning process. It was demonstrated that any kind of highly-ordered branches can be created underneath monodomain porous alumina, if the branches are formed in the self-ordering regimes. Furthermore, Moiré patterns of the porous alumina were obtained by consecutive nanoindentation steps where the orientation of the stamp is altered by rotating it. The distances between fringes in the Moiré patterns were theoretically predicted. In addition, modulations of pore diameter were obtained by alternation of two electrolytes. The limitation of the number of modulation steps is due to the change of the ratio of the inner oxide and the outer oxide. Finally, for integration of porous alumina with Si technologies, monodomain porous alumina was fabricated on a Si wafer.

In chapter 5, anodization of Ti was discussed in order to extend our knowledge of both nanoimprint and self-assembly. The prestructured Ti substrate was anodized using the same methods as discussed in the anodization of Al. Due to the semiconducting properties of titania, self-ordered porous titania could not be prepared. However, by nanoindentation of titanium and successive anodization of titania below the breakdown potential, monodomain porous titanium oxide with a pore depth of 60 nm on a  $\text{cm}^2$ -scale could be prepared.

Chapter 6 deals with the synthesis of Ag nanowires in various alumina templates by electrochemical plating. Nearly 100 % of the pores were filled since the novel thinning process allows to prepare a barrier layer with homogenous thickness of a few nanometers.

In the chapter 7, optical properties of monodomain porous alumina templates were investigated. The reflectivity of porous alumina photonic crystals with different of  $r/D_{int}$  ratios (0.18  $\sim$  0.40)

was measured and compared to corresponding bandstructure calculations. The results demonstrated that photonic stopgaps for both TE- and TM-polarizations in the  $\Gamma - M$  direction exist in the near-infrared regime. It was revealed that the outer oxide layer has a non-homogenous dielectric constant that depends on concentration of anions impurities. The porous alumina structures consist of three layers: the inner layer consisting of pure aluminum oxide, the intermediate part of the outer oxide layer where the phosphorous anion complex is enriched, and the outermost part of the outer oxide layer.

## Schlußfolgerungen

Im Kapitel 1 und 2 wurden die Anodisierungsparameter zum Erhalt hochgeordneter poröser Aluminiumoxidstrukturen mittels Selbstordnung im Detail diskutiert. Die selbstgeordneten porösen Aluminiumoxid-Strukturen weisen eine Porosität von 10 % auf, wenn bestimmte Bedingungen wie angewendetes Potential, Art und Konzentration des Elektrolyten und Temperatur erfüllt werden. Die 10 %-Porositätsregel zeigte eine gute Übereinstimmung mit dem mechanischen Spannung-Modell. Die erreichbaren Dicken des porösen  $\text{Al}_2\text{O}_3$  mit geraden Poren sind aufgrund der Diffusions in langen Poren limitiert. Dies konnte mit einer Abweichung von der 10 % Porositätsregel erklärt werden.

Im Kapitel 3 wurde die Präparation eines Stempels zur (-prägetechnik) Nanoindentation von Al dargestellt um perfekt hexagonal geordneten porösen  $\text{Al}_2\text{O}_3$  zu erhalten. Der Stempel besteht aus  $\text{Si}_3\text{N}_4$  Pyramiden mit einer Gitterkonstante von 500 nm und einer Höhe von 260 nm. Die hexagonale Struktur des Stempels wurde unter einem optimierten Druck ( $5 \text{ kN/cm}^2$ ) sehr gut auf das Al übertragen. Anschließend wurden monodomänige („einkristalline“) poröse  $\text{Al}_2\text{O}_3$ -Schichten mit einem Aspektverhältnis größer 500 im Selbstorganisationsregime bei 195 V hergestellt. Zusätzlich wurde die Auswirkung von Verunreinigungen im Aluminium auf die Herstellung monodispersen porösen  $\text{Al}_2\text{O}_3$  untersucht. Die Ergebnisse zeigten deutlich, daß eine hohe Reinheit des Aluminiums notwendig ist, um monodomäniges poröses Aluminiumoxid herzustellen.

Im Kapitel 4 wurde die Kombination aus Selbstorganisation und Nanoimprintlithographie (NIL) beschrieben. Die Methode ermöglicht die Herstellung verschiedener porösen  $\text{Al}_2\text{O}_3$ -Strukturen, die mit herkömmlichen Methoden nicht zugänglich sind. Zum Beispiel intelligente NIL erlaubt die Präparation von perfekt geordnetem porösen Aluminiumoxides mit 300 nm Porenabstand mittels des 500 nm Stempels. Weiterhin wurden Nanoverzweigungen mit Hilfe eines Abdünnprozesses hergestellt. Es konnte gezeigt werden, daß einige Formen hochgeordneter Verzweigungen unterhalb monodomänigen porösen Aluminiumoxides erzeugt werden können, wenn die Verzweigungen im Selbstordnungsregime gebildet werden. Außerdem konnten durch konsekutive Nanoindentation Moiré Strukturen des porösen Aluminiumoxid erhalten werden, wobei die Orientierung des Stempels durch Rotation geändert wurde. Der Abstand zwischen den Randzonen der Moiré Strukturen wurde theoretisch vorhergesagt. Außerdem konnten beim Wechsel zweier Elektrolyten eine Modulation der Poren erzielt werden. Die Anzahl der Modulationsschritte ist limitiert aufgrund der Änderung des Verhältnisses zwischen innerem und äußerem Oxid. Schließlich konnte monodomäniges poröses Aluminiumoxid auf einem Si-Wafer hergestellt werden, welche dessen Integration mit das Silizium-Technologie verdeutlicht.

Zur Erweiterung unseres Wissens von Nanoimprint und Selbstorganisation wurde im Kapitel 5 die Anodisierung von Titan beschrieben. Die vorstrukturierten Ti-Substrate wurden mittels der gleichen Methode wie im Falle des Aluminiums anodisiert. Aufgrund der halbleitenden Eigenschaften von Titan konnte kein selbstgeordnetes poröses Titandioxid hergestellt werden,

da das Durchbruchpotential unterhalb des benötigten feldunterstützten Auflösungspotentials liegt. Jedoch konnte durch Nanoindentation des Titans und nachfolgender Anodisation unterhalb des Durchbruchpotentials monodomäniges poröses Titandioxid mit einer Porentiefen von 60 nm im  $\text{cm}^2$ -Maßstab präpariert werden.

Im Kapitel 6 wurde die Synthese von Silber-Nanostäben in verschiedenen  $\text{Al}_2\text{O}_3$ -Templaten mittels elektrochemischer Abscheidung beschrieben. Ein neuartiger Abdünnprozess des Barriereoxides mit homogenen Dicken von wenigen Nanometern ermöglichte einen nahezu 100-%igen Füllgrad der Poren.

Im Kapitel 7 wurden die Untersuchungen der optischen Eigenschaften hochgeordneter poröser Aluminiumoxid-Template erläutert. Die Reflektivität von porösen  $\text{Al}_2\text{O}_3$  photonischen Kristallen mit unterschiedlichen  $r/D_{int}$  Verhältnissen ( $0.18 \sim 0.40$ ) wurde gemessen und mit korrespondierenden Bandstrukturberechnungen verglichen. Die Ergebnisse verdeutlichen, daß photonische Stopbänder für beide der TE- und der TM- Polarisation in der-Richtung im nahen Infrarotbereich existieren. Es wurde gezeigt, daß das äußere Oxid eine inhomogene dielektrische Konstante besitzt, die abhängig von der Konzentration der anionischen Verunreinigungen ist. Die poröse  $\text{Al}_2\text{O}_3$ -Struktur besteht aus drei Schichten: dem inneren Oxid bestehend aus reinem Aluminiumoxid, einer Zwischenschicht zugehörig dem äußeren Oxid, in dem komplexe Phosphat-Anionen angereichert sind und dem äußersten Teil dieser Oxidschicht.

## 9. Outlook

In this outlook, the following research ideas are proposed which are based on this dissertation:

1. The smart nanoimprint lithography could be used to obtain porous alumina having extended monodomain pore arrays with lattice constants as small as 65 nm (see the Section 4.1). If a master stamp with 180 nm lattice constant is employed to prepattern the surface of Al, monodomain porous alumina structures with a 100 nm interpore distance ( $\approx 0.6 \times 180$  nm) and a very high aspect ratio could be obtained because the required anodization conditions are in the self-ordering regime of 40 V. In a similar manner, monodomain porous alumina with a 65 nm interpore distance and a very high aspect ratio could be prepared by smart nanoimprint lithography using master stamp with a 110 nm lattice constant.

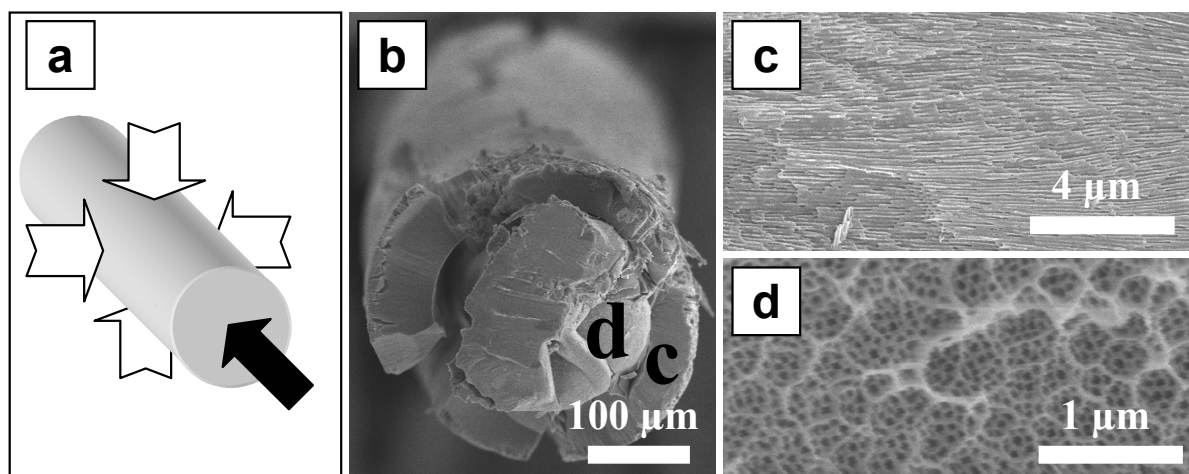


**Figure 9.1:** 3D-porous alumina structures. (a) Schematic diagram of anodization of an Al wire in two different directions. The white arrows and the black arrow indicate the direction of anodization in the first anodization and the third anodization, respectively. After the first anodization, aluminum continues to be anodized with linearly increasing potential from 40 V to 150 V in 0.05 M boric acid to increase the thickness of the barrier layer in the first anodization direction (second anodization). Afterwards, the oxide layer at the facet of the longitudinal direction, which is formed during the first anodization, is removed before the third anodization. (b) SEM image of anodized wires. The areas, marked **c** and **d** in Fig. 9.1 (b), are the layers obtained by the first anodization and by the third anodization, respectively. (c) and (d) show the enlarged view of the areas of **c** and **d** in Fig. 9.1 (b), respectively.

2. Three-dimensional porous alumina structures could be obtained by multi-step anodization in different orientations. For example, Fig. 9.1 (a) shows the feasibility to construct a 3-D porous alumina structure by a 3-step anodization. First, an Al wire with a diameter of 0.5 mm is anodized at all faces in 0.3 M oxalic acid at 40 V. Afterwards, it is anodized with an increasing potential from 40 V to 150 V in 0.05 M boric acid to enhance the thickness of the barrier layer (second anodization). This allows to avoid further anodization in the lateral directions during the third anodization. Then, the oxide layer at the facet of the longitudinal direction is removed. The third anodization under the same conditions as the first anodization is performed in the

longitudinal direction. Figs. 9.1 (b), (c), and (d) show porous alumina structures with different directions of pores [155].

Metal	Oxide	Bandgap, $E_g$	Formation factor, $\Delta d/\Delta U$ (nm/V)
Al	$\text{Al}_2\text{O}_3$	7-9.5	0.75-2
Be	BeO		0.76
Bi	$\text{Bi}_2\text{O}_3$	2.7	
Cu	$\text{Cu}_2\text{O}$	1.8	
	CuO	0.6-0.7	
Hf	$\text{HfO}_2$	5.1	1.8-2.4
Nb	$\text{Nb}_2\text{O}_5$	3.4-5.3	2.1-3.7
Si	$\text{SiO}_2$	9	0.4-0.7
Sn	$\text{SnO}_2$	3.5	1
Ta	$\text{Ta}_2\text{O}_5$	4-4.6	1.3-2.4
Ti	$\text{TiO}_2$	3.2-3.8	1.3-3.3
V	$\text{V}_2\text{O}_5$		6.5
W	$\text{WO}_3$	2.7-3.1	1.8
Zn	ZnO	3.2	
Zr	$\text{ZrO}_2$	4.6-8	1.7-3

**Table 9.1:** Physical properties of metal oxides [88].

3. It is still an open question what kind of materials are also likely to form porous oxide layers having very high aspect ratios by anodization, like Al. The anodization of Ti was already discussed in chapter 6. In the case of Ti, a local field enhancement to nucleate pores is not possible due to the semiconducting properties of Ti ( $3.2 < E_g < 3.8$ ). Table 9.1 shows the physical properties of metal oxides. First, suitable metals should form oxides having a bandgap higher than that of  $\text{TiO}_2$  since an insulating behavior is a prerequisite for a local field enhancement. Secondly, the oxide formation factor should have a moderate value if the self-ordering mechanism relies on the mechanical stress like in the case of the self-ordered porous alumina. For example, zirconia has a high bandgap ranging from 4.6 to 8 and a moderate formation factor of 1.7-3. In addition, silica is an alternative candidate due to its high bandgap [156].

4. It has been suggested that after silver infiltration (see the Section 6.1), monodomain porous alumina could be used as a metallo-dielectric photonic crystal associated with an increase in the width of photonic bandgaps which may be realized. Metallo-dielectric photonic crystals could show photonic bandgaps for the TE mode (H-polarization) in all directions even though the dielectric constant of the pure alumina in the porous alumina structure is as low as 2.8 [134, 157].

# Bibliography

- [1] *Anodic oxidation of aluminum and its alloys*, In *Information Bulletin*, vol. 14. London: The Aluminum development association, 1948.
- [2] C. R. Martin, “Nanomaterials - a membrane-based synthetic approach,” *Science*, vol. **266**, pp. 1961–1966, 1994.
- [3] K. Itaya, S. Sugawara, K. Arai, and S. Saito, “Properties of porous anodic aluminum oxide films as membranes,” *Journal of Chemical Engineering of Japan*, vol. **17**, pp. 514–520, 1984.
- [4] A. T. Shawaqfeh and R. E. Baltus, “Fabrication and characterization of single layer and multi-layer anodic alumina membranes,” *Journal of Membrane Science*, vol. **157**, pp. 147–158, 1999.
- [5] T. Kyotani, W. H. Xu, Y. Yokoyama, J. Inahara, H. Touhara, and A. Tomita, “Chemical modification of carbon-coated anodic alumina films and their application to membrane filter,” *Journal of Membrane Science*, vol. **196**, pp. 231–239, 2002.
- [6] S. Shingubara, “Fabrication of nanomaterials using porous alumina templates,” *Journal of Nanoparticle Research*, vol. **5**, pp. 17–30, 2003.
- [7] R. B. Wehrspohn and J. Schilling, “Electrochemically prepared pore arrays for photonic-crystal applications,” *Materials Research Society Bulletin*, vol. 26, pp. 623–626, 2001.
- [8] G. Sauer, G. Brehm, S. Schneider, K. Nielsch, R. B. Wehrspohn, J. Choi, H. Hofmeister, and U. Gösele, “Highly ordered monocrystalline silver nanowire arrays,” *Journal of Applied Physics*, vol. **2**, pp. 3243–3247, 2002.
- [9] K. Nielsch, F. Müller, A. P. Li, and U. Gösele, “Uniform nickel deposition into ordered alumina pores by pulsed electrodeposition,” *Advanced Materials*, vol. **12**, pp. 582–586, 2000.
- [10] J. Choi, G. Sauer, K. Nielsch, R. B. Wehrspohn, and U. Gösele, “Hexagonally arranged monodisperse silver nanowires with adjustable diameter and high aspect ratio,” *Chemistry of Materials*, vol. **15**, pp. 776–779, 2003.
- [11] M. Steinhart, J. H. Wendorff, A. Greiner, R. B. Wehrspohn, K. Nielsch, J. Schilling, J. Choi, and U. Gösele, “Polymer nanotubes by wetting of ordered porous templates,” *Science*, vol. **296**, pp. 1997–1997, 2002.
- [12] B. B. Lakshmi, P. K. Dorhout, and C. R. Martin, “Sol-gel template synthesis of semiconductor nanostructures,” *Chemistry of Materials*, vol. **9**, pp. 857–862, 1997.
- [13] G. Che, B. B. Lakshmi, C. R. Martin, E. R. Fisher, and R. S. Ruoff, “Chemical vapor deposition based synthesis of carbon nanotubes and nanofibers using a template method,” *Chemistry of Materials*, vol. **10**, pp. 260–267, 1998.
- [14] G. Che, B. B. Lakshmi, E. R. Fisher, and C. R. Martin, “Carbon nanotubule membranes for electrochemical energy storage and production,” *Nature*, vol. **393**, pp. 346–349, 1998.

- [15] P. G. Sheasby and W. E. Cooke, "The electrolytic colouring of anodized aluminum," *Transactions of the Institute of Metal Finishing*, vol. **52**, pp. 103–106, 1974.
- [16] *British Patent 223,994*, 1923.
- [17] *Italian Patent 741,753*, 1936.
- [18] F. Keller, M. S. Hunter, and D. L. Robinson, "Structural features of oxide coatings on aluminum," *Journal of the Electrochemical Society*, vol. **100**, pp. 411–419, 1953.
- [19] J. W. Diggle, T. C. Downie, and C. W. Couling, "Anodic oxide films on aluminum," *Chemical Review*, vol. **69**, pp. 365–405, 1969.
- [20] G. Thompson and G. C. Wood, *Anodic films on aluminum, In treatise on materials science and technology*, vol. 23. New York: Academic Press, 1983.
- [21] G. E. Thompson, Y. Xu, P. Skeldon, K. Shimizu, S. H. Han, and G. C. Wood, "Anodic oxidation of aluminum," *Philosophical Magazine B*, vol. **55**, pp. 651–667, 1987.
- [22] K. Shimizu, K. Kobayashi, G. E. Thompson, and G. C. Wood, "A novel marker for the determination of transport numbers during anodic barrier oxide growth on aluminum," *Philosophical Magazine B*, vol. **64**, pp. 345–353, 1991.
- [23] G. C. Wood, P. Skeldon, G. E. Thompson, and K. Shimizu, "A model for the incorporation of electrolyte species into anodic alumina," *Journal of the Electrochemical Society*, vol. **143**, pp. 74–83, 1996.
- [24] J. P. O'Sullivan and G. C. Wood, "Morphology and mechanism of formation of porous anodic films on aluminium," *Proceedings of the Royal Society of London Series A - Mathematical and Physical Sciences*, vol. **317**, pp. 511–543, 1970.
- [25] T. P. Hoar and N. F. Mott, "A mechanism for the formation of porous anodic oxide films on aluminum," *Journal of Physics and Chemistry of Solids*, vol. **9**, pp. 97–99, 1959.
- [26] V. P. Parkhutik and V. I. Shershulsky, "Theoretical modelling of porous oxide growth on aluminum," *Journal of Physics D - Applied Physics*, vol. **25**, pp. 1258–1263, 1992.
- [27] G. Paternaraki, P. Lenas, C. H. Karavassilis, and G. Papayiannis, "Kinetics of growth of porous anodic Al<sub>2</sub>O<sub>3</sub> films on Al metal," *Electrochimica Acta*, vol. **38**, pp. 709–725, 1991.
- [28] G. Paternaraki and N. Papandreadis, "Study on the kinetics of growth of porous anodic Al<sub>2</sub>O<sub>3</sub> films on Al metal," *Electrochimica Acta*, vol. **38**, pp. 2351–2361, 1993.
- [29] G. Paternaraki and D. Tzouvelekis, "Development of a strict kinetic model for the growth of porous anodic Al<sub>2</sub>O<sub>3</sub> films on Aluminium," *Electrochimica Acta*, vol. **39**, pp. 2419–2429, 1994.
- [30] G. Paternaraki and H. S. Karayannis, "The mechanism of growth of porous anodic Al<sub>2</sub>O<sub>3</sub> films on aluminium at high film thicknesses," *Electrochimica Acta*, vol. **40**, pp. 2647–2656, 1995.
- [31] G. Paternaraki, "Transformation of the overall strict kinetic model governing the growth of porous anodic Al<sub>2</sub>O<sub>3</sub> films on aluminium to a form applicable to the non-stirred bath film growth," *Electrochimica Acta*, vol. **41**, pp. 2601–2611, 1996.
- [32] J. Randon, P. P. Mardilovich, A. N. Govyadinov, and R. Paterson, "Computer-simulation of inorganic membrane morphology. 3. anodic alumina films and membranes," *Journal of Colloid and Interface Science*, vol. **169**, pp. 335–341, 1995.

- [33] S. K. Thamida and H. C. Chang, "Nanoscale pore formation dynamics during aluminum anodization," *Chaos*, vol. **12**, pp. 240–251, 2002.
- [34] H. Masuda and K. Fukuda, "Ordered metal nanohole arrays made by a two-step replication of honeycomb structures of anodic alumina," *Science*, vol. **268**, pp. 1466–1468, 1995.
- [35] H. Masuda, H. Yamada, M. Satoh, H. Asoh, M. Nakao, and T. Tamamura, "Highly ordered nanochannel-array architecture in anodic alumina," *Applied Physics Letters*, vol. **71**, pp. 2770–2772, 1997.
- [36] F. Li, "Nanostructure of anodic porous alumina films of interest in magnetic recording," *The University of Alabama*, 1998.
- [37] P. A. M. E. A. J. Bard), *Encyclopedia of electrochemistry of the elements*, vol. 6. New York and Basel: Marcel Dekker, 1973.
- [38] M. Lohrengel, "Thin anodic oxide layers on aluminum and other valve metals - high-field regime," *Materials Science & Engineering R-Reports*, vol. **11**, pp. 243–294, 1993.
- [39] "<http://webmineral.com/>,"
- [40] G. W. Kabalka and R. M. Pagni, "Organic reactions on alumina," *Tetrahedron*, vol. **53**, pp. 7999–8065, 1997.
- [41] K. Nielsch, J. Choi, K. Schwirn, R. B. Wehrspohn, and U. Gösele, "Self-ordering regimes of porous alumina: The 10% porosity rule," *Nano Letters*, vol. **2**, pp. 677–680, 2002.
- [42] M. S. Hunter and P. Fowle, "Determination of barrier layer thickness of anodic oxide coatings," *Journal of the Electrochemical Society*, vol. **101**, pp. 481–485, 1954.
- [43] M. S. Hunter and P. Fowle, "Factors affecting the formation of anodic oxide coatings," *Journal of the Electrochemical Society*, vol. **101**, pp. 514–519, 1954.
- [44] O. Jessensky, "Untersuchungen zum Porenwachstum in 6H-Siliziumkarbid und anodischem Aluminiumoxid," *Martin-Luther-Universität Halle-Wittenberg*, 1997.
- [45] K. Nielsch, "Hochgeordnete ferromagnetische Nano-Stabensembles: Elektrochemische Herstellung und magnetische Charakterisierung," *Martin-Luther-Universität Halle-Wittenberg*, 2002.
- [46] R. B. Wehrspohn and A. P. Li, K. Nielsch and F. Müller and W. Erfurth and U. Gösele (editors: K. R. Hebert and R. S. Lillard and B. R. Mac Dougall), *Highly ordered alumina films: pore growth and applications (Oxide Films in The Electrochemical Society Proceeding Series)*, vol. PV 2000-4, pp. 271. Pennington, NJ: Marcel Dekker, 2000.
- [47] B. Vanderlinden, H. Terryn, and J. Vereecken, "Investigation of anodic aluminum-oxide layers by electrochemical impedance spectroscopy," *Journal of Applied Electrochemistry*, vol. **20**, pp. 798–803, 1990.
- [48] O. Jessensky, F. Müller, and U. Gösele, "Self-organized formation of hexagonal pore arrays in anodic alumina," *Applied Physics Letters*, vol. **72**, pp. 1173–1175, 1998.
- [49] O. Jessensky, F. Müller, and U. Gösele, "Self-organized formation of hexagonal pore structures in anodic alumina," *Journal of the Electrochemical Society*, vol. **145**, pp. 3735–3740, 1998.

- [50] H. Masuda, F. Hasegawa, and S. Ono, "Self-ordering of cell arrangement of anodic porous alumina formed in sulfuric acid solution," *Journal of the Electrochemical Society*, vol. **144**, pp. L 127–L 130, 1997.
- [51] H. Masuda, K. Yada, and A. Osaka, "Self-ordering of cell configuration of anodic porous alumina with large-size pores in phosphoric acid solution," *Japanese Journal of Applied Physics Part 2-Letters*, vol. **37**, pp. L1340–L1342, 1998.
- [52] A. P. Li, F. Müller, A. Birner, K. Nielsch, and U. Gösele, "Hexagonal pore arrays with a 50-420 nm interpore distance formed by self-organization in anodic alumina," *Journal of Applied Physics*, vol. **84**, pp. 6023–6026, 1998.
- [53] G. C. Schwartz and V. Platter, "Anodic process for forming planar interconnection metalization for multilevel LSI," *Journal of the Electrochemical Society*, vol. **122**, pp. 1508–1516, 1975.
- [54] F. Li, L. Zhang, and R. M. Metzger, "On the growth of highly ordered pores in anodized aluminum oxide," *Chemistry of Materials*, vol. **10**, pp. 2470–2480, 1998.
- [55] S. Y. Chou, P. R. Krauss, and P. J. Renstrom, "Imprint of sub-25 nm vias and trenches in polymers," *Applied Physics Letters*, vol. **67**, pp. 3114–3116, 1995.
- [56] S. Y. Chou, P. R. Krauss, and P. J. Renstrom, "Imprint lithography with 25-nanometer resolution," *Science*, vol. **272**, pp. 85–87, 1996.
- [57] S. Y. Chou, P. R. Krauss, and P. J. Renstrom, "Nanoimprint lithography," *Journal of Vacuum Science & Technology B*, vol. **14**, pp. 4129–4133, 1996.
- [58] S. W. Pang, T. Tamamura, M. Nakao, A. Ozawa, and H. Masuda, "Direct nano-printing on Al substrate using a SiC mold," *Journal of Vacuum Science & Technology B*, vol. **16**, pp. 1145–1149, 1998.
- [59] H. Masuda, H. Asoh, M. Watanabe, K. Nishio, M. Nakao, and T. Tamamura, "Square and triangular nanohole array architectures in anodic alumina," *Advanced Materials*, vol. **13**, pp. 189–192, 2001.
- [60] H. Masuda, M. Yotsuya, M. Asano, K. Nishio, M. Nakao, A. Yokoo, and T. Tamamura, "Self-repair of ordered pattern of nanometer dimensions based on self-compensation properties of anodic porous alumina," *Applied Physics Letters*, vol. **78**, pp. 826–828, 2001.
- [61] A. P. Li, F. Müller, and U. Gösele, "Polycrystalline and monocrystalline pore arrays with large interpore distance in anodic alumina," *Electrochemical & Solid-State Letters*, vol. **3**, pp. 131–134, 2000.
- [62] C. Y. Liu, A. Datta, and Y. L. Wang, "Ordered anodic alumina nanochannels on focused-ion-beam-prepatterned aluminum surfaces," *Applied Physics Letters*, vol. **78**, pp. 120–122, 2001.
- [63] I. Mikulskas, S. Juodkazis, R. Tomasiunas, and J. G. Dumas, "Aluminum oxide photonic crystals grown by a new hybrid method," *Advanced Materials*, vol. **13**, pp. 1574–1577, 2001.
- [64] Z. J. Sun and H. K. Kim, "Growth of ordered, single-domain, alumina nanopore arrays with holographically patterned aluminum films," *Applied Physics Letters*, vol. **81**, pp. 3458–3460, 2002.

- [65] H. Asoh, K. Nishio, M. Nakao, T. Tamamura, and H. Masuda, "Conditions for fabrication of ideally ordered anodic porous alumina using pretextured Al," *Journal of the Electrochemical Society*, vol. **148**, pp. B152–B156, 2001.
- [66] J. Choi, J. Schilling, K. Nielsch, R. Hillebrand, M. Reiche, R. B. Wehrspohn, and U. Gösele, "Large-area porous alumina photonic crystals via imprint method," *Materials Research Society Symposium Proceedings*, vol. **722**, pp. 417–422, 2002.
- [67] A. Jagminas, D. Bigeliene, I. Mikulskas, and R. Tomasiunas, "Growth peculiarities of aluminum anodic oxide at high voltages in diluted phosphoric acid," *Journal of Crystal Growth*, vol. **233**, pp. 591–598, 2001.
- [68] "<http://www.advent-rm.com/>,"
- [69] W. D. Mackintosh, F. Brown, and H. H. Plattner, "Mobility of metallic foreign atoms during the anodic oxidation of aluminum," *Journal of the Electrochemical Society*, vol. **121**, pp. 1281–1286, 1974.
- [70] D. R. Lide, *76th edition*, In *CRC handbook of chemistry and physics*.
- [71] J. Choi, K. Nielsch, M. Reiche, R. B. Wehrspohn, and U. Gösele, "Fabrication of monodomain alumina pore arrays with an interpore distance smaller than the lattice constant of the imprint stamp," *Journal of Vacuum Science & Technology B*, vol. **21**, pp. 763–766, 2003.
- [72] H. Asoh, K. Nishio, M. Nakao, A. Yokoo, T. Tamamura, and H. Masuda, "Fabrication of ideally ordered anodic porous alumina with 63 nm hole periodicity using sulfuric acid," *Journal of Vacuum Science & Technology B*, vol. **19**, pp. 569–572, 2001.
- [73] J. P. Zou, L. Pu, X. M. Bao, and D. Feng, "Branchy alumina nanotubes," *Applied Physics Letters*, vol. **80**, pp. 1079–1081, 2002.
- [74] D. W. Gong, V. Yadavalli, M. Paulose, M. Pishko, and C. A. Grimes, "Controlled molecular release using nanoporous alumina capsules," *Biomedical Microdevices*, vol. **5**, pp. 75–80, 2003.
- [75] D. Crouse, Y. H. Lo, A. E. Miller, and M. Crouse, "Self-ordered pore structure of anodized aluminum on silicon and pattern transfer," *Applied Physics Letters*, vol. **76**, pp. 49–51, 2000.
- [76] S. Z. Chu, K. Wada, S. Inoue, and S. Todoroki, "Formation and microstructures of anodic alumina films from aluminum sputtered on glass substrate," *Journal of the Electrochemical Society*, vol. **149**, pp. B321–B327, 2002.
- [77] S. Z. Chu, K. Wada, S. Inoue, S. Todoroki, Y. K. Takahashi, and K. Hono, "Fabrication and characteristics of ordered Ni nanostructures on glass by anodization and direct current electrodeposition," *Chemistry of Materials*, vol. **14**, pp. 4595–4602, 2002.
- [78] H. Masuda, K. Yasui, Y. Sakamoto, M. Nakao, T. Tamamura, and K. Nishio, "Ideally ordered anodic porous alumina mask prepared by imprinting of vacuum-evaporated Al on Si," *Japanese Journal of Applied Physics Part 2-Letters*, vol. **40**, pp. L1267–L1269, 2001.
- [79] J. Choi, G. Sauer, P. Göring, K. Nielsch, R. B. Wehrspohn, and U. Gösele, "Monodisperse metal nanowire arrays on si by integration of template synthesis with silicon technology," *Journal of Materials Chemistry*, vol. **13**, pp. 1100–1103, 2003.

- [80] Y. Yang, H. L. Chen, Y. F. Mei, J. B. Chen, X. L. Wu, and X. M. Bao, "Anodic alumina template on Au/Si substrate and preparation of CdS nanowires," *Solid State Communications*, vol. **123**, pp. 279–282, 2002.
- [81] G. Oster, C. Zwerling, and M. Wasserman, "Oretical interpretation of Moiré patterns," *Journal of the Optical Society of America*, vol. **54**, pp. 169–175, 1964.
- [82] M. Li, J. Wang, L. Zhuang, and S. Y. Chou, "Fabrication of circular optical structures with a 20 nm minimum feature size using nanoimprint lithography," *Applied Physics Letters*, vol. **76**, pp. 673–675, 2000.
- [83] J. A. Rogers, K. E. Paul, and G. M. Whitesides, "Quantifying distortions in soft lithography," *Journal of Vacuum Science & Technology B*, vol. **16**, pp. 88–97, 1998.
- [84] N. G. Semaltianos, K. Scott, and E. G. Wilson, "Electron beam lithography of Moiré patterns," *Microelectronic Engineering*, vol. **56**, pp. 233–239, 2001.
- [85] M. E. Zoorob, M. D. B. Charlton, G. J. Parker, J. J. Baumberg, and M. C. Netti, "Complete photonic bandgaps in 12-fold symmetric quasicrystals," *Nature*, vol. **404**, pp. 740–743, 2000.
- [86] G. M. Whitesides, E. Ostuni, S. Takayama, X. Y. Jiang, and D. E. Ingber, "Soft lithography in biology and biochemistry," *Annual Review of Biomedical Engineering*, vol. **3**, pp. 335–373, 2001.
- [87] J. Schilling, F. Müller, S. Matthias, R. B. Wehrspohn, U. Gösele, and K. Busch, "Three-dimensional photonic crystals based on macroporous silicon with modulated pore diameter," *Applied Physics Letters*, vol. **78**, pp. 1180–1182, 2001.
- [88] J. W. Schultze and M. M. Lohrengel, "Stability, reactivity and breakdown of passive films. problems of recent and future research," *Electrochimica Acta*, vol. **45**, pp. 2499–2513, 2000.
- [89] A. Aladjem, "Anodic oxidation of titanium and its alloys," *Journal of Materials Science*, vol. **8**, pp. 688–704, 1973.
- [90] R. Asahi, T. Morikawa, T. Ohwaki, K. Aoki, and Y. Taga, "Visible-light photocatalysis in nitrogen-doped titanium oxides," *Science*, vol. **293**, pp. 269–271, 2001.
- [91] T. Albrektsson, P. I. Branemark, H. A. Hansson, and J. Lindstrom, "Osseointegrated titanium implants - requirements for ensuring a long-lasting, direct bone-to-implant anchorage in man," *Acta Orthopaedica Scandinavica*, vol. **52**, pp. 155–170, 1981.
- [92] H. M. Kim, F. Miyaji, K. T. and T. Nakamura, "Preparation of bioactive Ti and its alloys via simple chemical surface treatment," *Journal of Biomedical Materials Research*, vol. **32**, pp. 409–417, 1996.
- [93] V. Zwillling, E. Darque-Ceretti, A. Boutry-Forveille, D. David, M. Y. Perrin, and M. Aucouturier, "Structure and physicochemistry of anodic oxide films on titanium and TA6V alloy," *Surface and Interface Analysis*, vol. **27**, pp. 629–637, 1999.
- [94] D. Gong, C. A. Grimes, O. K. Varghese, W. C. Hu, R. S. Singh, Z. Chen, and E. C. Dickey, "Titanium oxide nanotube arrays prepared by anodic oxidation," *Journal of Materials Research*, vol. **16**, pp. 3331–3334, 2001.
- [95] R. Beranek, H. Hildebrand, and P. Schmuki, "Self-organized porous titanium oxide prepared in H<sub>2</sub>SO<sub>4</sub>/HF electrolytes," *Electrochemical and Solid State Letters*, vol. **6**, pp. B12–B14, 2003.

- [96] “<http://http://www.matweb.com/>,”
- [97] T. Shibata and Y. C. Zhu, “The effect of temperature on the growth of anodic oxide film on titanium,” *Corrosion Science*, vol. **37**, pp. 133–144, 1995.
- [98] J. L. Delplancke and R. Winand, “Galvanostatic anodization of titanium. 1 structures and compositions of the anodic films,” *Electrochimica Acta*, vol. **33**, pp. 1539–1549, 1988.
- [99] C. E. B. Marino, E. M. de Oliveira, R. C. Rocha-Filho, and S. R. Biaggio, “On the stability of thin-anodic-oxide films of titanium in acid phosphoric media,” *Corrosion Science*, vol. **43**, pp. 1465–1476, 2001.
- [100] H. Tang, K. Prasad, R. Sanjinbs, P. E. Schmid, and F. Lévy, “Electrical And Optical-Properties of TiO<sub>2</sub> Anatase Thin-Films,” *Journal of Applied Physics*, vol. **75**, pp. 2042–2047, 1994.
- [101] J. L. Delplancke, A. Garnier, Y. Massiani, and R. Winand, “Influence of the anodizing procedure on the structure and the properties of titanium-oxide films and its effect on copper nucleation,” *Electrochimica Acta*, vol. **39**, pp. 1281–1289, 1994.
- [102] L. Arsov, M. Froelicher, M. Froment, and A. H.-L. Goff, “Anodic-oxidation of titanium in sulfuric solution - nature, thickness and refractive-index of films,” *Journal de Chimie Physique et de Physico-Chimie Biologique*, vol. **72**, pp. 275–279, 1975.
- [103] G. Blondeau, M. Froelicher, M. Froment, and A. H.-L. Goff, “Anodic-oxidation of titanium in sulfuric solution - nature, thickness and refractive-index of films,” *Thin Solid Films*, vol. **42**, pp. 147–153, 1977.
- [104] J. Yahalom and J. Zahavi, “Electrolytic breakdown crystallization of anodic oxide films on Al, Ta and Ti,” *Electrochimica Acta*, vol. **15**, pp. 1429–1435, 1970.
- [105] J. F. MaAleer and L. M. Peter, “Instability of anodic oxide films on titanium,” *Journal of the Electrochemical Society*, vol. **129**, pp. 1252–1260, 1982.
- [106] J. Choi, K. H. Lee, and Y. Tak, “Interpretation of potential transients during aluminum etch tunnel growth in the presence of sulfuric acid,” *Electrochemistry*, vol. **129**, pp. 843–847, 2001.
- [107] R. S. Alwitt, H. Uchi, T. R. Beck, and R. C. Alkire, “Electrochemical tunnel etching of aluminum,” *Journal of the Electrochemical Society*, vol. **131**, pp. 13–17, 1984.
- [108] M. Kozlowski, W. H. Smyrl, L. J. Atanasoka, , and R. Atanasoki, “Local film thickness and photoresponse of thin anodic TiO<sub>2</sub> films on polycrystalline titanium,” *Electrochimica Acta*, vol. **34**, pp. 1763–1768, 1989.
- [109] Y. Lei and L. D. Zhang, “Fabrication, characterization, and photoluminescence properties of highly ordered TiO<sub>2</sub> nanowire arrays,” *Journal of Materials Research*, vol. **16**, pp. 1138–1144, 2001.
- [110] Y. Lei, L. D. Zhang, G. W. Meng, G. H. Li, X. Y. Zhang, C. H. Liang, W. Chen, and S. X. Wang, “Preparation and photoluminescence of highly ordered TiO<sub>2</sub> nanowire arrays,” *Applied Physics Letters*, vol. **78**, pp. 1125–1127, 2001.
- [111] Z. Miao, D. S. Xu, J. H. Ouyang, G. L. Guo, X. S. Zhao, and Y. Q. Tang, “Electrochemically induced sol-gel preparation of single-crystalline TiO<sub>2</sub> nanowires,” *Nano Letters*, vol. **2**, pp. 717–720, 2002.
- [112] J. Li, C. Papadopoulos, J. M. Xu, and M. M. M, “Highly-ordered carbon nanotube arrays for electronics applications,” *Applied Physics Letters*, vol. **75**, pp. 367–369, 1999.

- [113] N. I. Kovtyukhova, T. E. Mallouk, and T. S. Mayer, "Templated surface sol-gel synthesis of SiO<sub>2</sub> nanotubes and SiO<sub>2</sub>-insulated metal nanowires," *Advanced Materials*, vol. **15**, pp. 780–785, 2003.
- [114] H. Q. Cao, Y. Xu, J. M. Hong, H. B. Liu, G. Yin, B. L. Li, C. Y. Tie, and Z. Xu, "Sol-gel template synthesis of an array of single crystal CdS nanowires on a porous alumina template," *Advanced Materials*, vol. **13**, pp. 1393–1394, 2001.
- [115] H. Q. Cao, Y. Xu, X. W. Wei, X. Ma, and Z. L. Xue, "Sol-gel synthesis of an array of C-70 single crystal nanowires in a porous alumina template," *Chemical Communications*, pp. 541–542, 2001.
- [116] B. Cheng and E. T. Samulski, "Fabrication and characterization of nanotubular semiconductor oxides In<sub>2</sub>O<sub>3</sub> and Ga<sub>2</sub>O<sub>3</sub>," *Journal of Materials Chemistry*, vol. **11**, pp. 2901–2902, 2001.
- [117] J. D. Klein, R. D. Herrick, D. Palmer, M. J. Sailor, C. J. Brumlik, and C. R. Martin, "Electrochemical fabrication of cadmium chalcogenide microdiode arrays," *Chemistry of Materials*, vol. **5**, pp. 902–904, 1993.
- [118] S. Shingubara, O. Okino, Y. Sayama, H. Sakaue, and T. Takahagi, "Ordered two-dimensional nanowire array formation using self-organized nanoholes of anodically oxidized aluminum," *Japanese Journal of Applied Physics Part 1-Regular Papers Short Notes & Review Papers*, vol. **36**, pp. 7791–7795, 1997.
- [119] G. J. Strijkers, J. H. J. Dalderop, M. A. A. Broeksteeg, H. J. M. Swagten, and W. J. M. de Jonge, "Structure and magnetization of arrays of electrodeposited Co wires in anodic alumina," *Journal of Applied Physics*, vol. **86**, pp. 5141–5145, 1999.
- [120] L. Menon, S. Bandyopadhyay, Y. Liu, H. Zeng, and D. J. Sellmyer, "Magnetic and structural properties of electrochemically self-assembled Fe<sub>1-x</sub>Co<sub>x</sub> nanowires," *Journal of Nanoscience and Nanotechnology*, vol. **1**, pp. 149–152, 2001.
- [121] Y. T. Pang, G. W. Meng, Y. Zhang, Y. Qin, X. Y. Gao, A. W. Zhao, and Q. Fang, "Arrays of ordered Pb nanowires and their optical properties for laminated polarizers," *Advanced Functional Materials*, vol. **12**, pp. 719–722, 2002.
- [122] Y. T. Pang, G. W. Meng, Y. Zhang, Q. Fang, and L. D. Zhang, "Copper nanowire arrays for infrared polarizer," *Applied Physics A-Materials Science & Processing*, vol. **76**, pp. 533–536, 2003.
- [123] Y. J. Glanville, D. G. Narehood, P. E. S. PE, A. Amma, and T. Mallouk, "Preparation and synthesis of Ag<sub>2</sub>Se nanowires produced by template directed synthesis," *Journal of Materials Chemistry*, vol. **12**, pp. 2433–2434, 2002.
- [124] M. Martín-González, A. L. Prieto, R. Gronsky, T. Sands, and A. M. Stacy, "High-Density 40 nm Diameter Sb-Rich Bi<sub>2-x</sub>Sb<sub>x</sub>Te<sub>3</sub> Nanowire Arrays," *Advanced Materials*, vol. **15**, pp. 1003–1006, 2003.
- [125] V. P. Menon and C. R. Martin, "Fabrication and evaluation of nanoelectrode ensembles," *Analytical Chemistry*, vol. **67**, pp. 1920–1928, 1995.
- [126] A. W. Li, W. Q. Liang, and R. Hughes, "Fabrication of dense palladium composite membranes for hydrogen separation," *Catalysis Today*, vol. **56**, pp. 45–51, 2000.
- [127] M. Kajiwara, S. Uemiya, T. Kojima, and E. Kikuchi, "Rhodium- and iridium-dispersed porous alumina membranes and their hydrogen permeation properties," *Catalysis Today*, vol. **56**, pp. 83–87, 2000.

- [128] J. Zhang, L. D. Zhang, X. F. Wang, C. H. Liang, X. S. Peng, and Y. W. Wang, "Fabrication and photoluminescence of ordered GaN nanowire arrays," *Journal of Chemical Physics*, vol. **115**, pp. 5714–5717, 2001.
- [129] J. B. Bai, "Growth of nanotube/nanofibre coils by CVD on an alumina substrate," *Materials Letters*, vol. **57**, pp. 2629–2633, 2003.
- [130] R. M. Dickson and L. A. Lyon, "Unidirectional plasmon propagation in metallic nanowires," *Journal of Physical Chemistry B*, vol. **104**, pp. 6095–6098, 2000.
- [131] S. R. Nicewarner-Peña and R. G. Freeman and B. D. Reiss and L. He and D. J. Peña and I. D. Walton and R. Cromer and C. D. Keating and M. J. Natan, "Submicrometer metallic barcodes," *Science*, vol. **294**, pp. 137–141, 2001.
- [132] G. Schider, J. R. Krenn, W. Gotschy, B. Lamprecht, H. Ditlbacher, A. Leitner, and F. R. Aussenegg, "Optical properties of Ag and Au nanowire gratings," *Journal of Applied Physics*, vol. **90**, pp. 3825–3830, 2001.
- [133] "<http://www.technic.com/>,"
- [134] H. van der Lem and A. Moroz, "Towards two-dimensional complete photonic bandgap structures below infrared wavelengths," *Journal of Optics A-Pure and Applied Optics*, vol. **2**, pp. 395–399, 2000.
- [135] J. D. Joannopoulos, R. D. Meade, and J. N. Winn, *Photonic Crystals*. New Jersey: Princeton University Press, 1995.
- [136] A. Birner, R. B. Wehrspohn, U. Gösele, and K. Busch, "Silicon-based photonic crystals," *Advanced Materials*, vol. **13**, pp. 377–388, 2001.
- [137] Y. N. Xia, B. Gates, Y. D. Yin, and Y. Lu, "Monodispersed Colloidal Spheres: Old Materials with New Applications," *Advanced Materials*, vol. **12**, pp. 693–713, 2000.
- [138] Y. N. Xia, B. Gates, and Z. Y. Lu, "Self-assembly approaches to three-dimensional photonic crystals," *Advanced Materials*, vol. **15**, pp. 409–413, 2001.
- [139] D. J. Norris and Y. A. Vlasov, "Chemical approaches to three-dimensional semiconductor photonic crystals," *Advanced Materials*, vol. **15**, pp. 371–376, 2001.
- [140] K. M. Ho, C. T. Chan, C. M. Soukoulis, R. Biswas, and M. Sigalas, "Photonic bandgaps in three dimensions: new layer-by-layer structures," *Solid State Communications*, vol. **89**, pp. 413–416, 1994.
- [141] G. E. Thompson and G. C. Wood, "Porous anodic film formation on aluminum," *Nature*, vol. **290**, pp. 230–232, 1981.
- [142] F. L. Pedrotti and L. S. Pedrotti, *Introduction to optics*. New Jersey: Prentice Hall, 1993.
- [143] "<http://ab-initio.mit.edu/mpb/>," *The MIT photonic-bands (MPB) package*, S. G. Johnson, MIT.
- [144] "<http://userweb.elec.gla.ac.uk/a/areynolds/>," *Translight package*, A. L. Reynolds, University of Glasgow.
- [145] H. Takahashi, K. Fujimoto, H. Konno, and M. Nagayama, "Distribution of anions and protons in oxide-films formed anodically on aluminum in a phosphate solution," *Journal of the Electrochemical Society*, vol. **131**, pp. 1856–1861, 1984.
- [146] K. Huber, "Pore volume of electrolytically produced protective coatings on aluminum," *Journal of Colloid Science*, vol. **3**, pp. 197–206, 1948.

- [147] G. Hass, “On the preparation of hard oxide films with precisely controlled thickness on evaporated aluminum mirrors,” *Journal of the Optical Society of America*, vol. **39**, pp. 532–540, 1949.
- [148] S. Nakamura, M. Saito, L.-F. Huang, M. Miyagi, and K. Wada, “Infrared optical-constants of anodic alumina films with micropore arrays,” *Japanese Journal of Applied Physics Part 1-Regular Papers Short Notes & Review Papers*, vol. **39**, pp. 3589–3593, 1992.
- [149] M. Woldeyohannes and S. John, “Coherent control of spontaneous emission near a photonic band edge,” *Journal of Optics B - Quantum and Semiclassical Optics*, vol. **5**, pp. R43–R82, 2003.
- [150] H. Masuda, M. Ohya, K. Nishio, H. Asoh, M. Nakao, M. Nohtomi, A. Yokoo, and T. Tamamura, “Photonic band gap in anodic porous alumina with extremely high aspect ratio formed in phosphoric acid solution,” *Japanese Journal of Applied Physics Part 2-Letters*, vol. **39**, pp. L1039–L1041, 2000.
- [151] Y. Fukuda, “Role of oxalate ion in formation of oxide film of aluminum in oxalic-acid electrolyte,” *Nippon Kagaku Kaishi*, pp. 3589–3593, 1974.
- [152] Y. Fukuda, “Role of oxalate ion in formation of oxide film of aluminum in oxalic-acid electrolyte,” *Transactions of National Research Institute for Metals*, vol. **17**, p. 25, 1975.
- [153] H. Takahashi and M. Nagayama, “Distribution of phosphate ions in porous anodic oxide film formed on aluminum in phosphoric-acid solution,” *Nippon Kagaku Kaishi*, pp. 453–458, 1974.
- [154] S. Ono, H. Ichinose, and N. Masuko, “The high-resolution observation of porous anodic films formed on aluminum in phosphoric-acid solution,” *Corrosion Science*, vol. **33**, pp. 841–850, 1992.
- [155] J. Choi et al., Max-Planck-Institute in Halle, Germany, *Unpublished results (The idea is based on the proposal by Prof. A. Scherer at the Caltech, USA)*.
- [156] M. Lharch, J. N. Chazalviel, F. Ozanam, M. Aggour, and R. B. Wehrspohn, “In situ investigation of porous anodic films of silica,” *Physica Status Solidi A-Applied Research*, vol. **197**, pp. 39–45, 2003.
- [157] V. Poborchii, T. Tada, T. Kanayama, and A. Moroz, “Silver-coated silicon pillar photonic crystals: Enhancement of a photonic band gap,” *Applied Physics Letters*, vol. **82**, pp. 508–510, 2003.

# Curriculum vitae

First Name	Jinsub
Family Name	Choi
Date of Birth	June 30, 1974 (Seoul)
Nationality	South Korean
E-mail	<i>jchoi@mpi-halle.de</i> or <i>solar-sub@hanmail.net</i>

---

## EDUCATION

<i>Oct. 2000 - present</i>	Max Planck Institute of Microstructure Physics and Martin-Luther-University Halle Wittenberg (Halle, Germany) Ph.D. candidate (Supervisors: Prof. Ulrich Gösele and Prof. Ralf B. Wehrspohn)
<i>Mar. 1997 - Feb. 1999</i>	Inha University (Inchoen, Korea) M.S. in Chemical Engineering (Supervisor: Prof. Yongsug Tak) Thesis: Effects of sulfuric acid on the electrochemical tunnel etching of aluminum
<i>Mar. 1993 - Feb. 1997</i>	Inha University (Inchoen, Korea) B.S. in Chemical Engineering

---

## PROFESSIONAL EXPERIENCE

<i>Mar. 1999 - Feb. 2000</i>	Daewon Science College (Chechoen, Korea) Lecturer in Dept. of Environmental Engineering
<i>Jul.-Aug. 1997</i>	Samsung Electro-Mechanics Company (Suwon, Korea) Internship in Materials Laboratory (Electrochemical etching of aluminum)

---

## AWARDS & FELLOWSHIPS

<i>Apr. 2002</i>	Poster Session Award, 2002 MRS spring meeting, San Francisco, USA.
<i>Oct. 2000 - present</i>	Max-Planck-Institute Scholarship, MPI Halle, Germany.
<i>1998</i>	Poster Session Award, The Korea Electrochemical Society Fall Meeting, Seoul.
<i>Mar. 1997 - Feb. 1999</i>	Graduate Research Assistantship, Inha Univ, Korea.
<i>1997</i>	Poster Session Award, The Corrosion Society of Korea Fall Meeting, Seoul.

## List of publications

1. **J. Choi**, R. B. Wehrspohn, J. Lee, and U. Gösele, "Anodization of nanoimprinted titanium: A comparison with formation of porous alumina," *Electrochimica Acta*, revision (2004).
2. C. Harnagea, M. Alexe, J. Schilling, **J. Choi**, R. B. Wehrspohn, D. Hesse, and U. Gösele, "Mesoscopic ferroelectric cell arrays prepared by imprint lithography," *Applied Physics Letters*, vol. **83**, pp. 1827-1829, 2003.
3. **J. Choi**, R. B. Wehrspohn, and U. Gösele, "Moiré pattern formation on porous alumina arrays using nanoimprint lithography," *Advanced Materials*, vol. **15**, pp. 1531-1534, 2003.
4. **J. Choi**, Y. Luo, R. B. Wehrspohn, R. Hillebrand, J. Schilling, and U. Gösele, "Perfect 2D porous alumina photonic crystals with duplex oxide layers," *Journal of Applied Physics*, vol. **94**, pp. 4757-4762, 2003.
5. **J. Choi**, G. Sauer, P. Göring, K. Nielsch, R. B. Wehrspohn, and U. Gösele, "Monodisperse metal nanowire arrays on Si by integration of template synthesis with silicon technology," *Journal of Materials Chemistry*, vol. **13**, pp. 1100-1103, 2003.
6. **J. Choi**, G. Sauer, K. Nielsch, R. B. Wehrspohn, and U. Gösele, "Silver infiltration into monodomain porous alumina with adjustable pore diameter and with high aspect ratio," *Chemistry of Materials*, vol. **15**, pp. 776-779, 2003.
7. **J. Choi**, K. Nielsch, M. Reiche, R. B. Wehrspohn, and U. Gösele, "Fabrication of monodomain alumina pore arrays with an interpore distance smaller than the lattice constant of the imprint stamp," *Journal of Vacuum and Science Technology B*, vol. **21**, pp. 763-766, 2003.
8. M. Steinhart, J. H. Wendorff, A. Greiner, R. B. Wehrspohn, K. Nielsch, J. Schilling, **J. Choi**, and U. Gösele, "Polymer nanotubes by wetting of ordered porous templates," *Science*, vol. **296**, pp. 1997 (2002).
9. K. Nielsch, **J. Choi**, K. Schwirn, R. B. Wehrspohn, and U. Gösele, "Self-ordering regimes of porous alumina: The 10% porosity rule," *Nano Letters*, vol. **2**, pp. 677-680, 2002.
10. **J. Choi**, J. Schilling, K. Nielsch, R. Hillebrand, M. Reiche, R. B. Wehrspohn, and U. Gösele, "Large-area Porous alumina photonic crystals via imprint method," *Mat. Res. Soc. Symp. Proc.* vol. **722**, pp. L 5.2, 2002.
11. G. Sauer, G. Brehm, S. Schneider, K. Nielsch, R.B. Wehrspohn, **J. Choi**, H. Hofmeister, and U. Gösele, "Highly ordered monocrystalline silver nanowire arrays," *Journal of Applied Physics*, vol. **91**, pp. 3243-3247, 2002.
12. **J. Choi**, K. H. Lee, and Y. Tak, "Interpretation of potential transients during aluminum etch tunnel growth in the presence of sulfuric acid," *Electrochemistry*, vol. **69**, pp. 843-847, 2001.

## List of presentations (selection)

1. **J. Choi**, G. Sauer, K. Nielsch, R. B. Wehrspohn, and U. Gösele, "Fabrication of monodisperse silver nanowires with hierarchically ordered branches," *Euromat 2003*, Lausanne, Switzerland, September 01-05, 2003, Talk.
2. **J. Choi**, R. B. Wehrspohn, U. Gösele, and J. Lee, "Towards porous titania," *203rd The Electrochemical Society Meeting*, Paris, France, April 27-May 2, 2003, Poster.
3. **J. Choi**, "Towards porous titania : A comparison of Al anodization," *École Polytechnique*, Palaiseau Cedex, France, April 25, 2003, Talk.
4. **J. Choi**, G. Sauer, K. Nielsch, R. B. Wehrspohn, and U. Gösele, "Fabrication of monodisperse silver nanowires embedded in monodomain porous alumina templates on a cm-scale," *Materials Research Society Spring Meeting 2003, Symposium J: Self-Assembled Nanostructured Materials*, San Francisco, USA, April 21-25, 2003, Poster.
5. **J. Choi**, Y. Luo, R. B. Wehrspohn, R. Hillebrand, J. Schilling, and U. Gösele, "Synthesis of dielectric and metallo-dielectric photonic crystals based on porous alumina with adjustable ratios of radius to interpore distance," *Materials Research Society Spring Meeting 2003, Symposium J: Microphotonics, Nanophotonics, and Photonic Crystals*, San Francisco, USA, April 21-25, 2003, Poster.
6. **J. Choi**, K. Nielsch, R. B. Wehrspohn, and U. Gösele, "From self-assembly towards imprint lithography: Fabrication of highly-ordered porous alumina structures," *53rd Annual Meeting of the International Society of Electrochemistry*, Düsseldorf, Germany, September 15-20, 2002, Poster.
7. **J. Choi**, J. Schilling, K. Nielsch, R. Hillebrand, M. Reiche, R. B. Wehrspohn, and U. Gösele, "Large-area Porous alumina photonic crystals via imprint method," *Third Wilhelm and Else Heraeus Summer School, Photonic Crystals: Optical Materials for the 21st Century*, Wittenberg, Germany, July 14-25, 2002, Poster.
8. **J. Choi**, J. Schilling, K. Nielsch, R. Hillebrand, M. Reiche, R. B. Wehrspohn, and U. Gösele, "Large-area Porous alumina photonic crystals via imprint method," *Materials Research Society Spring Meeting 2002, Symposium L : Photonic Crystals—From Materials to Devices*, San Francisco, USA, April 01-05, 2002, Poster.
9. **J. Choi**, J. Schilling, K. Nielsch, R. Hillebrand, M. Reiche, R. B. Wehrspohn, and U. Gösele, "Porous alumina photonic crystals obtained via nano-imprint method," *Deutsche Physikalische Gesellschaft*, Regensburg, Germany, March 11-05, 2002, Talk.
10. **J. Choi**, R. B. Wehrspohn, K. Nielsch, M. Reiche, and U. Gösele, "Mono-domain porous alumina arrays obtained via nanoimprint," *International Workshop on NanoImprint Lithography*, Lund University, Sweden, January 16-17, 2002, Poster.

# Patent

R.B. Wehrspohn, U. Gösele, K. Nielsch, **J. Choi**, R. Reiche, M. Alexe

”Nanoimprint-Stempel mit pyramidenförmigen Spitzen und dessen Anwendung zur elektrochemischen Herstellung von porösem Aluminiumoxid mit Porenabständen, die entweder größer oder kleiner sind als der Abstand des Abdruckes des Stempels im Aluminium,”

Patent Application Germany DE10207952.8 (21/Nov./2002)

Patent Application Europe PCT/EP03/01138 (17/Feb./2003).

## Acknowledgements

I was very lucky to have two good supervisors. First and foremost, I would like to thank Professor Gösele for his kind guidance and financial support and Dr. Wehrspohn (now Professor at Universität Paderborn) for his advice and constant encouragement during my Ph.D period at Max-Planck-Institute of Microstructure Physics in Halle.

I sincerely thank to my dissertation committee members for their precious time and valuable comments.

I wish to express my gratitude to Dr. Kornelius Nielsch, Dr. Guido Sauer, and Mrs. Kathrin Schwirn for introducing me to porous alumina, stimulating discussions and friendship. Special thanks is dedicated to Mrs. Cécile Jamois and Johannes Heitmann, who share not only the office, but also friendship with me for the past 3 years. I would like to express my deep appreciation to the our group members for their numerous help: Dr. Jörg Schilling (now at Caltech), Dr. Stefan Schweizer (now at Universität Paderborn), Andreas Herbst (now at Universität Paderborn), Dr. Reinald Hillebrand, Dr. Frank Müller, Torsten Geppert, Mrs. Ulrike Rehn, Sven Matthias, Silko Grimm, Johannes Hohlbein, Mrs. Kornelia Sklarek, and Steffen Richter. I sincerely thank Dr. Martin Steinhart, Dr. Petra Göring, Danilo Zschech and Mrs. Yun Luo for valuable discussions and numerous support.

I would like to thank Dr. Marin Alexe and Dr. Manfred Reiche for their contributions on development of the master stamp. Thanks also to Dr. Herbert Hofmeister for the TEM images and Dr. Wilfried Erfurth, Mrs. Ursel Doss and Mrs. Sigrid Hopfe for technical support.

I am also deeply appreciate to Cécric Maufront (now in France) and his family for their warm heart in Halle and France.

I deeply thank all Korean friends in Halle for their support and friendship. Special mention goes to Dr. Ho Nyung Lee (now at Oak Ridge National Laboratory), Sung Kyun Lee, Jongwoo Kim, Taegeun Noh (in Berlin) and their families. Without their countless support, my Ph.D would not have been successful. I am indebted to Professor Youngsuk Tak (Inha University, Korea) who taught me the electrochemistry of aluminum and Dr. Jaeyoung Lee (now at RIST, Korea) who introduced me to the MPI in Halle. During the last 3 years, I was continuously encouraged and supported by them.

I would like to thank all the individuals who helped me to be an independent researcher.

Finally, I also would like to acknowledge the Max-Planck-Gesellschaft for the opportunity to be doctoral candidate under its excellent system and support.

This thesis is dedicated to my lovely wife Sujin Noh, and my parents. Without their endless love and sacrifice, nothing would have been accomplished.

## **Eidesstattliche Erklärung**

Ich erkläre hiermit, dass ich keine anderen als die von mir angegebenen Quellen und Hilfsmittel zur Erstellung meiner Dissertation verwendet habe. Den benutzten Werken wörtlich oder inhaltlich entnommene Stellen sind als solche gekennzeichnet.

Jinsub Choi

Halle (Saale), im October 2003